Probing Charge Transport and Thermoelectricity in Molecular Junctions

by

Ruijiao Miao

A dissertation submitted in partial fulfillment
of the requirements for the degree of
Doctor of Philosophy
(Mechanical Engineering)
in The University of Michigan
2019

Doctoral Committee:

Professor Edgar Meyhofer, Co-Chair
Professor Pramod Reddy, Co-Chair
Associate Professor Vikram Gavini
Associate Professor Anish Tuteja

Ruijiao Miao

mruijiao@umich.edu

ORCID iD: 0000-0002-4680-1343

To my parents

Acknowledgements

Twenty years ago, I told my parents my dream was to build a farm on my own grassland, where I could live freely. When my teacher asked us to write about our dreams, however, I wrote down the word “scientist” just to get a high homework grade, with no idea what scientists do.

Later in my life, I’ve learned that freedom is not presented by how much land one owns, but how far one’s thoughts and scope can reach. I began to admire those who are trying to discover the mechanism of how everything works, and my interest in physics and engineering developed since then, which finally led me to the road of pursuing a PhD degree. It might or might not be a coincidence, that after twenty years I am now exploring science.

The procedure of getting a PhD degree is challenging while exciting. I would like to say thank you to many people without whom this achievement would not be possible.

I wish to thank my co-advisors at University of Michigan, Professors Pramod Reddy and Edgar Meyhofer, for supporting me with scientific training and for suggesting interesting and challenging research topics. During the past a few years they showed rigorous and diligent attitude to science, which would benefit my entire career life. I am also thankful to my committee members, Professors Vikram Gavini and Anish Tuteja, for their advice and encouragement.

Further, I am grateful to my colleagues at University of Michigan for their contributions to my work. I wish to thank Dr. Youngsang Kim for his tutorial which led me into the field of molecular

electronics, and Professor Andrej Lenert for his help in rebuilding my experiment platform. Meanwhile, my research would not have been possible without the help of Dr. Longji Cui, Dr. Bai Song, Dr. Dakotah Thompson, Dr. Charles Chang Jiang, and Dr. Kun Wang.

Moreover, I wish to acknowledge my collaborators all over the world. Maxim Skripnik, Dr. Kim G. L. Pedersen, Dr. Linda Angela Zotti, did the computational work. Hailiang Xu, and Zico Alaia Akbar synthesized molecules used in my work. I also thank Professors Fabian Pauly, Sung-Yeon Jang, Martin Leijnse, Juan Carlos Cuevas, Kenneth Wärnmark, and Heiner Linke for their discussion.

I am in debt to all my friends in and outside Ann Arbor, who shared insightful thoughts with me; who provided generous help and blessing when I was in depression and frustration; and who made lots of laughter on the badminton court.

My special appreciation goes to Dr. Longji Cui, for all his wise or stupid suggestions on my research and personal life. For his applause, criticism, trust, patience, and encouragement to me. For his serious thinking about work and life, success and failure, happiness and sorrow. For his unyielding will towards his goals.

My deepest gratitude goes to my parents, for their endless love and unlimited support.

"Two roads diverged in a yellow wood, and sorry I could not travel both." There are always multiple branches along the way, yet I never have any regret for my decisions. Over the years I have learned how to make my choice the best choice, and I'm ready for the next one.

The most important thing is, now I hold a tiny piece of grassland in my heart.

Table of Contents

List of Figures

List of Tables

Abstract

The study of charge transport and thermoelectricity in molecular junctions is of fundamental interest for understanding charge transport mechanisms and provides knowledge critical for the development of nanotechnologies including electronics, energy conversion and thermal management. In spite of a large amount of theoretical and experimental work into charge transport and thermoelectric properties of various molecular junctions, several important questions remain unsolved.

Quantum phenomena dominate transport in molecular junctions, therefore, a natural question to ask is whether it is possible to tune the thermoelectric properties of molecular junctions via quantum interferences. To answer this question, I present work where we investigated charge and thermoelectric properties in molecular junctions based on two oligo (phenylene ethynylene) (OPE) derivatives where quantum interference effects are expected to arise. Our experiments reveal that *meta*-OPE3 junctions, which are expected to exhibit destructive interference effects, yield a higher thermopower (with ~20 μV/K) compared with *para*-OPE3 (with ~10 μV/K). Results from both single-molecule junction and monolayer experiments correspond well with each other and agree well with computational predictions made by our collaborators. Our results show that quantum interference effects can indeed be employed to enhance the thermoelectric properties of molecular junctions.

Along with enhancing thermoelectric properties of molecular junctions via quantum interference, past theoretical work has proposed another strategy to tune the thermoelectric properties in molecular junctions by varying the metal centres incorporated in porphyrins. The tunability of thermoelectric properties in these junctions, however, have not been experimentally explored. To explore the feasibility of tuning the thermoelectric properties in these junctions, we conducted measurements in Au-porphyrin-Au, Au-(Cu-porphyrin)-Au and Au-(Zn-porphyrin)-Au junctions. To achieve better thermoelectric performance, we replaced the thiol end groups that are typically employed in a series of metallo-porphyrins with triisopropylsilyl end groups, which enable a direct C-Au bond resulting in an increase of the electrical conductance. In fact, our single molecule experiments show nearly two orders of magnitude increase in the electrical conductance of junctions compared to previous work that employed thiol end groups. The thermoelectric experiments reveal tunable thermopower through molecules with different metal centres. Overall, among the molecules studied in our work, we find that Au-(Zn-porphyrin)-Au junctions exhibit the best thermoelectric performance.

In addition to the energy conversion of heat-to-electricity as discussed above, thermoelectric effects are also expected to enable cooling in molecular junctions through Peltier effects and in principle such Peltier cooling in molecular junctions may be applied to fabricate refrigerators at molecular scale. However, experimental observation of Peltier cooling in molecular junctions has not been possible. Here, I discuss the experimental observation of Peltier cooling in molecular junctions. The molecular junctions studied here are Au-(biphenyl-4,4'-dithiol)-Au, Au-(terphenyl-4,4"-dithiol)-Au and Au-(4,4'-bipyridine)-Au, of which the charge transport and thermoelectric properties are widely studied in the field. Our results unambiguously show cooling in molecular junctions under small bias voltage and reveal the relationship between heating or cooling and

charge transport mechanisms in studied molecular junctions. Our experimental results are supported by computational results from our collaborators.

Chapter 1 Introduction

1.1 Molecular Electronics

The miniaturization of electronic circuit elements is always a requirement in semiconductor industry.[1] Using single organic molecules or molecule assembles as building blocks for electrical devices has become a promising solution due to their intrinsic nanometer size. Molecular junctions, created by bridging single molecular or molecule assembly between metal electrodes, have been widely explored in the past several decades. The achievements have led to the field of molecular electronics, which aims to investigate the charge and thermal transport properties in molecular junctions including both single-molecular junctions and molecule assembly.

Molecular electronics has become one of the most important field in nanotechnology since it not only provides fundamental knowledge on how charge and phonon transport across the junctions but also facilitates application in nanotechnology.[2-7] From the point of view of basic science, molecular electronics focuses on charge and thermal transport phenomena at nanometer and sub-nanometer scale, which differs that in bulk materials. At this regime, the charge and thermal transport are dominated by quantum mechanics, and the effect of mechanical, electrical, optical and magnetic properties of molecules can act together and lead to varieties of physical phenomena. These phenomena can be employed to develop devices for electronics, signal detection, energy conversion and energy storage. However, the charge

and thermal transport mechanism in molecular junctions have not be fully understood yet and there are many questions to be answered in this field.[8, 9] In this sense, molecular electronics is gaining more and more attention with molecular junctions as a good platform to investigate and control charge and thermal transport at the atomic and molecular scale.

From the point of view of nanotechnology, molecules are good electronic elements as they have several advantages.[1, 10] First of all, molecules used in molecular electronics have small size off 1 – 10 nm, which represents the limit in current semiconductor industry. This could allow packing of electronic devices in an extremely high density. Towards this goal, people are attempting novel technologies in order to create molecular devices with high density, low cost and high efficiency. Second, self-assembled nanoscale structures can be utilized to investigate intermolecular interactions. This method can be used to modify the conformation of molecules and led to switching behavior of molecular junctions. The result can be employed to develop nanoscale sensors and signal detecting devices. Also, molecular electronics bring novel functionalities to current electronic devices. With carefully chosen existing molecules, the specific properties could lead to new electronic functions in the circuit which are not present in silicon-based circuits. Moreover, synthetic technology has enabled the design and tailor of molecules. The charge and thermal transport properties in molecular junctions can be varied by choosing the chemical composition and geometry of molecules. The tailored molecules could also exhibit mechanical, optical and magnetic properties, which further expand the application of molecular electric devices. Altogether, although molecular junctions have not been applied in practical device manufactory in industry, researchers are pushing the field towards better understand of charge and thermal transport properties and possible electronic devices with high efficiency and outstanding performance.

The history of molecular electronics can be traced back to 1970s.[4] Kuhn and Mann conducted conductivity measurements of cadmium salts of fatty acids in 1971 and the results showed exponentially decayed conductivity with layer thickness, which implies tunneling transport mechanism through the molecule monolayer. Later in 1974, Aviram and Ratner first discussed the charge transport through a single molecule theoretically. In this work a single molecule was creatively proposed to act as an electronic device, a molecular rectifier, for the first time.

The theoretical work following Aviram and Ratner[11] in 1970s urged for experimental tools to verify the results. The invention of scanning tunneling microscope (STM) by Gerd Binning and Heinrich Rohrer in 1981 and atomic force microscope (AFM) in 1982 made experiments on single molecule level possible. Despite the ability to obtain topology information at atom scale as imaging tools, STM and AFM enable trapping of single and multiple molecules between metal materials to create molecular junctions with high yield thus facilitates abundant experimental studies. As pioneer experimentalist, Mark Reed's group carried out significant work[12-15] to understand the charge transport at single-molecule levels in the 1990s and 2000s. In 2003, Xu and Tao[16] employed STM to repeatedly form single molecular junctions and measured their resistance. This technique is referred as scanning tunneling microscope break junction (STM-BJ) and is widely used in the field molecular electronics. Similarly, conductive probe AFM (CP-AFM) are used to conduct experiment on molecular monolayers[17-19]. Furthermore, other techniques including mechanically controlled break junction (MCBJ)[20, 21], electromigrated break junction (EBJ)[22] and nanocrystal arrays[23] also provide experiment platform for the investigation of charge and thermal transport properties in molecular junctions.

The developments in both theoretical and experimental tools have led to tremendous interesting studies in the field of molecular electronics and greatly broadened the topics. Besides the conductance in molecular junctions, researchers explored several topics in the past a few decades. One is the correlation between mechanical force and charge transport properties in molecular junctions, where AFM-based force spectroscopy acts as powerful tool since it provides force and distance information at the same time[24]. Another branch in molecular electronics is to discover the optical properties and their influence on charge transport in molecular devices. Optical spectroscopies, for example Raman spectroscopy[25], could provide characterization of the local junction structure and thus enable the study of interaction of plasmons with molecules at nanoscale. Meanwhile, people also investigate the possibility to control the spin states in the molecule or electrodes therefore to create potential spintronics devices[26] for data storage and quantum computation. In the aspect of energy conversion, Reddy *et al.*[27] adapted the STM-BJ technique and conducted the first thermoelectricity measurement in single-molecular junctions. After that researchers have been developing approaches to increase the thermopower and energy conversion efficiency in molecular junctions (See Chapter 2).

1.2 Overview of this dissertation

Within the field of molecular electronics, the study of charge transport and thermoelectricity in molecular junctions has drawn increasing attention, since it not only provides understanding of fundamental charge transport mechanism across molecular junctions but also provides promising approaches for energy conversion and waste heat recycle at nanometer scale. The aim of the research is to realize thermoelectric devices with high thermopower, high energy conversion efficiency and high output power at optimized

efficiency. The realization of these goals requires molecular junctions with (1) high electrical conductance, (2) high thermopower (also called Seebeck coefficient) and (3) low thermal conductance. I will discuss the details of improving thermoelectric performance of molecular junctions in Chapter 2. The electrical conductance and Seebeck coefficient are directly related to charge transport across the molecular junctions, while the thermal conductance relates to both charge and phonon transport in the molecular junction. In this dissertation, I will focus on the work of improving thermoelectric performance via increased electrical conductance and Seebeck coefficient. Past experiment work has measured the electrical conductance and thermoelectricity in a bunch of single-molecular and molecule monolayer junctions, however the approaches to increase the power factor in molecular junctions have not been fully explored. The main questions that are to be addressed in this dissertation are: (1) is it possible to increase the electrical conductance in molecular junctions? (2) Is it possible to increase the thermoelectricity in molecular junctions via quantum interference?

To answer these questions, it requires both an understanding of the charge transport across molecular junctions and experiment platforms for steadily trapping of molecules and repeatedly forming molecular junctions. In Chapter 2, I will first discuss the theoretical frame work of charge transport and thermoelectricity in molecular junctions. Then I will briefly introduce current available experiment tools and techniques to study charge transport and thermoelectricity in molecular junctions. Following this introduction, I will review the computational and experimental work in this field so as to give a better understanding of the charge transport and thermoelectricity in molecular junctions.

In Chapter 3, I will discuss the work of tuning electrical conductance and thermoelectricity and in molecular via quantum interference. The molecules studied in this work are two OPE

derivatives with same chemical composition but different geometry on the center benzene ring. Destructive interference arises in the meta-connected molecule and lead to increased thermopower in the molecular junctions. However, the electrical conductance is suppressed due to the same effect. Both single-molecular junction and monolayer experiments were conducted, and the results agree well with each other.

In Chapter 4, I will describe the work of investigation charge transport and thermoelectricity in metallo-porphyrin molecular junctions with varied metal centres. Porphyrins are widely studied due to their varied functional properties. As a highly conjugated molecule, it provides impressive charge transfer properties. Different metal centres incorporated within the porphyrins are proven to be able to tune the charge transfer properties in molecular junction, yet the ability to tune thermoelectric properties remains unexplored. In this work a series of Au-metallo-porphyrin-Au junctions were investigated to reveal the effect of different metal centres on charge transport and thermoelectric properties. One the other hand, direct Si-Au bond were employed to bridge the molecules with Au electrodes, which leads to nearly two orders of magnitude increase in electrical conductance.

In Chapter 5, I will discuss the observation of Peltier cooling in molecular junctions, which is a critical step for establishing molecular-base refrigeration. An experimental platform was created to allow unified characterization of electrical, thermoelectric and energy dissipation characteristics of molecular junctions by integrating conducting-probe atomic force microscopy with custom-fabricated picowatt-resolution calorimetric microdevices, we created a platform. Au-(biphenyl-4,4′-dithiol)-Au, Au-(terphenyl-4,4″-dithiol)-Au and Au-(4,4′-bipyridine)-Au junctions were studies and revealed the relationship between heating/cooling and charge transportation characteristics.

Chapter 2 Charge Transport and Thermoelectricity in Molecular Junctions

Reproduced with permission from *The Journal of Chemical Physics.*

Longji Cui*, Ruijiao Miao*, Chang Jiang, Edgar Meyhofer and Pramod Reddy, *the Journal of Chemical Physics*, **146**, 092201, (2017).

2.1 Abstract

With the advent of molecular electronics, tremendous attention has been paid towards understanding the structure-function relationship of single molecular junctions. Understanding how charge is transported and how heat is converted into electricity in molecular junctions is of great importance to design thermally robust molecular circuits and high-performance energy conversion devices. Additionally, the study of thermal and thermoelectric phenomena in molecular junctions provides novel insights into the limits of applicability of classical laws. Here, we present a review of the computational and experimental progress made in probing thermoelectric effects in self-assembled monolayer and single molecular junctions. We also discuss the outstanding challenges and interesting future directions in this field.

2.2 Introduction

The intriguing idea[11] of building electrical components and interconnects using single molecules has greatly inspired researchers over the past 40 years and led to the emergence of the field of "molecular electronics". Transport characteristics of junctions of single molecules between electrodes (Fig. 2-1 a), called molecular junctions, have been extensively explored to investigate the feasibility of creating molecular devices with desirable transport characteristics. Both experimental and theoretical work has shown that molecular junctions can indeed be employed to achieve unique and interesting charge transport characteristics.[2, 3, 10, 28-32] Owing to the technical and computational advancements over the last decade, energy (thermal) transport and conversion properties of molecular junctions have attracted considerable attention[6, 8, 9, 33-36]. Fundamentally, probing thermal transport in molecular junctions is useful to understand the limits to the applicability of classical theories at the nanoscale. Moreover, such studies are also essential for future practical applications of molecular junctions in electronic devices and in developing high-efficiency energy conversion devices. For example, it has been computationally proposed that by carefully designing molecular junctions, it is possible to achieve very efficient thermoelectric energy conversion.[37-40] Furthermore, single molecular chains are also expected to feature ultrahigh thermal conductivities, in strong contrast to the relatively poor thermal conductivity of polymer materials,[41, 42] indicating that a more detailed understanding of thermal transport in such molecules may enable the creation of polymer based materials with high thermal conductivity.

In this chapter, we review current understanding of thermal and thermoelectric properties of molecular junctions. Insights obtained from both theoretical and experimental

investigations of both self-assembled monolayer (SAM) and single molecular junctions will be described. Our paper is organized as follows: in Chapter 2.3, we briefly introduce the Landauer formalism that is used to describe transport in molecular junctions; subsequently in Section 2.4, we review the theoretical and experimental advancements in studying thermoelectric effects in molecular junctions. Finally, we conclude by highlighting some open questions in the field.

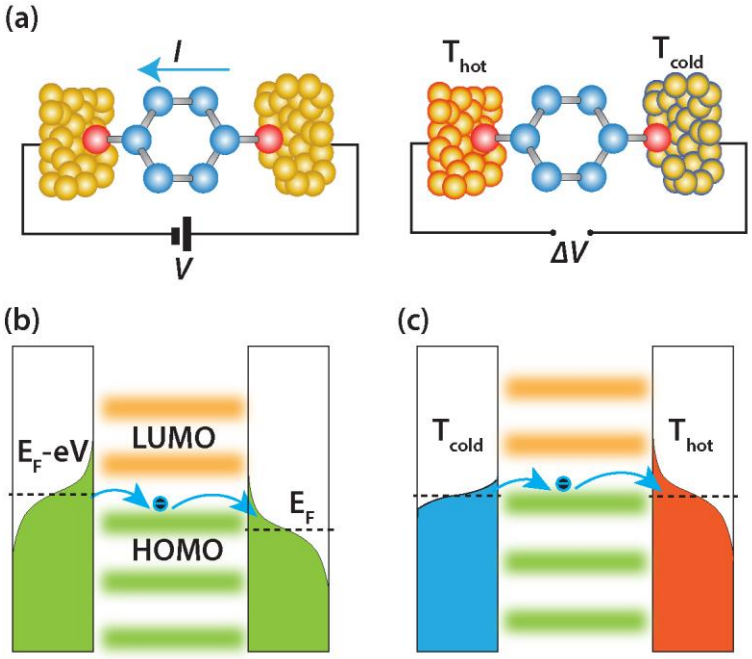

Figure 2-1 Schematics describing charge, thermoelectric and thermal transport in molecular junctions. (a) An organic molecule bridged between two electrodes to form a single molecular junction. Left: electrical conductance measurement scheme. Middle: thermoelectric (Seebeck coefficient) measurement scheme. Right: thermal conductance measurement scheme. (b) Electric currents in a molecular junction are driven by a difference in the Fermi-Dirac distributions in the electrodes arising from an applied bias (V). (c) Thermoelectric transport under a temperature difference (T_{hot} - T_{cold}). The sign of the Seebeck coefficient (S) is detemined by the alignement of the HOMO and LUMO levels of the molecular junction with respect to the Fermi level of the electrodes.

2.3 Theoretical Framework Describing Charge Transport and Thermoelectricity in Molecular Junctions

2.3.1 Electrical Conductance of Molecular Junctions

Landauer's seminal work[43] which relates electrical conductance to electron transmission is widely used for describing transport in molecular junctions.[44-46] Within the Landauer formalism (Fig. 2-1 b), the electrical current (*I*) at finite bias (*V*), is given by[46]

$$I = \frac{2e}{h} \int_{-\infty}^{+\infty} (f_L - f_R)\tau(E)dE \tag{2.3.1}$$

where $f_{L/R}$ is the Fermi-Dirac distribution of the left/right electrodes and $\tau(E)$ is the transmission function, which describes the probability of electrons transmitting through the molecular junction. The Fermi-Dirac distribution is given by

$$f_{L/R} = \left[1 + \exp\left(\frac{E - \mu_{L/R}}{k_B T_{L/R}}\right)\right]^{-1} \tag{2.3.2}$$

where *E* is any given energy, k_B is the Boltzmann constant and $T_{L/R}$ are the temperatures of the left and right electrodes.

By applying the small-bias and low-temperature approximations, Eq. (2.3.1) can be simplified to yield

$$\frac{I}{V} = G_e = \left(\frac{2e^2}{h}\right)\tau_{E=E_F} \tag{2.3.3}$$

Interestingly, for one fully open channel ($\tau_{E=E_F} = 1$), we find a limit value

$$G_e = G_0 = \frac{2e^2}{h} = \frac{1}{12.9\ \mathrm{k\Omega}} \tag{2.3.4}$$

which is called the electrical conductance quantum.

2.3.2. Seebeck Coefficient in Molecular Junctions

The thermoelectric properties of molecular junctions can also be described within the Landauer formalism (Fig. 2-1 c). Specifically, when a temperature difference (ΔT) is applied across a molecular junction, an open-circuit voltage (ΔV) develops across the junction (Fig. 2-1 c). The Seebeck coefficient (S) is given by $S = -\Delta V/\Delta T$ and can be related to the transmission function by[47, 48]

$$S = -\frac{\pi^2 k_B^2 T}{3|e|} \frac{\partial \ln\big(\tau(E)\big)}{\partial E}\bigg|_{E=E_F} \tag{2.3.5}$$

It is clear from the above expression (valid if the transmission function changes approximately linearly with E on the scale of k_BT) that the slope of the transmission functions at the chemical potential (Fermi energy) determines the sign and magnitude of the Seebeck coefficient.

2.3.3 Thermoelectric Transport in Molecular Junctions

Thermoelectric materials have long been employed for solid-state heat engines that convert heat into electricity. The energy conversion efficiency is represented by a dimensionless quantity called the figure of merit (ZT) which is defined as

$$ZT = \frac{S^2 \sigma T}{\kappa} \tag{2.3.6}$$

where S is the Seebeck coefficient (also called thermopower), σ is the electrical conductivity, κ is the thermal conductivity and T is the absolute temperature. Analogous to bulk materials, the efficiency of a molecular junction in converting heat into electricity is quantified by

$$ZT = \frac{S^2 G_e T}{G_{th}} \tag{2.3.7}$$

where G_e and G_{th} represent the electrical and thermal conductance respectively. The energy conversion efficiency (η) of a molecular junction monotonically increases with ZT and is given by

$$\eta = \eta_C \frac{\sqrt{1+ZT}-1}{\sqrt{1+ZT}+{T_C}/{T_H}} \tag{2.3.8}$$

where T_H and T_C are the temperature of the hot side and the cold side, respectively, and

$$\eta_C = 1 - {T_C}/{T_H} \tag{2.3.9}$$

is the Carnot efficiency which is the upper limit of heat-to-work conversion efficiency any heat engine can reach. It can be seen from Eq. (2.3.8) that achieving high energy conversion efficiency requires a large ZT which in turn can be obtained if the molecular junctions feature a large thermopower and electric conductance, and a small thermal conductance. Given the results in Eq. (2.3.1), Eq. (2.3.5) and Eq. (2.3.7) it is clear that large values of ZT can be achieved if molecular junctions simultaneously feature a large value of $\tau(E)$ and a large gradient of the transmission $\partial\tau / \partial E$ at the chemical potential.

2.4 Computational Studies of Charge Transport and Thermoelectricity in Molecular Junctions

One of the first studies to explore thermoelectric properties in molecular junctions was by Paulsson and Datta[48] where they analyzed the thermoelectric current and voltage of benzenedithiol (BDT) based molecular junctions. Their findings suggested that the thermoelectric current and voltage output of BDT molecular junctions were large enough to be measured and insensitive to the molecule-electrode coupling details. Further, this work highlighted that the relative position of the HOMO (highest occupied molecular orbital) and LOMO (lowest unoccupied molecular orbital) with respect to the Fermi energy plays an important role in determining the sign of the Seebeck coefficient, suggesting that thermoelectric measurements of molecular junctions can reveal important information about the electronic structures of molecular junctions.

Subsequently, several groups theoretically studied the thermoelectric properties of molecular junctions to explore the feasibility of achieving high *ZT*.[37, 38, 49-62] For example, Finch *et al.*[37] presented a computational study for CSW-479-bipyridine molecular junctions with gold electrodes (Fig. 2-2 a). They showed that by tuning the orientation of side group with respect to the molecular backbone, the thermopower could be dramatically enhanced, resulting in a large *ZT* value. They attributed this enhancement to Fano resonance[63], which arises from the presence of degenerate energy levels in the molecular backbone and the side groups. Specifically, they found that the transmission function showed a peak, which was shifted towards the Fermi energy by controlling the angular orientation of the side group.

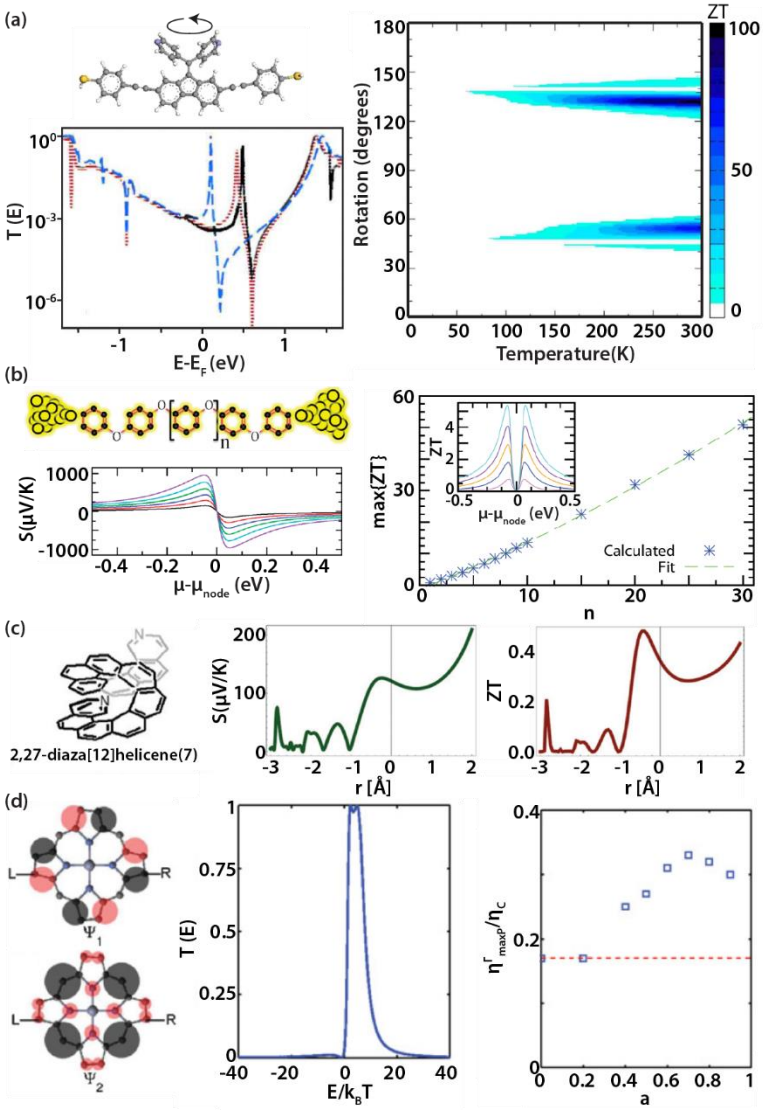

Figure 2-2 Theoretical proposals for enhancing thermoelectricity in molecular junctions. (a) Results for CSW-479-bipyridine molecule.[37] Left top: schematic of the molecule with a side group which can rotate around the C-C bond connecting it to the molecule. Left bottom: transmission function when the side group is rotated. Right: calculated ZT with respect to rotation angle and temperature. Darker color indicates higher ZT. (b) Results of thermeoelctric properties of polyphenyl ether (PPE) molecules.[38] Schematic of the molecule is shown on top left with length denoted as n. Left bottom: Seebeck coefficient vs chemical potential from n = 1 (black line) to n = 7 (purple line). Right: Maximum ZT plotted as a function of n. Insert: ZT vs. chemical potential, where the maximum ZT value increases with n. (c) Helicene molecular junctions.[40] Left: Schematic of helicene molecule subject to mechanical stretching/compression. Middle: Seebeck coefficient with respect to stretching/compressing distance. r < 0 indicates compression and r > 0 stretching. Right: Plot of calculated ZT. (d) Analysis of high power output energy conversion.[60] Left: schematic of zinc porphine molecule with sketching of wave function of the two degenerate levels. Light/dark shade indicates

positive/negative magnitude of wave function. Middle, plot of the transmission function. The low-energy tail is eliminated. Right: plot of efficiency at maximum output power (η^{Γ}_{maxP}) in unit of Carnot efficiency (η_C) as a function of the difference between the coupling strength of two levels (a, defined in Eq. (2.4.3)).

Bergfield *et al.*[38] investigated polyphenyl ether (PPE) molecules bridged between gold electrodes (Fig. 2-2 b). Their work suggested that a sharp peak in the transmission function near the Fermi energy could arise from quantum interference effects[58, 64, 65], and thus led to a large Seebeck coefficient. Further, they showed that by increasing the number of phenyl rings in the molecule, very high *ZT* (> 4) was reachable.

Besides modifying the shape of transmission function by means of quantum interference, recent work has also found that spin-crossover could be used to tune the charge transport[66-68] and thermoelectric properties[69] of molecule-ferromagnetic metal junctions. Ghosh *et al.*[69] studied a spin-crossover molecule Fe(2-(1H-pyrazol-1-yl)-6-(1H-tetrazole-5-yl)pyridine)$_2$ ([Fe(L)$_2$]) which has a sharp transition from a low-spin (LS) state to a high-spin (HS) state upon elevating the temperature of the junction, and both spin and electron contributed to the thermoelectric current. *ZT* at HS (350 K) was found to be 4 times higher than that that at LS (250 K).

Vacek *et al.*[40] studied thermoelectric properties in helicene molecular junctions when the helical shaped junctions are mechanically stretched or compressed (Fig. 2-2 c). They showed that when the molecular junction is compressed, a significant enhancement of electrical conductance and a sign-change of thermopower, originated from the change in the overlapping of the wave functions of nearest atoms, are expected, resulting in an increase in *ZT*. Upon stretching, the *ZT* value was found to first decrease and subsequently increase. They suggested that the idea of mechanically controlling electric conductance and thermopower

could also be applied to other non-planar shaped molecules including cycloparaphenylenes, cyclacenes, ball-like molecules, carbon cages, tailored fullerenes, fullerene cages and short DNA molecules.

Despite the studies indicating the possibility to perform thermoelectric energy conversion at efficiencies close to the Carnot limit, operation close to the Carnot limit implies almost reversible thermodynamic processes and therefore, the power output is negligible. In practice, as have been highlighted in recent works[60, 70, 71], it is essential to understand the relationship between efficiency and power out under irreversible conditions. The Curzon-Ahlborn (CA) limit, which describes the thermodynamically maximum efficiency of a heat engine operating under conditions where the power output is maximized, is therefore of great interest. The maximum efficiency of a heat engine operating at maximum output power is given by

$$\eta_{CA} = \frac{\eta_C}{2} + \frac{\eta_C^2}{8} + O(\eta_C^3) + \cdots \tag{2.4.1}$$

Where $\eta_{CA}(\eta_C)$ is the Curzon-Ahlborn (Carnot) efficiency. To achieve this maximum output power, the transmission function of molecular junctions has to be rationally designed.

In this regard, Nakpathomkun *et al.*[39] studied a low-dimensional system with an approximately Lorentzian shape transmission function, which is given by

$$\tau(E) = \frac{\left(\frac{\Gamma}{2}\right)^2}{(E - E_0)^2 + \left(\frac{\Gamma}{2}\right)^2} \tag{2.4.2}$$

where E_0 is the center position of the Lorentzian and Γ is the full width at half of maximum of $\tau(E)$. When the Lorentzian is very sharp with Γ close to zero, the power output becomes

zero. By carefully choosing Γ and the relative position between E_0 and E_F, the output power can be optimized. Although optimized output power is achieved, the Curzon-Ahlborn limit can't be reached with a Lorentzian shaped $\tau(E)$, since its low-energy tail indicates that the electric current in the direction opposite to the thermoelectric current is not filtered.

To overcome this challenge, Karlstrom *et al.*[60] took advantage of the quantum interference in a two-level system (Fig. 2-2 d) where the transmission function is expressed as

$$\tau(E) = \Gamma^2 \left| \frac{1}{(E-E_F)+E_1+i\Gamma} - \frac{a^2}{(E-E_F)+E_2+ia^2\Gamma} \right| \quad (2.4.3)$$

where the energy levels E_1 and E_2 are located on the same side of E_F, and the coupling strengths of the two energy levels to the electrodes are differed by a factor of a^2. When $E_2 = a^2E_1$, $\tau(E)$ is zero at E_F and is large for a finite range of energies above E_F. This implies that $\tau(E)$ has a large gradient at E_F and a finite width so that the system can operate with large power output. They further showed that the efficiency of such a system can be very close to the CA-limit and can be realized in Au-zinc porphyrin-Au molecular junctions.

Taken together, computational work on the thermoelectric efficiencies of molecular junctions suggests that there are various strategies to achieve energy conversion at very high efficiencies (close to the Carnot limit) and large power outputs (close to the CA-limit). By taking advantage of strategies like having a delta-function (or step function) shape transmission function with steep slope in the optimum position from the Fermi energy, and creating an asymmetric Lorentzian-like transmission function with limited width, thermopower can be significantly enhanced in molecular junctions.[72] Furthermore, approaches to tune the transmission function are not limited to what introduced above. Other methods, such as, redox control of the quantum interference within phase coherent molecular

wires,[73] varying the transition metal-centre in porphyrin-based conjugated molecules,[74] and creating π-π overlap between planar aromatic anchor groups and electro-burnt graphene electrodes,[75] can also be employed to increase the thermopower and *ZT* in molecular junctions. In the following, we will discuss about the experimental studies of the thermoelectric properties of molecular junctions.

2.5 Experimental Techniques and Experimental Studies in Investigating Charge Transport and Thermoelectricity Properties in Molecular Junctions

Several groups have experimentally quantified the thermoelectric properties of molecular junctions. Below, we first provide a brief discussion of experimental techniques that were developed to measure the thermoelectric properties of molecular junctions in two-terminal configurations, i.e., techniques that enable the measurement of a voltage output from junctions created by trapping molecules between a hot and a cold electrode. Subsequently we review the studies on the dependence of thermopower in molecular junctions on various factors such as molecular length, end groups, molecular structures and conformation, electrode materials, and temperature. Finally, we discuss about the three-terminal techniques that enable tuning the thermoelectric properties of molecular junctions.

2.5.1 Two-terminal Thermoelectric Measurements

The thermoelectric properties of molecular junctions were first experimentally probed by Reddy *et al.*[27]. In performing these studies the authors adapted a STM based technique called the STM break-junction (STMBJ) technique that was originally developed by Xu and Tao[16] for probing electrical transport in molecular junctions (Fig. 2-3 a). Since the electrical and thermoelectric properties of molecular junctions are pivotal to thermoelectric energy

conversion, we first introduce the STMBJ technique and then describe how Reddy *et al.*[27] modified it for single-molecule thermoelectric measurement.

In the STMBJ technique a voltage bias is applied between the sharp tip of an STM (typically made of Au) and an Au substrate covalently bonded with a monolayer of molecules. The tip is displaced towards the substrate while the electrical conductance between the tip and the sample is being monitored. This process continues until an electrical contact is established and an electrical conductance of ~5 G_0 or greater is observed (signifying the formation of Au-Au atomic contacts). During this process, in addition to the formation of Au-Au contacts, some molecules stochastically bridge the electrodes (see Fig. 2-3 b). Subsequently, the tip is withdrawn from the substrate, while the electrical conductance is being recorded. This process results in a scenario where a few molecules bridge the tip and substrate. By further withdrawing the tip, the molecular bridges break successively until there is only one molecule existing between the tip and the substrate. During this withdrawal process the electrical conductance of the tip-molecule-substrate junctions is measured. Typical conductance traces obtained in such an experiment[76] are shown in Fig. 2-3 c. A substantial number of conductance traces can then be used to analyze and obtain statistically significant information about the electrical properties of molecular junctions.

In order to modify this STMBJ technique to study thermoelectric effects of molecular junctions, the key is to set up a temperature difference across the molecular junction. In Fig. 2-4 a, a single molecular junction formed by using the STMBJ technique is depicted. The Au substrate is heated while the STM tip is kept at room temperature by putting it in contact with a large thermal reservoir. Because the molecular junction thermal conductance is sufficiently smaller than the thermal conductance between the gold STM tip and the thermal reservoir

with which it is in contact, a tip-substrate temperature difference, ΔT, is therefore stably established.[55, 57]

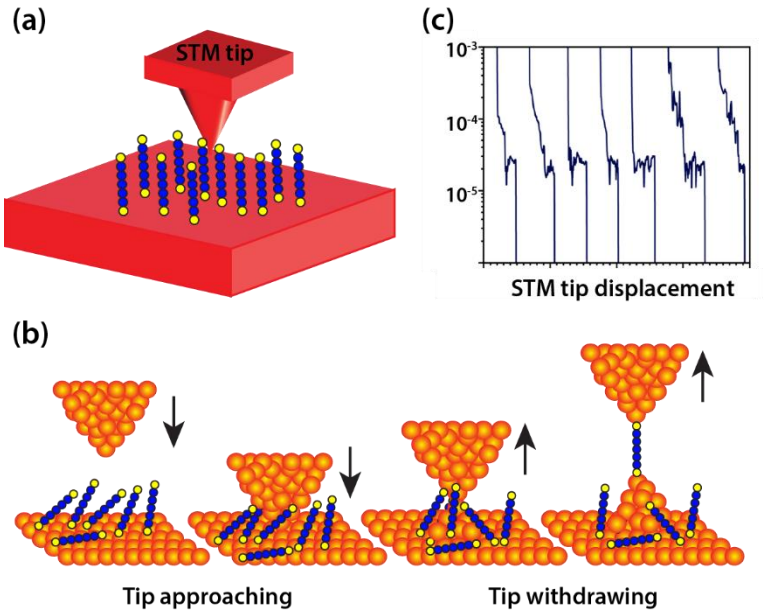

Figure 2-3 Schematics of STM break junction (STMBJ) technique. (a) STM tip is in proximity to a substrate bonded with SAM molecular junctions. (b) The process of trapping a single molecular junction. STM tip is brought in contact with the substrate. Molecular junctions are formed when the STM tip retracts from the substrate until only one molecule bridges the tip and substrate. (c) Representative traces of electrical conductance of the junction during the withdrawal process.[76]

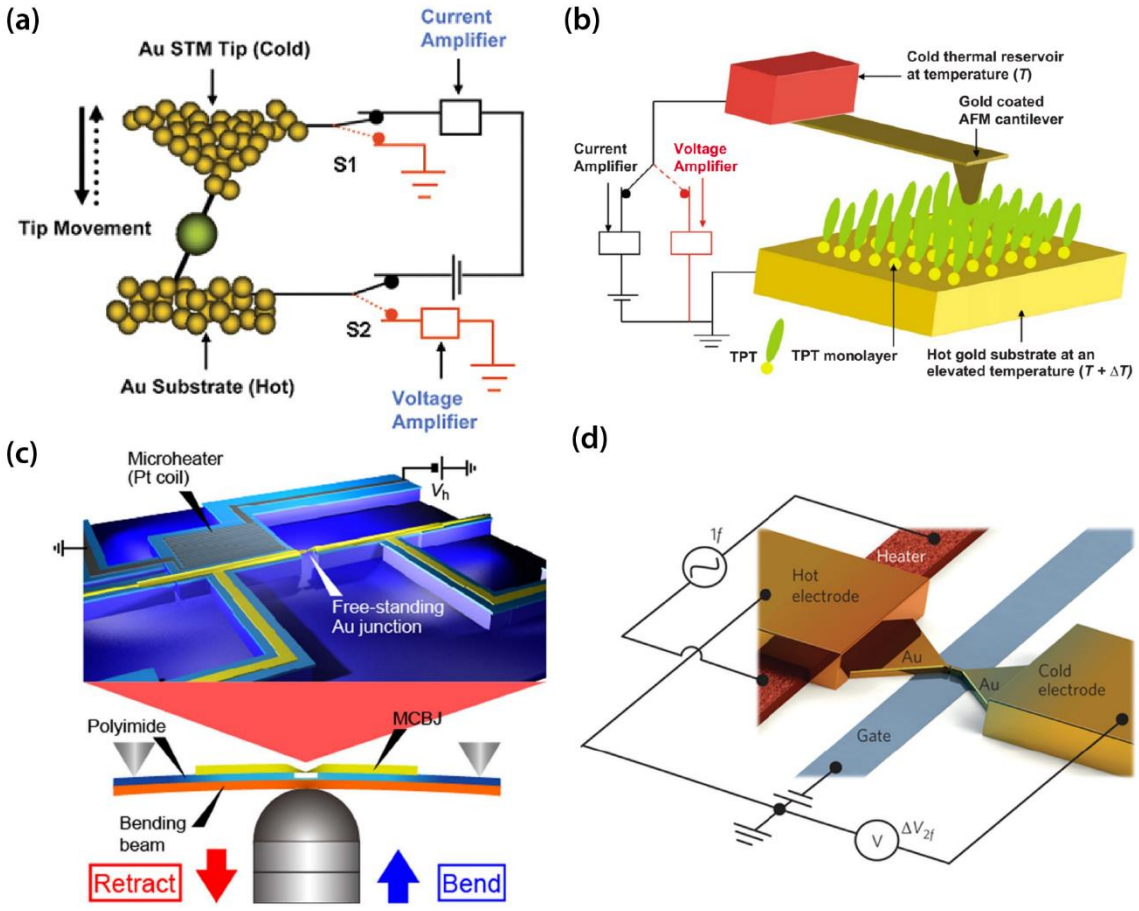

Figure 2-4 Schematics of experimental setups for thermoelectric measurements of molecular junctions. (a) STMBJ based setup.[27] The STM tip is kept at ambient temperature while the substrate is heated up. The current and voltage amplifier are switched on alternatively to measure the thermoelectric voltage across the junctions. (b) CP-AFM based setup.[17] The AFM cantilever is in contact with a reservoir at temperature T while the Au substrate is heated to an elevated temperature $T + \Delta T$. (c) MCBJ setup.[77] A free-standing Au junction is created by bending the substrate. Temperature differentials between the electrodes are achieved via an integrated Pt coil micro-heater. A polyimide layer insulates the Au electrodes from the bending substrate. (d) EBJ setup.[22] A gate electrode is used to tune the electronic structure of the junction. One of the electrodes is heated by applying a sinusoidal electric current at frequency f through an integrated heater, resulting in a temperature difference and a thermoelectric voltage output at frequency $2f$.

The procedure to measure the Seebeck coefficient involves the trapping of multiple molecules between the electrodes by following the procedure described above. Afterwards, the voltage bias and the current amplifier that are used to monitor the current are disconnected

and a voltage amplifier is connected to measure the thermoelectric voltage induced by ΔT (see Fig. 2-4 a). Subsequently, the tip is slowly withdrawn until all the molecules trapped break off. During this process, the output voltage, ΔV, is continuously monitored. When the last molecule breaks off, the thermoelectric voltage vanishes. This output voltage ΔV, due to ΔT, is a measure of the Seebeck coefficient and is obtained by $S = -\Delta V / \Delta T$.

Reddy *et al.*[27] employed the above-described STMBJ technique to probe the thermoelectric properties of molecular junctions created from benzenedithiol, dibenzenedithiol and tribenzenedithiol molecules and Au electrodes (Fig. 2-5 a). These experiments revealed that the Seebeck coefficient of these aromatic molecular junctions is positive and increased monotonically (and approximately linearly) with molecular length.

The STMBJ technique as applied to thermoelectric studies was further improved by Widawsky *et al.*[78] who succeeded in simultaneously recording the electrical conductance and thermopower of single molecular junctions in STMBJ technique by measuring both the zero-bias thermocurrent and the electrical conductance under a small applied bias. Using this method, the authors explored several amine-Au linked and pyridine-Au linked molecular junctions. From these measurements they observed a positive Seebeck coefficient for amine-Au linked molecular junctions and a negative Seebeck coefficient for pyridine-Au linked molecular junctions, confirming that transport in amine-Au junctions is HOMO dominated whereas that in pyridine-Au junctions is LUMO dominated.

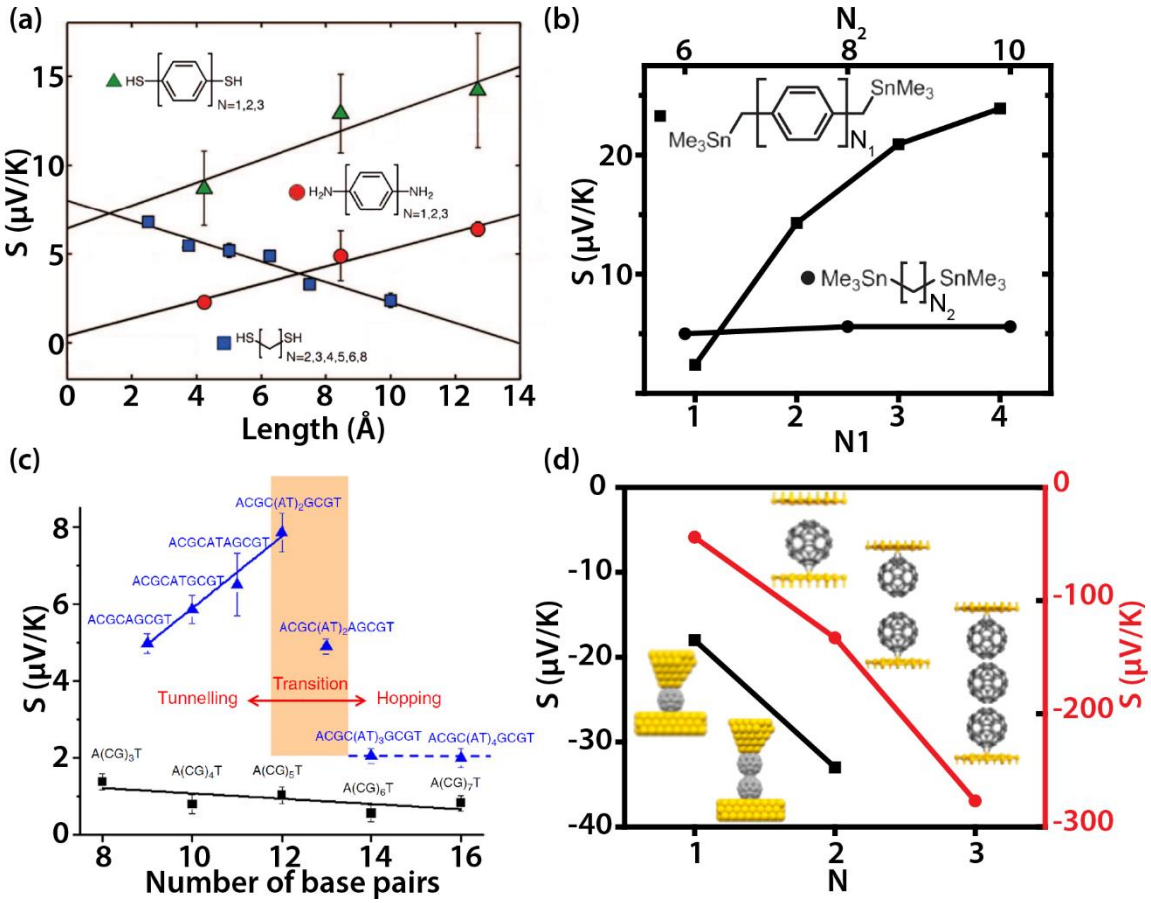

Figure 2-5 Length dependence of the Seebeck coefficient of molecular junctions. (a) Seebeck coefficient of phenylenedithiol (green triangle), phenylenediamine (red circle) and ADT (blue square) molecular junctions with respect to molecular length.[79] (b) Thermopower of $SnMe_3$ terminated polyphenyl (square, N_1) and $SnMe_3$ terminated alkane (circle, N_2) vs molecule length.[80] (c) Transition from tunneling to hopping regime of (CG) DNA molecules inserted with (AT) tunneling blocks (blue triangle).[81] (CG) sequence DNA molecules don't show transition behavior (black square). (d) Experimental (square, left axis) and computational (circle, right axis) results of C_{60} monomer, dimer and trimer (only computational data shown for trimers).[82]

In addition to the STMBJ technique, a different technique that is based on atomic force microscope (AFM) to probe thermoelectric effects in SAM molecular junctions was developed by Tan *et al.*[17]. Briefly, an Au-coated AFM probe made of Si, that is at ambient temperature, is placed in contact with a heated Au substrate that is covered with a monolayer

of molecules, while the deflection of the cantilever is continuously monitored and maintained at a constant value using feedback control (Fig. 2-4 b). The electrical conductance and the Seebeck coefficient of the tip-SAM-metal junctions are directly measured, respectively, by monitoring the current output under a small bias and measuring the voltage output under a temperature difference.

Mechanically controlled break junction (MCBJ) technique is another widely used experimental platform for probing the electrical and thermoelectric transport properties of molecular junctions. The first mechanical "break junction" experiment was conducted by Moreland and Ekin[83] for electron tunneling in superconductors. Later Muller and van Ruitenbeek[84] developed MCBJ technique in which a suspended metallic wire with a notch at the center is attached to a thin substrate (Fig. 2-4 c). Further, the flexible device is mounted in a three-point contact configuration. The center of the device is pushed by a piezoactuator whose motion can be controlled precisely by external bias. This process results in an elongation of the wire and eventually leads to the fracture of the wire at the notch, exposing clean metal surfaces. By controlling the motion of the actuator, the gap size between the electrodes can be systematically controlled allowing one to close and reopen the gap. Specifically, the displacement between the electrodes is a small fraction (also called reduction factor) of the displacement of the actuator due to the geometry of the MCBJ platform. This reduction factor enables very precise control in the separation of the electrodes with picometer scale stability. The superb stability of the MCBJ platform was extensively leveraged by researchers to create single atomic junctions by creating and gently breaking the contact between electrodes.

Reed *et al.*[12] applied the MCBJ technique to perform the charge transport measurements in organic molecule based molecular junctions for the first time. Briefly, they exposed the Au electrodes in an MCBJ setup to benzenedithiol (BDT) molecules. This enabled them to successfully trap BDT molecules between the Au electrodes. Given the stability of the MCBJ platform they were able to trap molecular junctions stably and perform electrical transport experiments in them. Subsequently, the MCBJ technique has been employed in studies of transport properties of molecular junctions and atomic junctions.[21, 85-90]

Tsutsui *et al*.[91] adapted the MCBJ technique for probing thermoelectric properties of molecular junctions by integrating a Pt serpentine heater into one of the electrodes that enabled them to apply temperature differences across molecular junctions (Fig. 2-4 c). Using this approach, the authors probed both the electrical conductance and the Seebeck coefficient of Au-BDT-Au junctions and reported that the transport properties are sensitive to the BDT configurations. They showed that upon mechanical stretching, in some cases, the molecule tilts towards the upright direction and Au-S bond are elongated, resulting in a weaker coupling to the contact and gradual shift of HOMO, accompanied by a decrease in conductance and a change (slightly increase or decrease) in Seebeck coefficient. In other cases, the configuration of the contact was dramatically changed, so that E_F shifts towards HOMO, leading to increased conductance and Seebeck coefficient.

2.5.2 Length Dependence of Thermopower in Molecular Junctions

Researchers have explored the dependence of the thermoelectric properties of molecular junctions on the molecular length. For Au-alkanedithiol (ADT)-Au junctions, the thermopower was found to vary linearly with increased N (N is the number of carbon atoms

in the backbone) (Fig. 2-5 a) while the conductance tends to decrease exponentially.[79] Specifically, for Au-phenylenediamine-Au[79] and Au-phenylenedithiol-Au[27, 79, 92] the thermopower increased linearly with length (Fig. 2-5 a). Similar results are found by Widawsky *et al.*[80] for trimethylstannylmethyl-terminated polyphenyls with 1-4 phenyl rings (P1-P4) (Fig. 2-5 b). However, they also found that the thermopower of trimethylstannyl-terminated alkanes with N = 6, 8 and 10 (C6, C8, and C10) was found to have little length dependence (Fig. 2-5 b). It was suggested[79] that the molecular backbone determined the length dependence of thermopower and the zero length thermopower is determined by the ending groups. Transmission in phenylenes is HOMO-determined, which sharpens and aligns closer to E_F with increased molecular length, resulting in higher thermopower. The transmission for alkanedithiols is strongly affected by Au-S metal induced gap states between HOMO and LUMO.

Length dependence of thermopower was also studied in junctions made from DNA molecules of different sequences (Fig. 2-5 c).[93, 81] For GC sequence double-stranded DNA molecules, the hole hopping transport mechanism lead to linearly increased resistance with molecular length. The Seebeck coefficient is small and weakly dependent on the length. When AT pairs, which are expected to act as a tunneling barrier, were inserted in the middle of GC sequence, both the conductance and thermopower behavior changed. When the number of inserted AT block base pairs m is smaller than 4, the resistance exponentially increased with the length of the block, and the Seebeck coefficient increases linearly and is large compared with GC molecule. When $m \geq 4$, the transport mechanism transition from tunneling to hopping, in which regime the resistance shows weak dependence on length, and Seebeck coefficient drops to small value.

The ability to acquire imaging of substrate in STMBJ enables the measurement in C_{60} dimer junctions. Evangeli *et al.*[82] trapped two C_{60} molecules to form a dimer by contacting a tip with one C_{60} molecule that has already been trapped to another molecule conjugated to the substrate (Fig. 2-5 d). They found that the thermopower of C_{60} dimer is approximately doubled compared to single C_{60} junctions, with a high Seebeck coefficient of -33 μV/K. Computational results suggested that the thermopower and *ZT* increased with the number of C_{60} monomers in the molecular chain due to the intermolecular interaction, showing the potential to improve thermoelectric properties by manipulating C_{60} junctions.

2.5.3 Effect of End Groups on Thermoelectric Molecules

The end groups bridging molecules to electrodes play an important role in charge transport and thermoelectric properties in molecules.[94-97] Experimental measurements of thiol-terminated aromatic molecular junctions showed a positive thermopower[34, 74, 75] while measurements of isocyanide-terminated junctions showed a negative thermopower[18]. In addition, experimental work on trimethyltin-terminated aromatic molecules[80] demonstrated slightly higher thermopower compared to thiol groups[18]. Balachandran *et al.*[96] provided a theoretical explanation for the end-group effects on thermopower of molecular junctions. Specifically, they investigated five different end groups (isocyanide, nitrile, amine, thiol and hydroxyl) which couple triphenyl molecule to Au electrodes (Fig. 2-6). It was found that isocyanide, nitrile and amine end-groups led to charge transfer out of the upon coupling with the electrodes, resulting in a downward shift of the energy levels, which positioned the HOMO peak closer to the Fermi energy. In contrast, thiol and hydroxyl end-groups resulted in charge transfer from the electrodes into the molecule, which led to a slightly downward shift in the energy levels placing the LUMO peak closer to the Fermi energy.

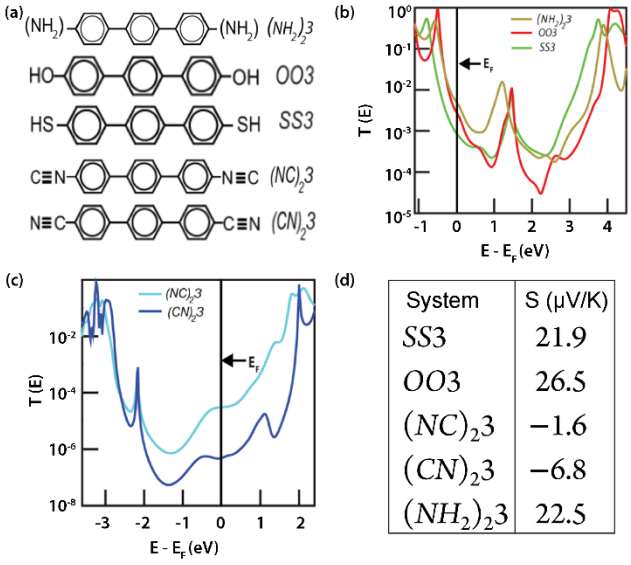

Figure 2-6 Theoretical results for triphenyl molecular junctions with five different end groups.[96] (a) Schematic of triphenyl molecules with five different end groups. (b) and (c) Transmission as a function of energy. For SS3, OO3, and $(NH_2)_2$3 molecules, the HOMO peak is closer to the E_F. For $(NC)_2$3 and $(CN)_2$3 the LUMO peak is closer to the E_F, resulting in a LUMO-dominated transport. (d) Calculated Seebeck coefficient for five types for triphenyl molecular junctions.

2.5.4 Effect of Chemical Structure, Conformation and Shape of Molecules

The effect of chemical structure on thermoelectricity of molecular junctions has been probed by adding electron-withdrawing/donating groups (fluorine, chlorine, and methyl) to BDT molecules (Fig. 2-7 a).[98] It was suggested that the presence of electron-withdrawing groups (fluorine and chlorine) on a BDT molecule shifts the energy levels of molecular junctions downwards, leading to a decreased thermopower, while the presence of electron-donating group (methyl) groups shift the energy levels upwards, leading to an increased thermopower. Since BDT has HOMO dominated charge transport properties, shifting the energy levels up (down) gives rise to a larger (smaller) slope in the transmission function at the Fermi level.

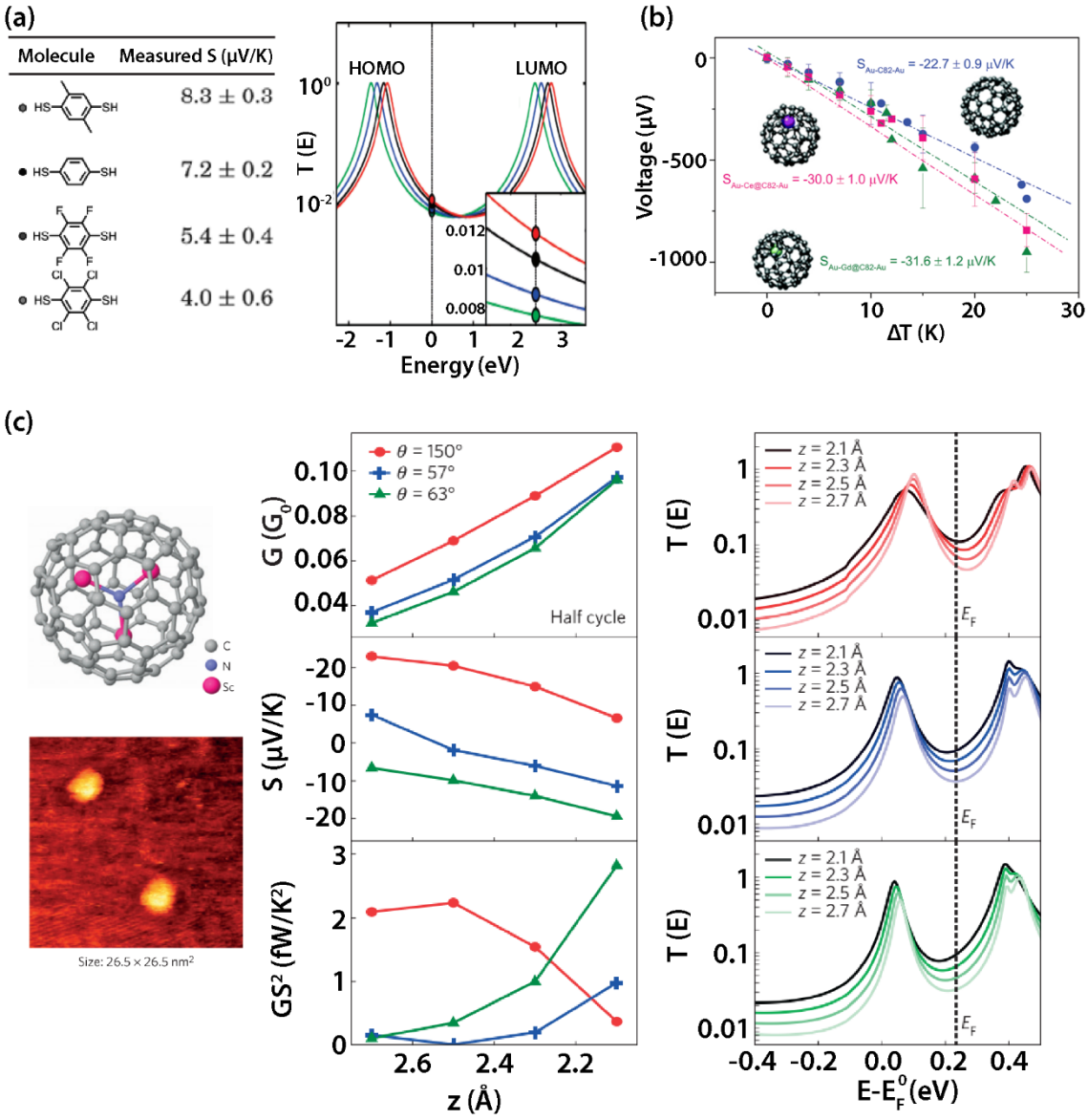

Figure 2-7 Effect of chemical structure, conformation and shape of molecules on thermoelectric properties of molecular junctions. (a) Thermoelectric properties of BDT based molecular junctions with substituents.[98] Left: Structure of BDT2Me, BDT, BDT4F, and BDT4Cl molecules (from top to bottom). Right: Lorentzian shaped transmission functions which illustrates how the transmission function is expected to change due to electron-withdrawing groups (BDT4F, blue line and BDT4Cl, green line, BDT, black line), and electron-donating groups (BDT2Me, red line). (b) Effect of shape on C_{82} derivative based junctions: C_{82} (blue circle), Gd@C_{82} (green triangle), Gd@C_{82} (red square).[99] (c) Effect of mechanical deformations of molecular junctions on their thermoelectric properties.[100] Left: Schematic of $Sc_3N@C_{80}$ molecule and two isolated $Sc_3N@C_{80}$ molecules under STM. Middle: Conductance, Seebeck coefficient and power factor (GS^2) as functions of pressing distance. Red circle, blue square and green triangle represents different molecule orientation

corresponding to the substrate. Right: Theoretical transmission functions vs. energy. Red, green and blue color represents different molecule orientation. Lighter colored line represents larger pressing distances.[100]

The effect of molecular conformation on the electrical conductance has also been studies by several groups.[101-103] For example, it was shown that in aromatic molecules, when the planes associated with each of phenyl rings are twisted from being "flat" ($\theta = 0°$, θ indication the twist angle between two benzene plates) to being "perpendicular" ($\theta = 90°$), the conductance decreases by a factor of 30.[101] The thermoelectric properties of molecular junctions created from fullerene based molecules was investigated by Lee *et al*.[99]. They experimentally investigated three fullerene derivatives (C_{82}, Gd@C_{82} and Ce@C_{82}) and found enhanced thermopower of Gd@C_{82} and Ce@C_{82} (Fig. 2-7 b). Computational analysis of the same systems suggested that this enhancement was due to the encapsulated metal atom that induced changes in the geometric and electronic structure of the fullerene molecule.

Researchers have also explored the effect of mechanical deformations of molecular junctions on their thermoelectric properties.[100] For example, by studying a Au-Sc_3N@C_{80}-Au junctions, where an Sc_3N molecule is imbedded into a C_{80} cage (Fig. 2-7 c), Rincon-Garcia *et al.*[100] found that the magnitude and the sign of thermopower both depend on the orientation of the molecule and applied force to the molecule. Further, computational analysis suggested that the introduced Sc_3N creates a sharp resonance near the Fermi energy, and the location of the peak in transmission function strongly depends on the molecular orientation and applied pressure, so the thermopower can exhibits both positive and negative sign, depending on the relative position of the transmission peak to the Fermi level. They emphasized that the

transport resonance plays an import role in thermoelectric performance and $Sc_3N@C_{80}$ can act as a bi-thermoelectric material.

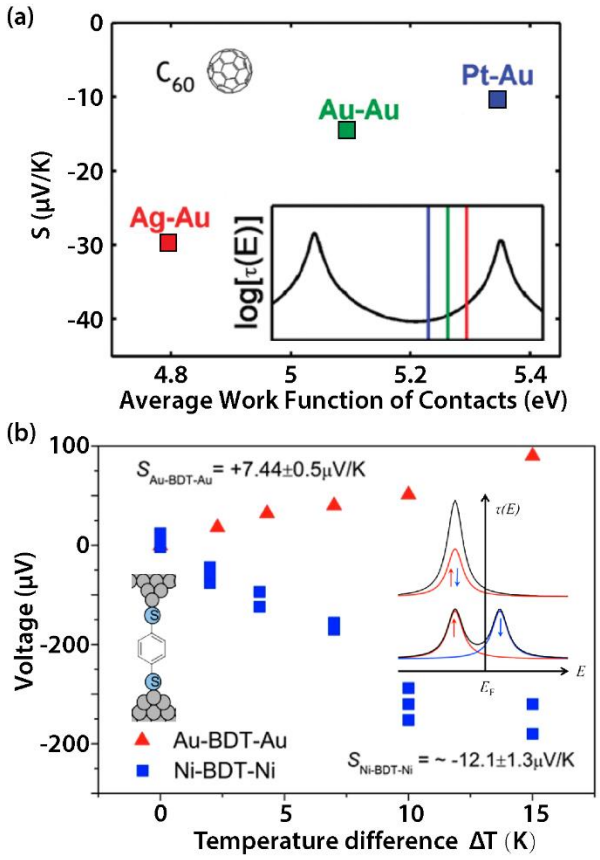

Figure 2-8 Effect of electrode materials on thermoelectric properties of molecular junctions. (a) Thermopower of Au-C_{60}-Au/Pt/Ag junctions vs. the average work function of electrodes. Inserted: Lorentzian approximation of the transmission function, where blue, green, and red vertical lines approximate the position of E_F for Au-Pt, Au-Au, and Au-Ag junctions.[104] (b) Plot of measured thermoelectric voltage of Au-BDT-Au (red triangle) and Ni-BDT-Ni (blue square) molecular junctions. Top inset: transmission function of Au-BDT-Au junction. Bottom inset: transmission function of Ni-BDT-Ni junction. Ni-BDT-Ni junction has a negative Seebeck coefficient (as opposed to the positive Seebeck coefficient of Au-BDT-Au junctions) due to spin-split hybridized states generated when BDT LUMO orbital coupled with Ni electrodes.[105]

2.5.5 Effect of Electrode Materials

Although gold is the prototypical electrode material in most molecular junction experiments, other metals have also been studied for potential interesting thermoelectric properties.[8, 56, 82, 106] The advantage of other electrode materials lies in their possibility of bringing the Fermi energy of electrodes closer to the orbital that dominates the charge transport properties of molecules due to modified work function of the electrode.[107, 108] Past work on fullerene based molecules (C_{60}, PCBM ([6,6]-Phenyl-C_{61}-butyric acid methyl ester) and C_{70}) (Fig. 2-8 a, showing C_{60} only) shows that the Seebeck coefficient is suppressed when one of the Au electrodes is replaced by Pt. In contrast, it was found that the Seebeck coefficient is doubled when one of the Au electrodes was replaced with Ag.[104] Enhancements in the Seebeck coefficient were also reported in experiments involving Ni electrodes. Computations revealed that these enhancements arise from the spin-split hybridized states that are generated when the HOMO orbital of the BDT molecule couples with Ni electrodes (Fig. 2-8 b).[105] In addition to these studies, computational work has pointed out that semiconducting electrodes and carbon nanotubes could suppress the "electron-like" contributions to the thermopower and cutoff the lower energy tails of HOMO transmission.[62] In these cases the output power of the systems was found to be greatly boosted.

2.5.6 Temperature Dependence of Thermopower in Molecular Junctions

According to Landauer formula, thermopower is expected to be linearly dependent on the average temperature of the molecular junction (see Eq. (2.3.5)). Kim *et al.*[109] varied the average temperature along the Au-BDT-Au molecular junctions and experimentally verified this prediction (Fig. 2-9). Since the figure of merit ZT is proportional to the power factor (G_eS^2)

and temperature T, and inversely proportional to the thermal conductance G_{th}, this work indicates that the values of ZT increase quadratically with temperature.

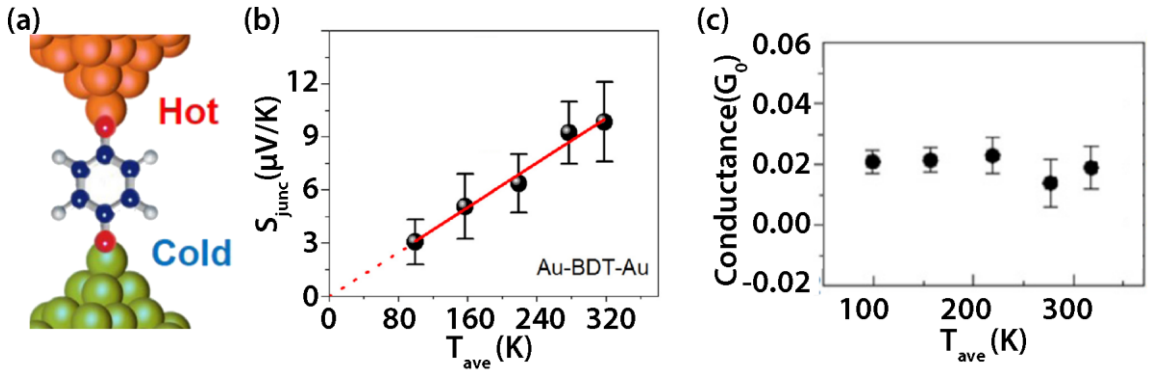

Figure 2-9 Temperature dependence of thermopower of molecular junctions.[109] (a) Schematic of Au-BDT-Au junction. (b) Plot of measured Seebeck coefficient as function of average temperature of the junction. Linear fit indicates that the Seebeck coefficient vanishes when the temperature tends to 0 K. (c) Plot of the electrical conductance as function of average temperature. The electrical conductance remains invariant with temperature.

2.5.7 Three-Terminal Thermoelectric Measurements

The key to improving the thermopower of a molecular junction is to shift a transmission function such that its maximum slope is located at Fermi energy. However, most measurements of thermoelectric properties of molecular junctions have relied on two-terminal measurements, which do not offer any control on the electronic structure of the junction. Past research[13, 20, 110-118] has shown that it is possible to create three-terminal devices that can tune the electronic structure of junctions via a gate electrode. These devices are often created by a process called electromigration which creates three-terminal molecular junctions by inserting molecules in nanometer-sized gaps formed during electromigration.[112, 119] In creating these devices, a gold nanowire is first fabricated using electron-beam lithography on a doped Si layer which is coated with a thin dielectric layer. Subsequently, a large electric current is

applied to the nanowire, causing the movement of metal atoms, which creates a nanometer or sub-nanometer sized gap in the nanowire. Molecules are deposited into the nanoscale gap by exposing the electrodes to molecules in a solution. The broken portions of the Au nanowire create two terminals (source and drain electrodes), while the Si back gate serves as a gate electrode. While several groups had used three terminal devices for tuning electrical transport, such devices could not be readily used for thermoelectric measurements due to the challenges in establishing temperature differences across the nanoscale gaped electrodes.

In order to overcome the limitations of two-terminal thermoelectric measurements, Kim *et al.*[22] created novel three-terminal devices based on EBJ and integrated electric heater in one electrode (source or drain) that allowed them to apply temperature differences across molecular junctions while electrostatically gating their electronic structure. Using such devices (Fig. 2-4 d), they probed the thermoelectric properties of Au-biphenyldithiol (BPDT)-Au and Au-C_{60}-Au junctions. These measurements revealed that the thermoelectric properties can be significantly improved when the dominant transport orbital is located closely to Fermi energy. In analyzing these experimental results, the transmission function of the junctions was approximated by a Lorentzian function. For both Au-BPDT-Au junction (Fig. 2-10 a), and Au-C_{60}-Au junctions (Fig. 2-10 b), the thermoelectric properties were found tunable by the applied gate voltage. This work demonstrated the feasibility of improving thermoelectric properties by tuning the electronic structure of molecular junctions.

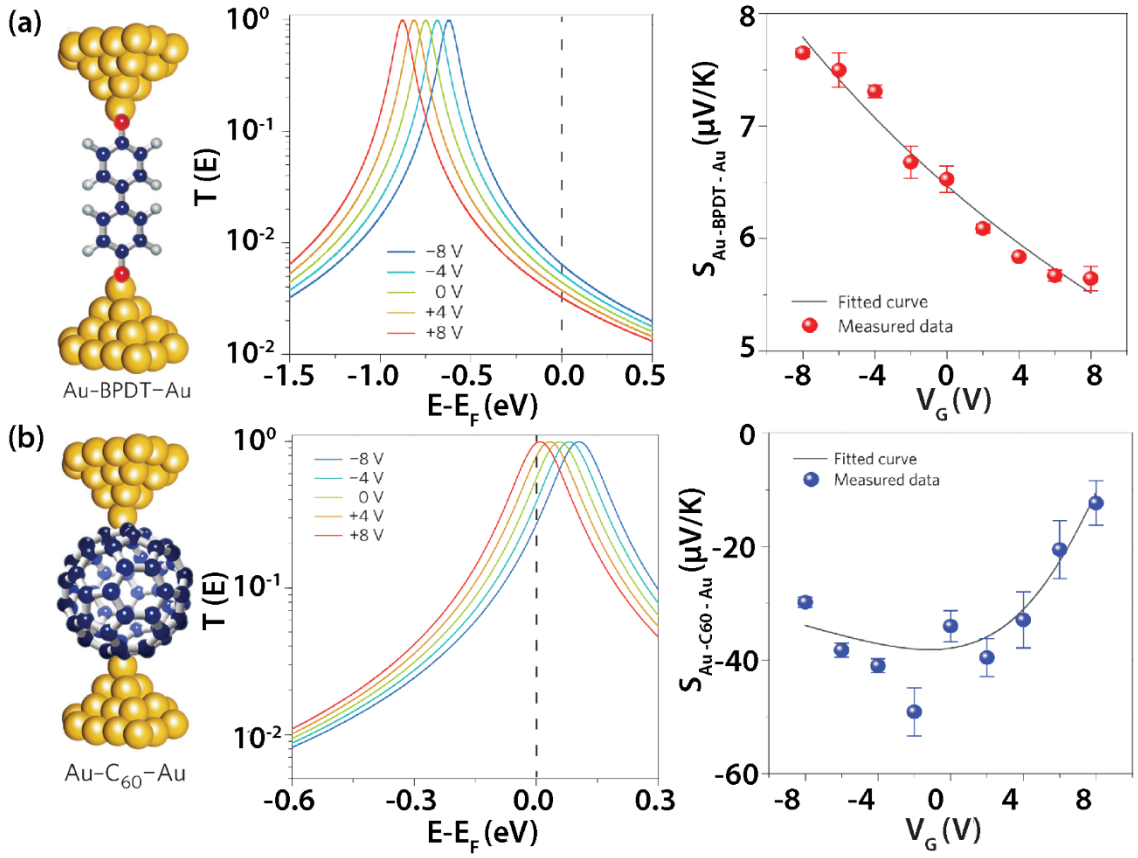

Figure 2-10 Electrostatic tuning of thermoelectric properties of MJs, Au-DBDT-Au (a) and Au-C_{60}-Au (b) junctions using three-terminal EBJ technique. Left: molecular junction structures. Middle: Lorentzian curves that approximate the transmission function when the gate voltage is varied from -8 V to +8 V. Right: Measured Seebeck coefficient as a function of gate voltage.[22]

Chapter 3 Influence of Quantum Interference on the Thermoelectric Properties of Molecular Junctions

Reproduced with permission from *Nano Letters*.

Ruijiao Miao, Hailiang Xu, Maxim Skripnik, Longji Cui, Kun Wang, Kim G. L. Pedersen, Martin Leijnse, Fabian Pauly, Kenneth Wärnmark, Edgar Meyhofer, Pramod Reddy, and Heiner Linke. *Nano Letters*, **18**, 5666-5672, (2018).

3.1 Abstract

Molecular junctions are promising candidates for developing electric devices at the molecular scale. Quantum interference effects in molecular junctions have been proposed as an avenue for highly efficient thermoelectric power conversion at room temperature. Towards this goal, we investigated the effect of quantum interference on the thermoelectric properties of molecular junctions. Specifically, we employed oligo(phenylene ethynylene) (OPE) derivatives with a *para*-connected central phenyl ring (*para*-OPE3) and *meta*-connected central ring (*meta*-OPE3), which both covalently bind to gold via sulfur anchoring atoms located at their ends. In agreement with predictions from *ab-initio* modelling, our experiments on both single molecules and monolayers show that *meta*-OPE3 junctions, which are expected to exhibit destructive interference effects, yield a higher thermopower (with around 20 μV/K) compared to *para*-OPE3 (with around 10 μV/K). Our results show that quantum interference

effects can indeed be employed to enhance the thermoelectric properties of molecular junctions at room temperature.

3.2 Introduction

Studies of the thermoelectric and electric properties of molecular junctions, created by bridging metallic electrodes by a single molecule or multiple molecules, not only reveal the fundamentals of charge transport through molecules, but also provide knowledge critical for developing molecule-based devices and their application in the field of energy conversion[5, 7, 10, 28, 31, 120, 121]. Recent computational studies have suggested that impressive thermoelectric performance, rivaling that of inorganic materials, can be obtained from molecular junctions by tuning their electronic transmission characteristics[22, 27, 82, 100, 122, 123]. A particularly intriguing approach is to take advantage of quantum interference effects that arise in conjugated molecules[37, 38, 60, 65, 124-128], for example by using destructive interference to block low-energy electrons, while allowing high-energy electrons to pass[60]. In this way, one may approximate the ideal transmission function for thermoelectric power conversion at high efficiency[39]. A corresponding performance increase in molecules at room temperature has been predicted[60].

While past experimental work has probed the electric and thermoelectric properties of molecular junctions in both two terminal[17-19, 27, 82, 98, 100, 109, 123, 129] and three terminal[22] configurations, the effects of quantum interference on the thermoelectric performance have remained unexplored. In this letter we ask the question: Is it possible to introduce, in a predictable manner, quantum-interference effects in molecular junctions such that the experimentally observed thermoelectric properties are enhanced? We use the following

approach: First, we introduce two specific molecules. While being isomerically similar, one of them is expected (based on modeling presented later) to show effects of destructive quantum interference, whereas the other one does not and can thus be used as a control. Subsequently, we will present our experimental results that indeed show a higher thermoelectric voltage in the presence of quantum interference, which is in quantitative agreement with expectations from DFT-based modelling of coherent quantum transport.

3.3 Experiments and results

The molecules we chose for our study are two OPE3 derivatives that feature different geometries at the central benzene ring (*para*- versus *meta*-connectivity, as shown in Figs. 3.1 a and 3.1 b). The choice of these two molecules is motivated by their expected different electron transmission characteristics. Specifically, the energy-dependent transmission in the gap between the highest occupied molecular orbital (HOMO) and the lowest unoccupied molecular orbital (LUMO) of *para*-connected junctions can be approximated by Lorentzians that are located at the HOMO and LUMO energies (Fig. 3-1 c). *Meta*-connected junctions, on the other hand, are expected to feature a sharp antiresonance dip in their transmission characteristics in this range due to destructive quantum interference effects, as a consequence of the phase difference between the HOMO and LUMO transport channels of *meta*-OPE3 (see Fig. 3-1 d)[130-132]. The resulting sharp feature in the transmission of *meta*-OPE3 is expected to lead to a larger Seebeck coefficient compared to *para*-OPE3 (see also computational results described below). The key question is now: Can this hypothesis regarding quantum-interference-related enhancement of the thermopower be experimentally confirmed?

To answer this question, we first measured the electrical conductance of OPE3-based

single-molecule junctions using a break-junction technique that relies on a custom-built ultra-stable scanning tunneling microscope (STM)[16, 76, 109] (Fig. 3-1 e). In these measurements, the OPE3-based molecules (whose synthesis is described in the Supporting Information (SI)) were first self-assembled onto a 7 mm × 7 mm sized template-stripped Au sample (150 nm thick), which was mounted into the STM. The STM tip was an electrochemically etched Au wire with a sharp tip, featuring a radius of around 30 nm[133]. In our experiments we first applied a 100 mV DC bias to the tip, while the Au substrate with the self-assembled monolayer on it was grounded. Molecular junctions were formed by reducing the separation between the tip and the sample until they contacted each other, resulting in an electrical resistance of less than 1 kΩ. Subsequently, the Au tip was withdrawn from the Au substrate at a speed of 1.6 to 3.2 nm/s, during which molecules were stochastically trapped between the tip and the sample. The formation of molecular junctions was reflected through steps and plateaus in the electrical conductance traces, measured by monitoring the tunneling current through the junction at a sampling rate of 1 kHz[134, 135]. The inset of Fig. 3-2 a shows representative conductance traces obtained in measurements of *para*-OPE3 junctions, where plateaus in the conductance frequently appear at around 10^{-4} G_0. In order to find the most probable conductance of the molecular junctions, we collected 2000 traces for *para*-OPE3 junctions and created histograms as shown in Fig. 3-2 a. It can be seen that the most probable conductance (as obtained from the peak of the histogram) is $(1.2 \pm 0.6) \times 10^{-4}$ G_0 for Au-(*para*-OPE3)-Au junctions. This result is close to that from Ref. 132 where the measured conductance is 2.8×10^{-4} G_0[136]. Results from experiments and a similar analysis on Au-(*meta*-OPE3)-Au junctions are shown in Fig. 3-2 b and reveal that their most probable electrical conductance is $(1.1 \pm 0.4) \times 10^{-5}$ G_0 – an order of magnitude smaller than those of the *para*-OPE3 junctions. This

difference is consistent with the expected destructive interference in *meta*-OPE3 junctions (see Fig. 3-1 d). It is also in agreement with the result in Ref. 132 where different end groups are used (pyridyl instead of thiol) and the conductance of the meta (~1.6 × 10^{-6} G_0) junction is almost an order of magnitude smaller conductance than that of the para junction (~3.1 × 10^{-5} G_0).

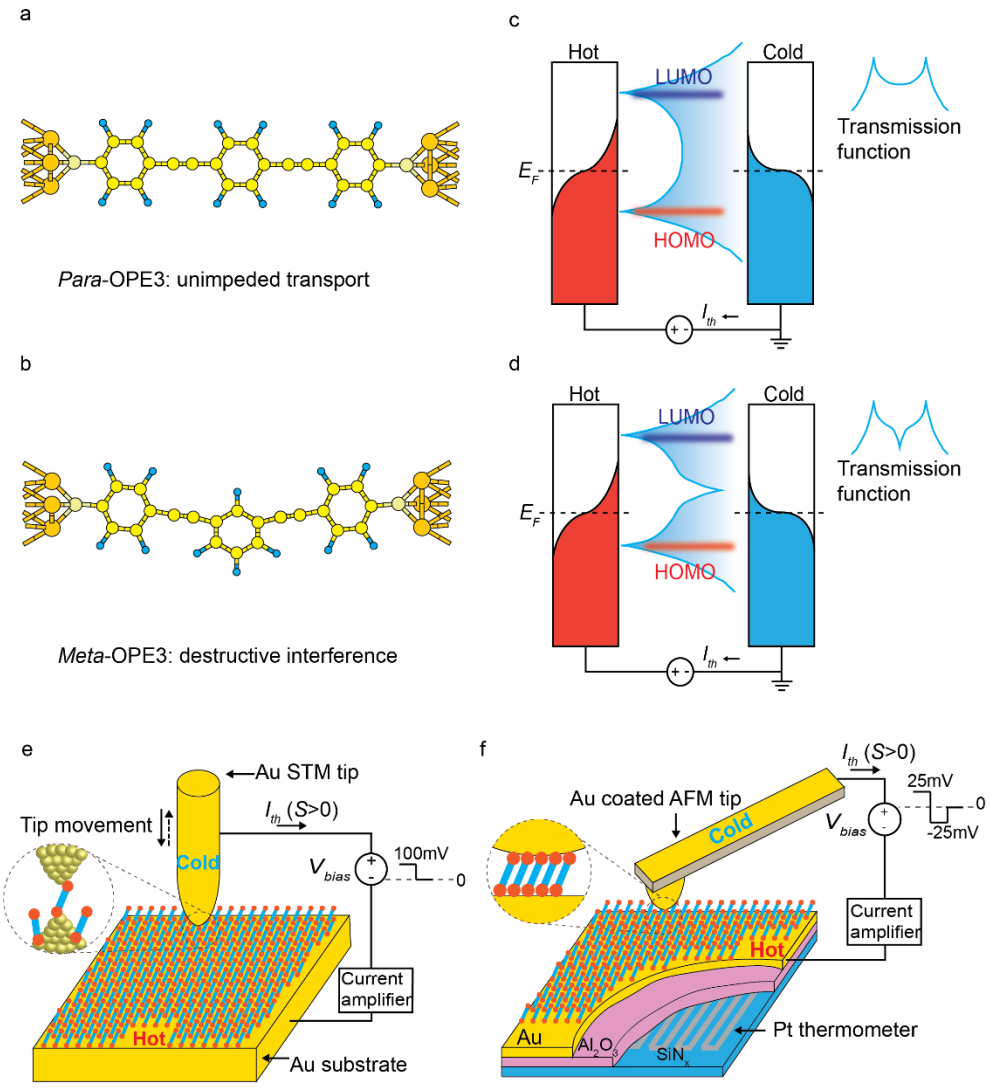

Figure 3-1 Schematics describing transport in molecular junctions and experimental approaches. a,b, Geometry of Au-(*para*-OPE3)-Au and Au-(*meta*-OPE3)-Au junctions, respectively. c, Schematic description of the origin of thermocurrent in a molecular junction in which charge transport is dominated by the HOMO level. The transmission function is to

be a sum of two Lorentzians. d, Thermocurrent in a molecular junction with destructive interference. The transmission shows sharp features, unlike a Lorentzian-type transmission. e, Schematic of the experimental setup based on an STM break junction. Molecules are trapped between the Au STM tip and Au substrate when the tip repeatedly approaches the substrate and withdraws from it. A voltage bias is applied and the current is monitored to evaluate the conductance. In thermoelectric measurements the substrate is heated to the desired temperature and the tip is kept at ambient temperature. No voltage bias is applied to the junction and the thermocurrent is recorded to estimate the thermoelectric voltage. The inset shows the formation of a single-molecule junction. f, Schematic of the experimental setup employed for measuring the thermoelectric properties in a many-molecule junction. It is based on an AFM, where a Au-coated cantilevered probe makes contact with a molecular monolayer self-assembled on gold. The inset shows a many-molecule junction. The direction of the thermocurrent I_{th} in panels a, b corresponds to a positive sign of the Seebeck coefficient.

In order to measure the thermopower of single-molecule junctions, we created a stable temperature difference ($\Delta T \approx 0$, 15, 30 or 45 K) between the tip and sample by heating the sample holder via an integrated heater. The substrate temperature was monitored via a diode temperature sensor located on the sample holder. The tip was maintained at room temperature (around 295 K). When performing measurements at a given temperature differential ΔT, a single-molecule junction was created following the same approach employed in the electrical conductance measurements, but with a reduced tip withdrawal speed of 0.2 nm/s. In order to perform thermoelectric measurements, the withdrawal of the tip was stopped when the electrical conductance reached the most probable conductance value as determined from the measurement data shown in Figs. 3.2 a and 3.2 b. Once the electrical conductance reached the desired value, we switched the bias applied to the tip with respect to the grounded sample from 100 mV to 0 V and monitored the thermocurrent I_{th} resulting from the applied ΔT via a current amplifier for a period of 100 to 500 ms. To confirm the integrity of the junction, we switched back to the 100 mV bias for 100 to 500 ms and checked if the electrical conductance was within a few percent of the most probable electrical conductance (see Chapter 3.4 for a

detailed description of this process). If the conductance was not within a few percent of the most probable value, the experiment was terminated and the data from this measurement was discarded. This process of switching the bias from 100 mV to 0 V and back again to 100 mV was repeated until the single-molecule junction spontaneously broke. By performing many (on the order of several hundred) measurements like this we could collect the thermocurrent at each temperature differential $\Delta T = T_{substrate} - T_{tip}$. The obtained I_{th} is treated as positive, when the current flows from the tip (via the molecule) to the substrate, and negative, when it flows in the opposite direction. I_{th} was converted into a thermoelectric voltage ($\Delta V_{th} = V_{substrate} - V_{tip}$) by dividing $-I_{th}$ by G, that is, by the electrical conductance of the junctions before the withdrawal was stopped (see SI for a discussion of the sign of I_{th}). Histograms built from the thermoelectric voltage, collected at several temperature differentials, are shown in Fig. 3-2 c for *para*-OPE3 junctions and in Fig. 3-2 d for *meta*-OPE3 junctions. Similar measurements were also performed on benzenedithiol junctions, which have been studied in the past[27, 109, 137] and were repeated here as control experiments (shown in Chapter 3.4). Finally, in Figs. 3.2 e and 3.2 f we present the most probable thermoelectric voltages from the histograms as a function of the applied temperature differential. The thermopower of the molecular junction is given by:

$$S_{junc} = S_{Cu} - \frac{\Delta V_{th}}{\Delta T} \tag{3.3.1}$$

where S_{Cu} = 1.94 μV/K is the Seebeck coefficient of bulk copper at T = 300 K (see Chapter 3.4 for details).

The Seebeck coefficients obtained from the thermopower slopes in Figs. 2e and 2f are 10.8 ± 9.5 μV/K and 20.9 ± 15.4 μV/K for the Au-(*para*-OPE3)-Au and Au-(*meta*-OPE3)-Au junctions, respectively. The positive sign in the Seebeck coefficient of OPE3-based junctions reveals that transport is hole-dominated. Remarkably, the thermopower of the Au-(*meta*-OPE3)-Au junction is twice as large as the thermopower of the Au-(*para*-OPE3)-Au junction. The data from single-molecule-junction Seebeck-coefficient measurements (shown in Figs. 3.2 c-f) thus suggest that quantum interference effects can enhance thermoelectric properties. It should however be noted that there is a large spread in the thermoelectric voltages reported in Figs. 3.2 c and 3.2 d (as also reflected in Figs. 3.2 e and 3.2 f), possibly due to the intrinsic variability in the electronic structure of the junctions.

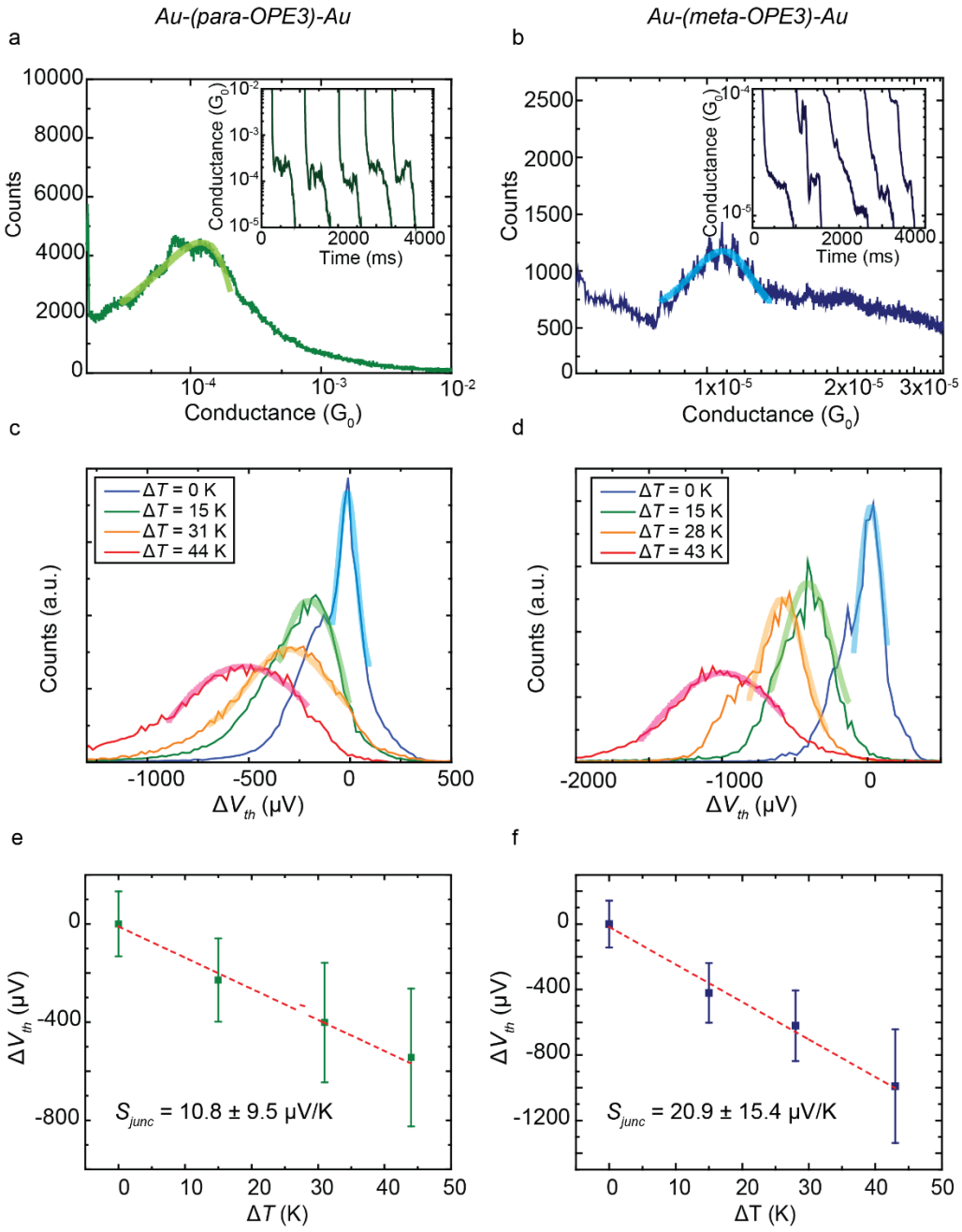

Figure 3-2 Results of single-molecule junction experiments with Au-(*para*-OPE3)-Au (left column) and Au-(*meta*-OPE3)-Au (right column), respectively. a,b, Conductance histograms, generated without data selection from 2000 traces. The curved lines show Gaussian fits. The insets display representative traces (tip speed 3.2 nm/s). c,d, Distribution of thermoelectric voltages at a series of ΔT as indicated. Shaded curves represent Gaussian fits. e,f, Thermoelectric voltage as a function of ΔT. Red dashed lines are linear fits.

In order to ensure that our conclusions about the Seebeck coefficient are robust, we applied an approach developed by us in the past[18] that enables measurements of thermoelectric properties of junctions involving multiple molecules. These ensemble measurements are expected to present lower variability due to the averaging over junction geometries. In this method, the molecules were self-assembled onto Au substrates (see the Chapter 3.4 for a characterization of monolayers). Subsequently, an Au-coated atomic force microscopy (AFM) probe was placed in gentle contact with the molecule-coated Au surface at a pushing contact force of around 1 nN (see Fig. 3-1 f). In order to measure the electrical conductance, the voltage bias across the molecular junction was varied from -0.5 V to 0.5 V and the current flowing through the junction (I) was measured[16]. The measured I-V curves are shown in Figs. 3.3a,b and indicate that the low-bias conductances for Au-(*para*-OPE3)-Au junctions and Au-(*meta*-OPE3)-Au junctions are 3.8×10^{-2} G_0 and 1.9×10^{-3} G_0, respectively. The measured low-bias conductance is consistent with the expectation of roughly 100 molecules in the junction, when compared to the corresponding most probable single-molecule conductance.

Next, we determined the thermoelectric properties by varying the temperature differential ΔT from 0 to 3 K, while measuring I_{th} across the junction with the substrate grounded. The measured thermocurrent was converted into a thermoelectric voltage (similar to what was done in the single-molecule measurements, i.e. by dividing $-I_{th}$ by the electrical conductance), which is shown as a function of the applied temperature differential in Figs. 3.3 c and 3.3 d for Au-(*para*-OPE3)-Au and Au-(*meta*-OPE3)-Au junctions, respectively. Finally, using Eqn. 1 the Seebeck coefficient for the Au-(*para*-OPE3)-Au and Au-(*meta*-OPE3)-Au junctions is determined to be 8.0 ± 0.8 μV/K and 22.5 ± 1.1 μV/K respectively. The measured data confirm the conclusion from our single-molecule measurements that the Seebeck coefficient of *meta*-OPE3 junctions is over two times that of the *para*-OPE3 junctions.

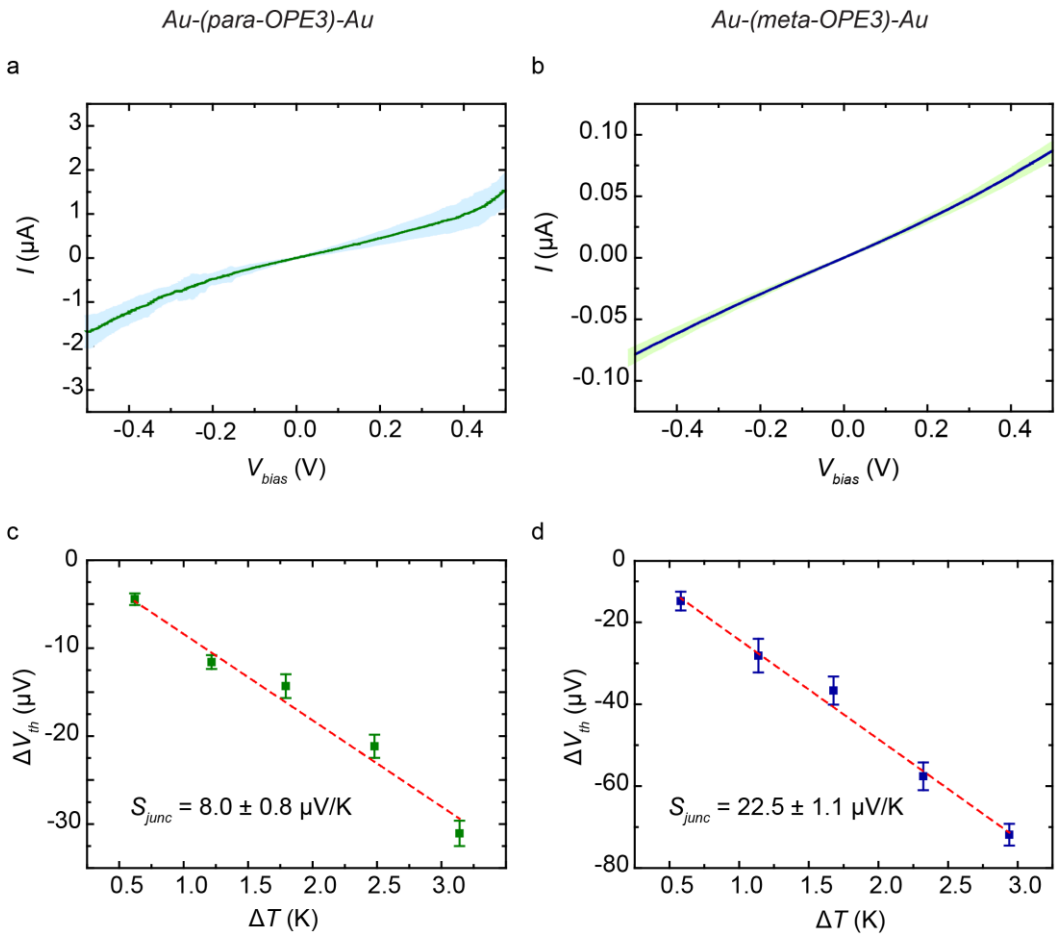

Figure 3-3 Results for monolayer measurements of Au-(*para*-OPE3)-Au (left column) and Au-(*meta*-OPE3)-Au junctions (right column), respectively. a,b, *I*-*V* characteristics obtained by averaging 50 individual *I*-*V* curves. The shaded regions represent the standard deviations. c,d, Thermoelectric voltage as a function of ΔT. Red dashed lines are linear fits.

To compare the measurements to theoretical expectation, we describe the electric and thermoelectric transport properties via the Landauer-Büttiker scattering theory of phase-coherent transport through nanostructures[1]. The central quantity in this approach is the energy-dependent transmission function $\tau(E)$. While we evaluate both the electrical conductance, G, and the thermopower, S_{junc}, exactly via energy integrals (see the SI for details), the following low-temperature expressions provide an excellent approximation[48]:

$$G = G_0\tau(E_F)\ and\ S_{junc} = -\frac{\pi^2 k_B^2 T}{3e}\frac{dln\tau(E)}{dE} \tag{3.3.2}$$

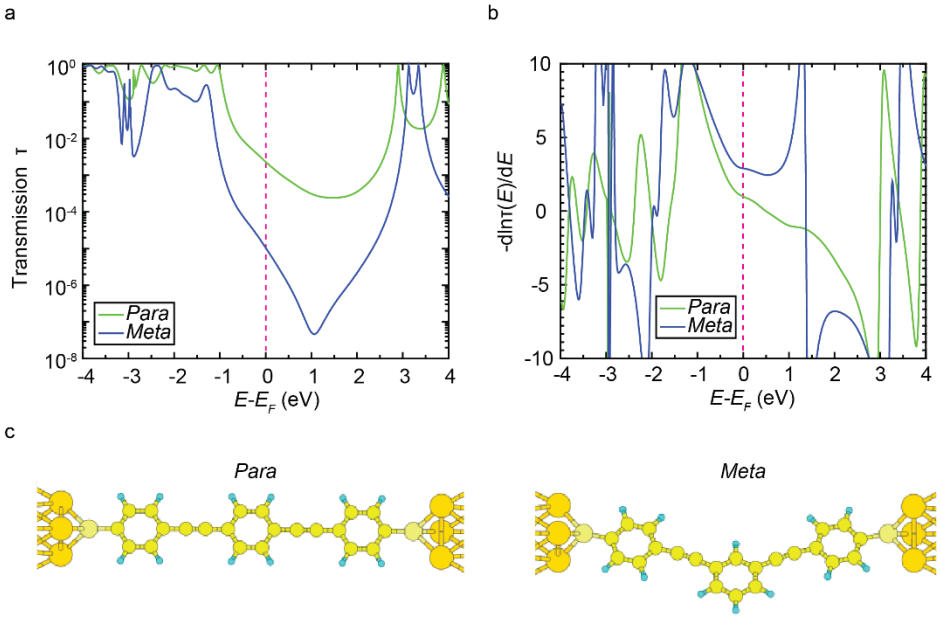

Figure 3-4 Theoretical computational results for Au-(*para*-OPE3)-Au and Au-(*meta*-OPE3)-Au from DFT+Σ calculations. a, Transmission curves. b, Negative derivatives of the logarithm of the transmission curves. These are proportional to the thermopower. c, The single-molecule junction geometries considered in our DFT+Σ calculations for the para and the meta molecular junctions.

In order to evaluate $\tau(E)$, we express the transmission in terms of Green's functions and use information on the electronic structure, as determined from density functional theory (DFT)[138, 139]. These DFT calculations, which we also employ to determine stable contact geometries through energy optimization, were carried out with TURBOMOLE[140]. Since the actual energies of HOMO and LUMO levels with respect to the Fermi energy are crucial in the studied systems, we applied the DFT+Σ correction to overcome well-known shortcomings of DFT with regard to level alignments[55, 141]. We have studied different contact geometries, where the sulfur anchoring atoms at both ends of the molecules bind either to a single or three

gold atoms (see Chapter 3.4). The transmission curves for those junctions, where the sulfur atoms bind to three gold atoms, are shown in Fig. 3-4 a. The antiresonance in the Au-(*meta*-OPE3)-Au junction is located around 1.3 eV above the Fermi energy E_F, while it is absent for Au-(*para*-OPE3)-Au. Following from the transmission at E_F, the calculated electrical conductance is 1.8×10^{-4} G_0 for Au-(*para*-OPE3)-Au and 3.85×10^{-6} G_0 for Au-(*meta*-OPE3)-Au. Compared to the experiment, these values differ by a factor of 1.8 and 0.32, respectively. Between *para* and *meta* configurations we see a significant difference in the derivatives $-d\ln\tau(E)/dE$ at the Fermi energy (Fig. 3-4 b) and therefore in the Seebeck coefficients, which we find to be 7.31 µV/K for Au-(*para*-OPE3)-Au and 21.4 µV/K for Au-(*meta*-OPE3)-Au, respectively. The calculated Seebeck coefficients are thus within the experimental uncertainties. Our *ab-initio* modeling suggests that the doubling of the measured thermopower for Au-(*para*-OPE3)-Au junctions, in comparison to the Au-(*meta*-OPE3)-Au junctions, is due to the increased slope of the logarithm of the transmission function at E_F, as expected from destructive quantum interference effects.

3.4 Methods

3.4.1 Molecule Synthesis Process
General Information

All reactions were carried out under an atmosphere of nitrogen unless otherwise indicated. Anhydrous THF was distilled from sodium/benzophenone ketyl prior to use. All other solvents were technical grade unless noted. The following reagents, $PdCl_2(PPh_3)_2$ (Acros), $Pd(dba)_2$ (Aldrich), CuI (99.99%, Aldrich), PPh_3 (99%, Acros), triethylamine (99%, Acros),

DIPEA (99.5%, Aldrich), TMSA (Aldrich) and K_2CO_3 (99%, Aldrich) were purchased and used as received. The following compounds *1a*, *1b*, and *para*-OPE3 were synthesized according to the literature (Scheme 1)[1,2]. Column chromatography was performed using silica gel 230-300 mesh (purchased from Aldrich) as the solid support. All NMR spectra were recorded on a Bruker Avance 400 MHz spectrometer. ^{1}H NMR and ^{13}C NMR chemical shifts are reported in δ units, parts per million (ppm) relative to the chemical shift of residual solvent. Deuterated solvents were used as received from Aldrich. Reference peaks for chloroform in ^{1}H NMR and ^{13}C NMR spectra were set at 7.27 ppm and 77.0 ppm, respectively. The melting point was recorded on a micro melting point apparatus SMP3 (Stuart Scientific, UK). FTIR spectra were recorded on a Bruker FTIR spectrometer Alpha II. Electron-spray ionization high-resolution mass (ESI–HRMS) spectra were recorded on a Waters Micromass Q-Tof micro mass spectrometer. Elemental analyses were performed by Mikroanalytisches Laboratorium KOLBE (Mülheim an der Ruhr, Germany).

Details of Synthesis of *meta*-OPE3

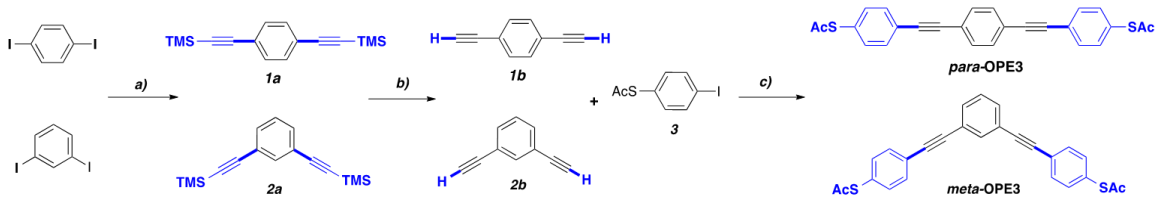

Figure 3-5 Synthesis of *para*-OPE3 and *meta*-OPE3. a) $HCCSi(CH_3)_3$, $PdCl_2(PPh_3)_2$, CuI, TEA, reflux, 8 h, for *1a*, 85%; *2a*, 86%; b) K_2CO_3, MeOH, CH_2Cl_2, room temperature, for *1b*, 93%; *2b*, 90%; c) $Pd(dba)_2$, CuI, PPh_3, DIPEA, THF, 50 °C, 24 h, for *para*-OPE3, 86%; *meta*-OPE3, 82%.

1,3-Bis(trimethylsilylethynyl)benzene (*2a*). Following the literature[1], 1,3-diiodobenzene (3.67 g, 100 mol%, 11.1 mmol) was dissolved in triethylamine (150 ml) under a nitrogen atmosphere. Copper(I) iodide (30 mg, 1.42 mol%, 0.158 mmol) and dichlorobis(triphenylphosphine)palladium(II) (60 mg, 0.77 mol%, 0.085 mmol) were added to the stirred solution. Trimethysilylacetylene (3.28 g, 300 mol%, 33.3 mmol) was dropped in and the mixture was heated to reflux for 8 h. After cooling, the formed precipitate of diethylamine hydroiodide was filtered off and washed with dichloromethane. The combined filtrates were evaporated under a reduced pressure, and the residue was chromatographed on a column (SiO_2, 5% EtOAc in PE) to yield ***2a*** as a light yellow solid (2.58 g, 9.55 mmol, 86%).

^{1}H NMR ($CDCl_3$, 400 MHz): δ 7.60 (t, *J* = 1.6 Hz, 1H), 7.40 (dd, *J* = 8.0 and 1.6 Hz, 2H), 7.24 (t, *J* = 8.0 Hz, 1H), 0.25 (s, 18 H). ^{13}C NMR ($CDCl_3$, 100 MHz): δ 135.4, 131.7, 128.2, 123.3, 104.0, 94.9, 0.11.

1,3-Diethynylbenzene (*2b*). Following the literature[2], ***2a*** (2.57 g, 100 mol%, 9.50 mmol) was dissolved in methanol (40 mL) and dichloromethane (40 mL), and potassium carbonate (7.88 g, 600 mol%, 57.0 mmol) was added. The mixture was stirred at room temperature before being poured into water. The solution was extracted with ether and washed with brine. After drying over magnesium sulfate, the solvent was evaporated in vacuo to afford ***2b*** as a dark yellow oil (1.08 g, 8.55 mmol, 90%).

^{1}H NMR ($CDCl_3$, 400 MHz): δ 7.63 (t, *J* = 1.6 Hz, 1H), 7.47 (dd, *J* = 7.6 and 1.6 Hz, 2H), 7.30 (t, *J* = 8.0 Hz, 1H), 3.10 (s, 2 H). ^{13}C NMR ($CDCl_3$, 100 MHz): δ 135.6, 132.3, 128.4, 122.5, 82.5, 77.9.

1,3-Bis(4-acetylsulfanyl-phenylethynyl)benzene (*meta*-OPE3). Following the literature[2], to a flame-dried vessel were added *compound 3* (0.31 g, 200 mol%, 1.10 mmol), *2b* (0.07 g, 100 mol%, 0.55 mmol), $Pd(dba)_2$ (0.0317 g, 10 mol%, 0.055 mmol), PPh_3 (0.0721g, 50 mol%, 0.28 mmol), CuI (0.0105 g, 10 mol%, 0.055 mmol), well-degassed *i*-Pr_2NEt (1 mL) and THF (4 mL). The vessel was sealed and allowed to stir at 50 ^oC for 1 day. The reaction mixture was then poured into water, and the aqueous layer was extracted three times with dichloromethane. After drying the combined organic layers over magnesium sulfate, the solvent was removed in vacuum to afford a crude product. The crude product was purified by column chromatography (SiO_2, 15% EtOAc in PE) to provide *meta*-OPE3 as a light yellow solid (0.19 g, 0.45 mmol, 82%).

mp 148-149 ^oC. FTIR (neat): ν (cm^{-1}) 3058, 2923, 1913, 1697, 1593, 1490, 1398, 1354, 1265, 1117, 1011, 960, 896, 828, 795, 732, 682, 627, 603, 543, 471, 442. ^1H NMR ($CDCl_3$, 400 MHz): δ 7.73 (s, 1H), 7.57 (d, J = 8.0 Hz, 4H), 7.52 (dd, J = 7.6 and 1.2 Hz, 2H), 7.42 (d, J = 8.4 Hz, 4H), 7.36 (t, J = 8.0 Hz, 1H), 2.45 (s, 6H). ^{13}C NMR ($CDCl_3$, 100 MHz): δ 193.3, 134.7, 134.2, 132.2, 131.6, 128.5, 128.3, 124.2, 123.3, 90.1, 89.3, 30.3. HRMS (ESI) calc. for $C_{26}H_{18}O_2S_2$ ($M+H^+$): 427.0826; Found: 427.0828. Elemental Analysis calc. for $C_{26}H_{18}O_2S_2$: C 73.21, H 4.25, S 15.03; Found: C 73.24, H 4.38, S 14.82.

Spectral Data for New Compounds

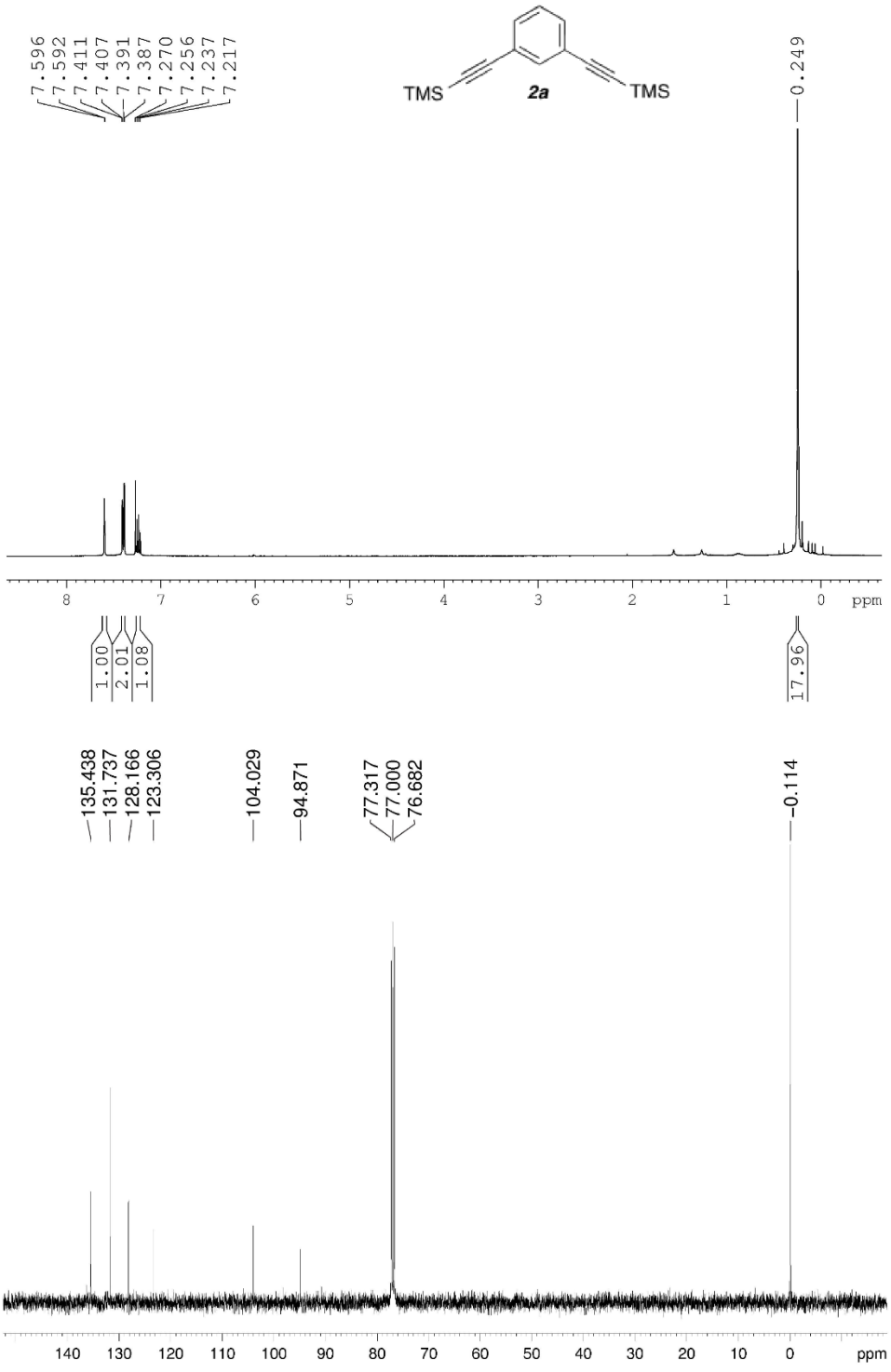

Figure 3-6 ^{1}H (top) and ^{13}C (bottom) NMR data for compound *2a*.

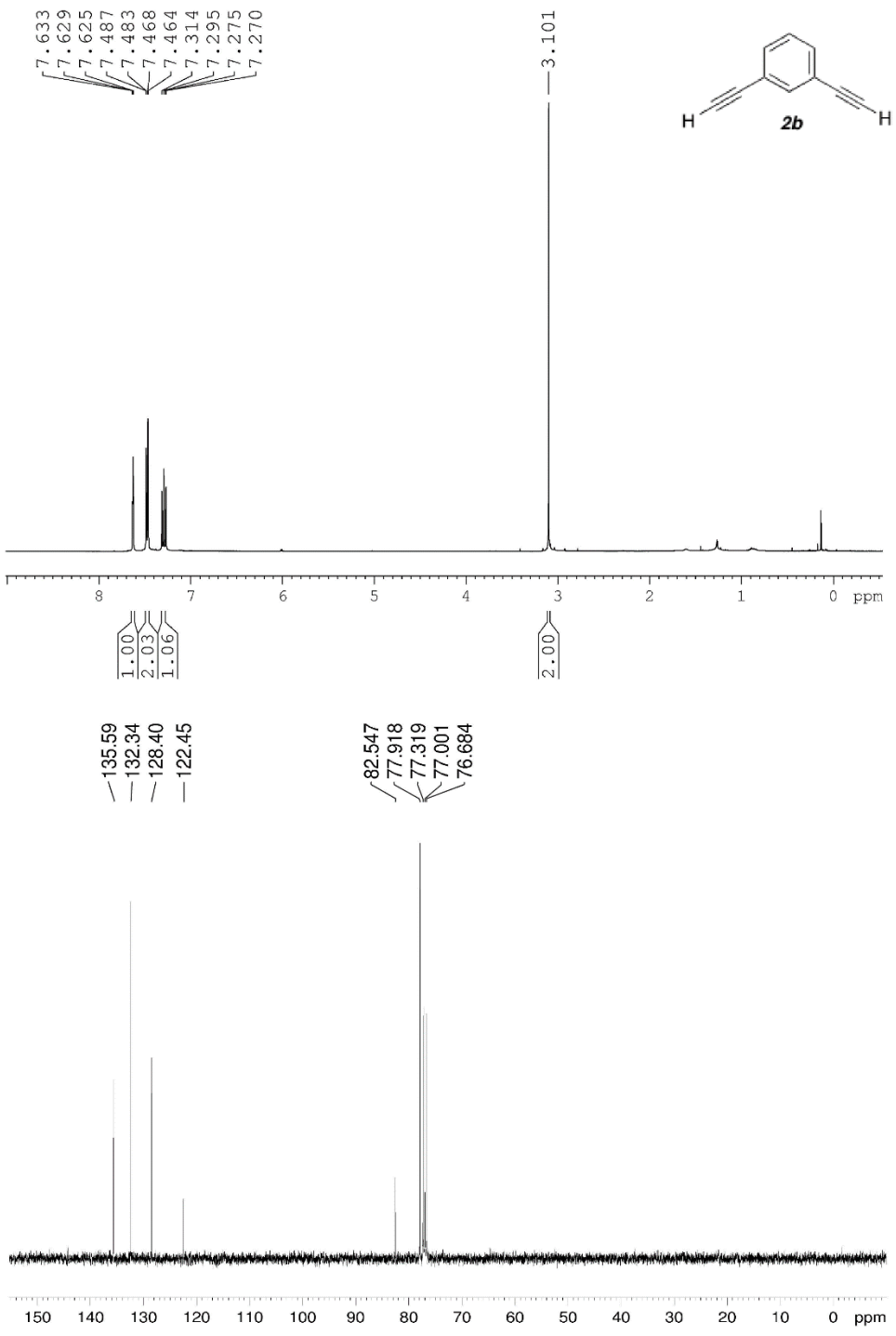

Figure 3-7 ^{1}H (top) and ^{13}C (bottom) NMR data for compound *2b*.

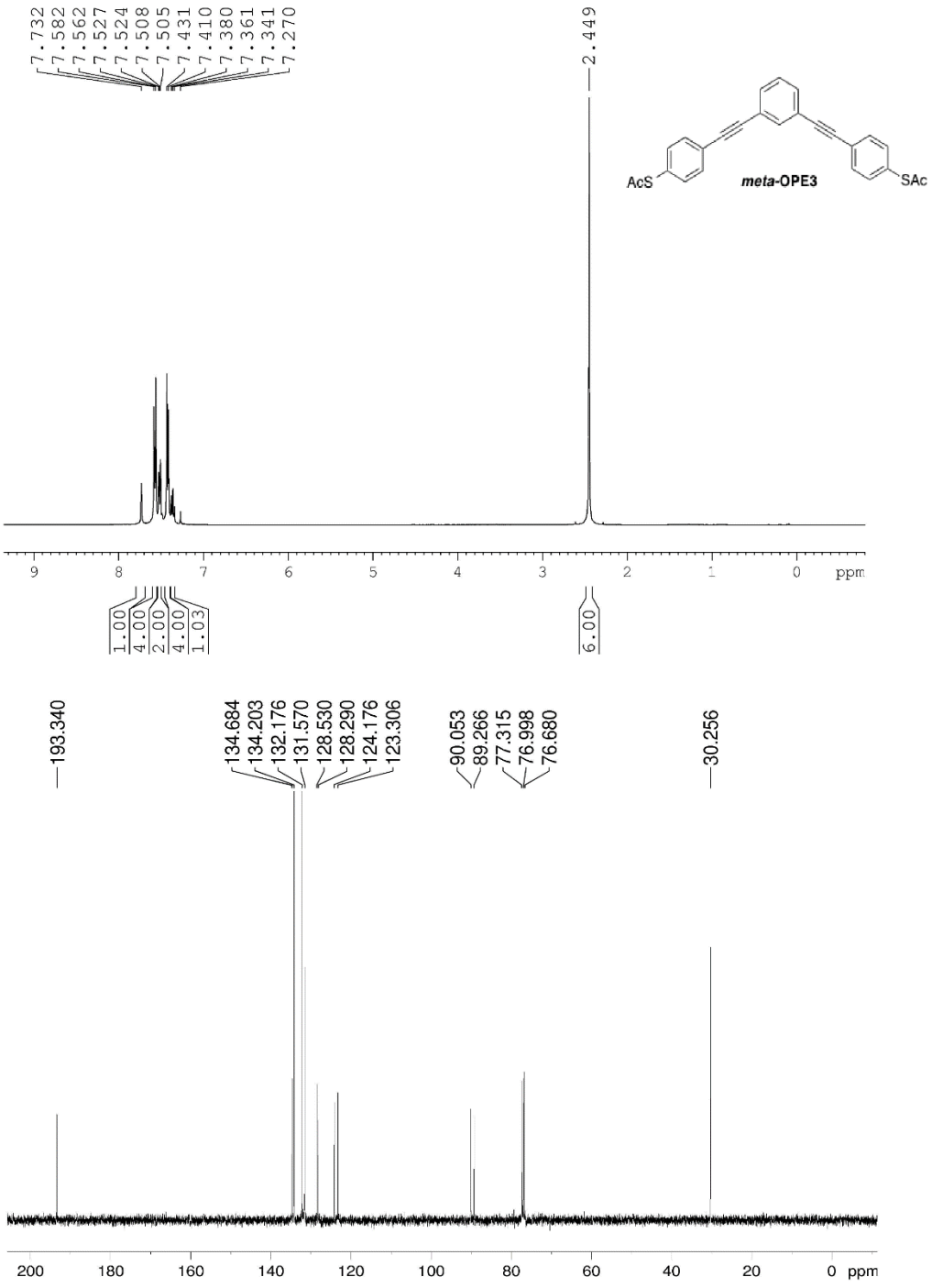

Figure 3-8 ^{1}H (top) and ^{13}C (bottom) NMR data for *meta*-OPE3.

3.4.2 Calculation Details

We used the Landauer-Büttiker formalism of phase-coherent elastic transport to describe electric and thermoelectric properties of single-molecule junctions and to compare to the experiment.[3] In this formalism, the electrical conductance G and the Seebeck coefficient S_{junc} are expressed as

$$G = G_0 K_0 \; and \; S_{junc} = \frac{-K_1}{eTK_0} \tag{3.4.1}$$

where the coefficients K_n are given by

$$K_n = \int_{-\infty}^{\infty} dE\tau(E) \frac{-\partial f(E)}{\partial E} (E-\mu)^n \tag{3.4.2}$$

with the transmission function $\tau(E)$, the Fermi-Dirac distribution function $f(E)$ and the chemical potential μ, which we approximate by the Fermi energy E_F.

We used electronic structure information extracted from density functional theory (DFT) to evaluate the transmission with the help a proprietary framework based on Green's functions[4]. Working with the TURBOMOLE code[5], we employed DFT at the same time to determine stable junction geometries. We considered Au-(*para*-OPE3)-Au and Au-(*meta*-OPE3)-Au junctions along with two kinds of leads or molecule-electrode binding types. These were top-top, where each sulfur atom binds to one electrode tip atom, and hollow-hollow, where each sulfur binds to three lead atoms. Proceeding along the lines of Ref. 6, each of the four resulting systems was defined in the following way: The molecule was attached to one lead of the particular type and terminated with one gold atom at the opposing sulfur. After structural relaxation the single gold atom was replaced by the second gold lead in a symmetric

way. The system was then relaxed again to obtain the final junction geometry. To mimic electrodes, whose transport direction is oriented along the ⟨111⟩ crystallographic direction, we used clusters of 20 or 19 Au atoms on the left and the right of the molecule for top-top and hollow-hollow configurations[6]. In all of the previously discussed relaxations, we kept in every step the two layers of each electrode cluster fixed that were most distant from the molecule, imagining them to belong to the "bulk" part of the electrode[6]. This yielded the central part of the final junction geometries shown in Fig. 3-9, while the fixed parts of the electrodes were treated as surfaces of semi-infinite perfect crystals in the subsequent transmission computations[4,6]. Throughout our DFT calculations, we used the def-SVP basis set[7] and the PBE functional[8]. The total energy was converged to better than 10^{-6} a.u. and the maximum norm of the Cartesian gradient to below 10^{-3} a.u.

For the energy corrections of occupied and virtual states in the self-energy-corrected density functional theory (DFT+Σ) we proceeded as described in literature[9]. The total correction for all occupied and all unoccupied states is Σ_{occ}=-IP-ϵ_H+Δ_{occ} and Σ_{virt}=-EA-ϵ_L+Δ_{virt}, respectively. In the expressions, the ionization potential (IP) and electron affinity (EA) are defined as IP = $E_{tot}(Q = +e) - E_{tot}(Q = 0)$ and EA = $E_{tot}(Q = 0) - E_{tot}(Q = -e)$, where $E_{tot}(Q)$ is the total energy of the gas-phase molecule with charge Q, $\epsilon_{H/L}$ are the Kohn-Sham HOMO/LUMO energies of the gas-phase molecule, and $\Delta_{occ/virt}$ describe the stabilization of HOMO/LUMO charge distributions on the molecules by image charges in the electrodes. The particular values for all four systems are listed in Table 3-1.

Calculated conductance and thermopower values are given in Table 3-2. For comparison, the uncorrected DFT results are shown in brackets. While the DFT+Σ results are close to

experimental values, pure DFT overestimates both conductance and thermopower values quite substantially.

Table 3-1 Detailed overview of relevant energies within the DFT+Σ method in units of eV. -IP-ϵ_H and -EA-ϵ_L denote energy shifts related to the gas-phase molecule. Δ_{occ} and Δ_{virt} are the energy shifts of the occupied and unoccupied molecular orbitals due to image charges, when the molecules are close to metal electrodes in the molecular junctions. Σ_{occ} and Σ_{virt} are the total corrections to DFT level alignments.

Binding	Molecule	-IP-ϵ_H	-EA-ϵ_L	Δ_{OCC}	Δ_{virt}	Σ_{OCC}	Σ_{virt}
TT	*Para*	-1.49	1.53	0.53	-0.55	-0.95	0.98
	Meta	-1.48	1.54	0.53	-0.49	-0.95	1.05
HH	*Para*	-1.47	1.54	0.44	-0.44	-1.03	1.10
	Meta	-1.47	1.55	0.46	-0.47	-1.01	1.09

Table 3-2 Calculated conductance G and thermopower S_{junc}. Values listed have been obtained with the DFT+Σ method, those in brackets are uncorrected DFT results.

Binding	Molecule	G (G_0)	S_{junc} (μV/K)
TT	*Para*	2.35×10^{-3} (3.93×10^{-2})	19.2 (44.7)
	Meta	1.08×10^{-5} (4.76×10^{-4})	31.9 (92.1)
HH	*Para*	1.80×10^{-4} (4.20×10^{-3})	7.31 (41.9)
	Meta	3.85×10^{-6} (1.07×10^{-3})	21.4 (39.6)

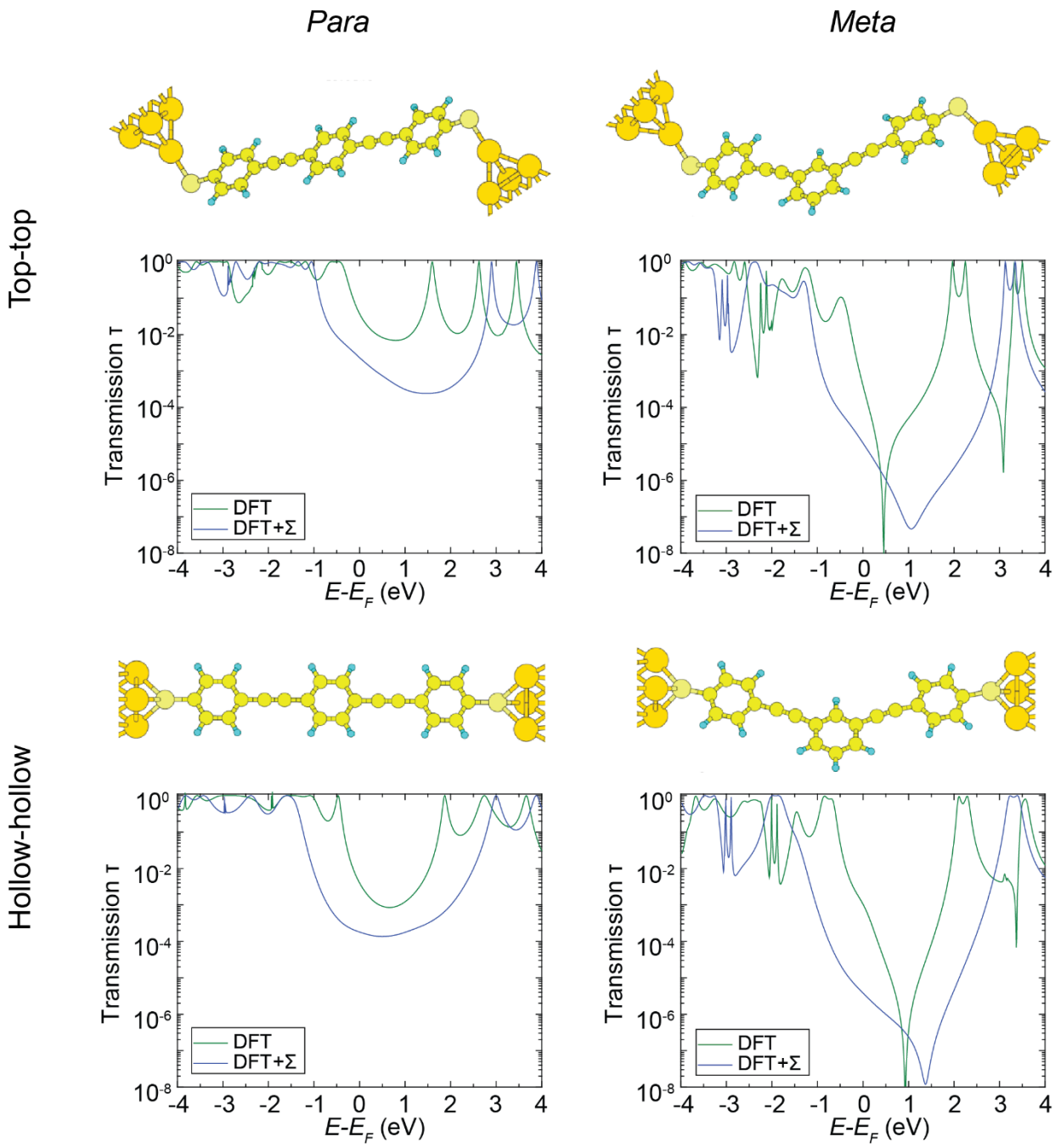

Figure 3-9 Junction geometries and corresponding calculated transmission curves. The qualitative shape of the transmission curves does not depend on the type of lead-molecule binding (top-top or hollow-hollow). Instead, it is determined by the molecular configuration (*para* or *meta*): An antiresonance between the frontier orbitals occurs only in the *meta* configuration (right side), while it is absent in the *para* configuration (left side).

3.4.3 Experimental Techniques

Preparation of STM tips with sub-50 nm radius.

To prepare sharp STM tips, the electrochemical etching method was used[10,11]. First we prepared a solution of 37% hydrochloric acid and absolute ethanol with a volume proportion of 1:1. The Au wire (Premion®, 99.999%, 0.5 mm diameter) to be etched, which acts as the anode, was placed at the center of an approximately 10 mm diameter cathode Au ring. Both the Au wire and Au ring were immersed just below the liquid surface. Then a ±7 V DC voltage was applied between the cathode and anode, and the wire is etched away at the meniscus of the solution until breaking. In this way a sharp tip is created.

Preparation of Au-coated AFM tips.

The conducting-probe AFM tip was fabricated by depositing an Au layer on commercially available AFM probes (NanoWorld Arrow^{TM}-CONTR) following a procedure similar to that used in previous work[12,13]. The silicon probe was first cleaned in a piranha solution for 2 min, thoroughly rinsed and dried, then alternating layers of Ti and Au (5 nm Ti, 50 nm Au, 5 nm Ti, 50 nm Au, 5 nm Ti and 50 nm Au) were sputtered onto the tip surface.

Preparation of Au template strip samples.

Similar to previous work[14,15], we first deposited 150 nm of Au on pristine Si wafers using electron beam evaporation. Then we used epoxy (Epotek® 377) drops to attach 7 mm × 7 mm square glass pieces (Pyrex® 7740) to the Au-coated silicon wafer. After curing the epoxy at 150 ^{o}C for 1 h, a glass piece was stripped off from the silicon wafer, peeling a clean ultra-flat Au film from the silicon wafer.

Self-assembly of monolayers.

To assemble molecules on the Au surface, the Au sample was immersed in a 100 μM molecule solution in ethanol (200 proof, Decan Labs) for more than 12 h. Following incubation, the device surface with the assembled monolayer was rinsed with ethanol and dried in a N_2 stream.

Monolayer characterization.

Monolayers were characterized using both ellipsometry and X-ray photoelectron spectroscopy (XPS) to determine the thickness and chemical composition. For ellipsometry (M-2000, J. A. Woolam Co., Inc), measurements were performed at three incidence angles (55^o, 65^o, 75^o) with wavelengths ranging from 600 nm to 1500 nm. For the XPS measurement (Kratos AXIS Ultra DLD X-ray photoelectron spectrometer), 8 mA and 14 kV were applied to a monochromatic Al X-ray source (see Fig. 3-10). The thicknesses were calculated assuming an exponential attenuation of substrate photoelectrons due to the presence of the aromatic monolayer. The thicknesses determined with the two methods (Table 3-3) correlate well with each other.

Table 3-3 Measured thickness of *para*-OPE3 and *meta*-OPE3 monolayers.

Molecule	Thickness (ellipsometry)	Thickness (XPS)
Para-OPE3	14.52 ± 0.088 Å	11.23 ± 0.66 Å
Meta-OPE3	12.28 ± 0.084 Å	11.01 ± 0.59 Å

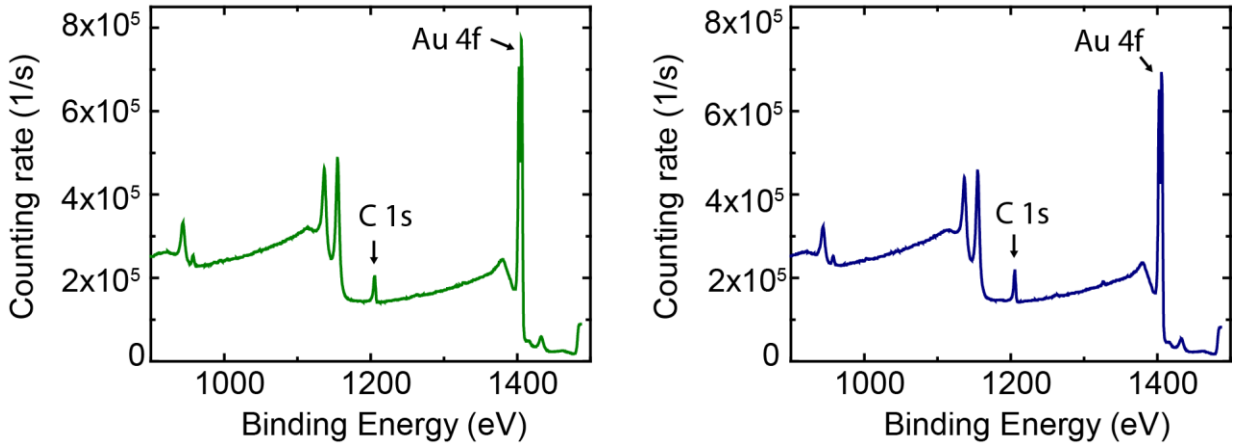

Figure 3-10 Wide-scan spectrum of Au samples coated with *para*-OPE3 (left) and *meta*-OPE3 (right) monolayers.

Method to measure single-molecule junctions.

To perform the thermoelectric measurements, a temperature difference was established between the Au tip and sample. After that, a small bias (V_{bias} =100 mV) was applied to the tip. The tip, controlled by a center piezoelectric tube, was withdrawn from the sample until a single-molecule junction was formed, as indicated by the appropriate conductance value. The movement of the tip during the withdraw cycle was then paused so that the electrical conductance shows a plateau with the corresponding conductance (as shown in Fig. 3-11). After the single-molecule junction was created, the bias voltage was alternated between 0 V and 100 mV, and the thermocurrent I_{th} was recorded when the bias was 0 V.

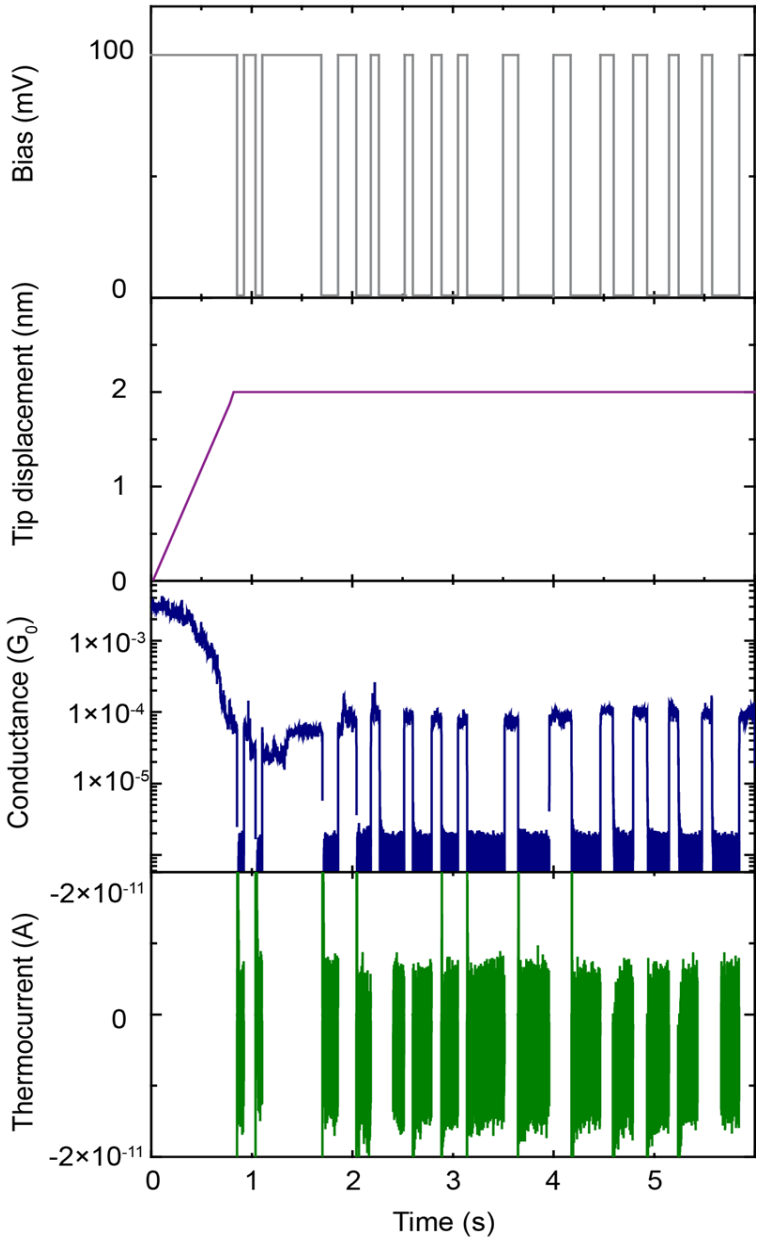

Figure 3-11 Representative data from thermoelectric measurements. From top to bottom: applied bias voltage, Au STM tip displacement, measured electrical conductance and measured thermocurrent of a single *para*-OPE3 junction as a function of time.

Data analysis method.

All experimental data (Figs. 3.2 and 3.3) were plotted in Origin. For the electrical conductance of Au-(*para*-OPE3)-Au junctions, we applied a Gaussian fit in the range of 0.3 $\times 10^{-4}$ - 2 $\times 10^{-4}$ G_0 to the conductance histogram (as shown in Fig. 3-2 a). For the electrical conductance of Au-(*meta*-OPE3)-Au junctions, we applied a Gaussian fit in the range of 0.8 $\times 10^{-5}$ - 1.4 $\times 10^{-5}$ G_0 to the conductance histogram (as shown in Fig. 3-2 b). The peak values corresponding to the Gaussian fit provided the most probable conductance whereas the width of the Gaussian provided the uncertainty in the estimated most probable conductance. For estimating the thermoelectric voltage in single-molecule junction experiments we applied Gaussian fits to the histograms (Fig. 3-2 c and 3-2 d) and used the peak value and Gaussian width as described above to obtain the most probable thermoelectric voltage and the uncertainty. The data obtained in this way are plotted in Fig. 3-2 e and 3-2 f. Finally, we applied a linear fitting with the York method to acquire the slope (ΔV_{th} / ΔT) and the standard error associated with the slope. A similar approach was used to process the data from monolayer experiments (Fig 3.3).

3.4.4 Control Experiments with Au-Benzenedithiol-Au Junctions

Following the same procedure as those employed for Au-(*para*-OPE3)-Au and Au-(*meta*-OPE3)-Au experiments, we used 1,4-benzeneditiol (Sigma-Aldrich, 99%) molecules to perform control experiments that illustrate the robustness of our measurements. The results are shown in Fig. 3-12. The Seebeck coefficient obtained is 11.0 ± 3.2 μ/K, which agrees well with previous experiments[16,17].

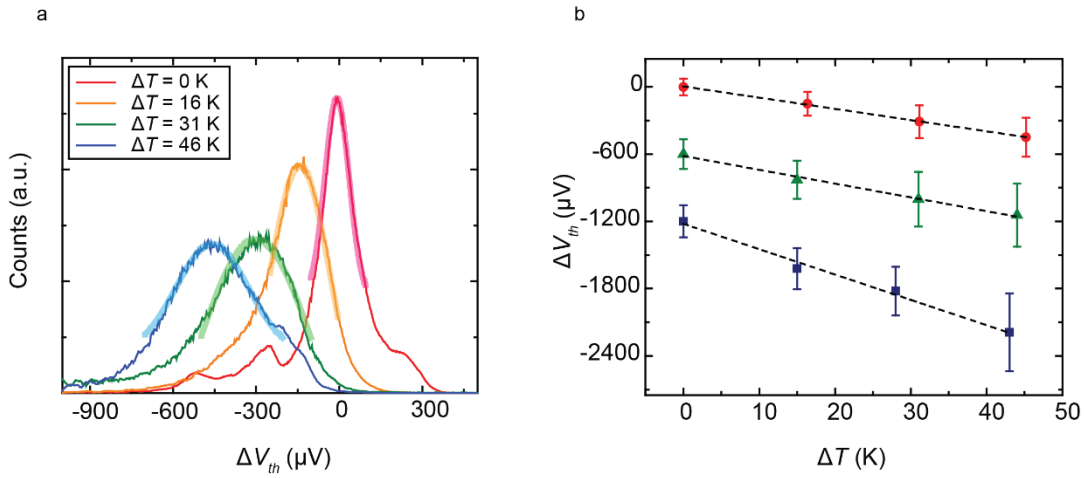

Figure 3-12 Control experiment using Au-benzenedithiol-Au junctions. a, Distribution of thermoelectric voltage at a series of ΔT. Shaded curves show Gaussian fits. b, Thermoelectric voltage for Au-benzenedithiol-Au (red circle), Au-(*para*-OPE3)-Au (green triangle) and Au-(*meta*-OPE3)-Au (blue square) junctions as a function of ΔT. Dashed lines are linear fits. Data are vertically shifted from zero thermoelectric voltage at $\Delta T = 0$ for better visualization.

3.4.5 Effect of Thermal Gradients on the Measured Thermopower

The thermopower (Seebeck coefficient) is defined by the following equation:

$$\Delta V_{th} = -S\Delta T \tag{3.4.3}$$

where $\Delta V_{th} = V_{hot} - V_{cold} = V_6 - V_5$, $\Delta T = T_{hot} - T_{cold} = T_1 - T_2$, T_n and V_n represent the temperature and electrical potential at node n (n=1-8), as denoted in Fig. 3-13.

The voltage differential between every two neighboring nodes in the STM setup is as follows:

$$V_2 - V_1 = -S_{junc}(T_2 - T_1) \tag{3.4.4}$$

$$V_3 - V_2 = -S_{Au}(T_3 - T_2) \tag{3.4.5}$$

$$V_4 - V_3 = -S_{Cu}(T_4 - T_3) \tag{3.4.6}$$

$$V_5 - V_4 = -S_{Cu}(T_5 - T_4) \tag{3.4.7}$$

$$V_7 - V_6 = -S_{Cu}(T_7 - T_6) \tag{3.4.8}$$

$$V_8 - V_7 = -S_{Cu}(T_8 - T_7) \tag{3.4.9}$$

$$V_1 - V_8 = -S_{Au}(T_1 - T_8) \tag{3.4.10}$$

Here S_{junc} is the thermopower of the molecular junction, S_{Au} and S_{Cu} are the thermopower of bulk Au and Cu, respectively. V_n and T_n are the voltage and temperature at each node (n=1-8). We assume that the Au sample and Au tip are both isothermal (T_3=T_2, T_8=T_1), and the Cu wires outside of the STM chamber are at ambient temperature (T_4=T_5=T_6=T_7). The thermal gradient arises between nodes 7 and 8, and nodes 3 and 4. Now we can reduce the equations to

$$\Delta V_{th} = V_6 - V_5 = S_{junc}(T_2 - T_1) - S_{Cu}(T_8 - T_3) = -\left(S_{junc} - S_{Cu}\right)\Delta T \tag{3.4.11}$$

where T_3=T_2 is the temperature of the hot side and T_8=T_1 is the temperature of the cold side. Finally, we obtain the expression of the thermopower of the junction:

$$S_{junc} = S_{Cu} - \frac{\Delta V_{th}}{\Delta T} \tag{3.4.12}$$

with S_{Cu} = 1.94 V/K at T= 300 K.

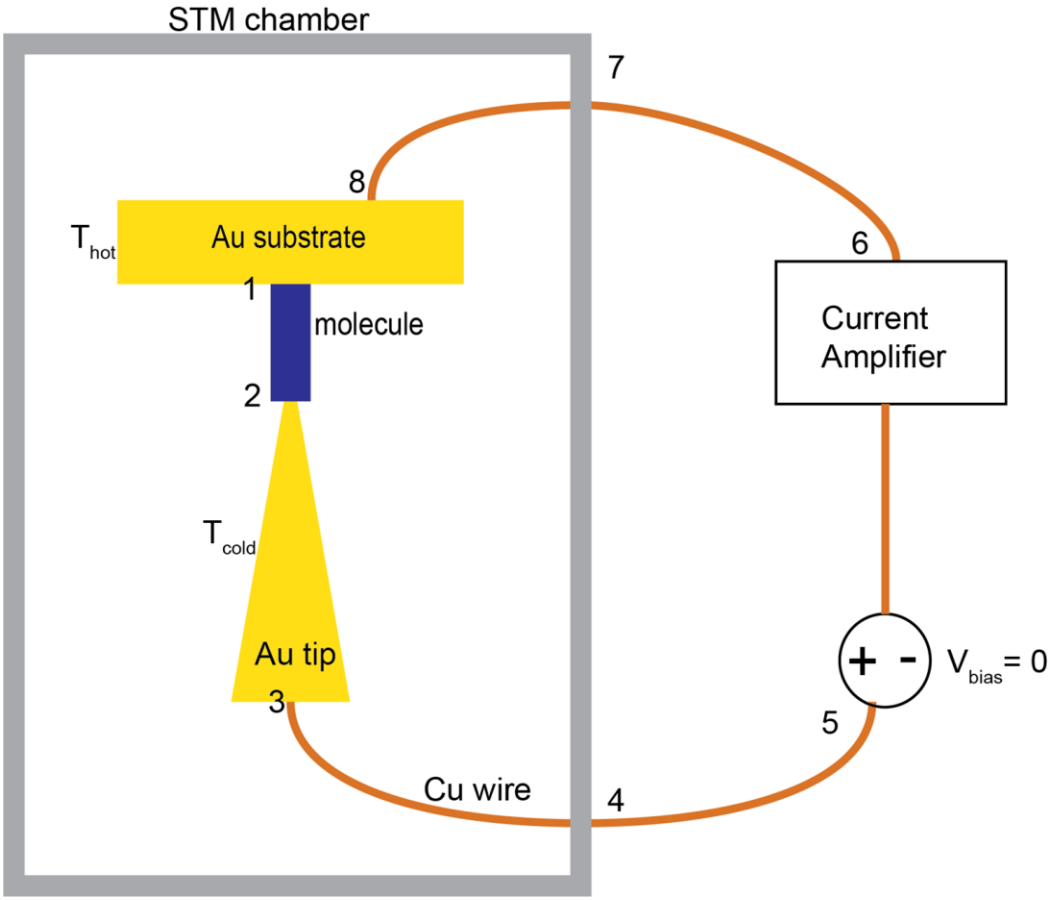

Figure 3-13 Schematic diagram of the circuit in the STM setup, showing different materials and nodes (1-8), where voltage and temperature differentials are present.

3.4.6 Discussion of the Sign of the Thermocurrent

As described in Chapter 3.3 and 3.4, $S_{junc} = S_{Cu} - \Delta V_{th}/\Delta T$, where the temperature differential is defined as $\Delta T = T_{substrate} - T_{tip}$ and the open circuit voltage differential is defined as $\Delta V_{th} = V_{substrate} - V_{tip}$. In Chapter 3.3 we related the thermocurrent I_{th} (measured under conditions, where the substrate and tip are shorted with each other externally) to the open circuit voltage ΔV_{th} by $\Delta V_{th} = -I_{th}/G$, where G is the electrical conductance of the junction. The negative sign reflects the fact that under open circuit conditions, the voltage

ΔV_{th}opposes the flow of I_{th}. Further, this choice of a negative sign is consistent with the fact that the Seebeck coefficient is positive for junctions exhibiting HOMO-dominated transport and negative for those with LUMO-dominated transport.

3.5 Conclusion

In conclusion both our single-molecule and ensemble measurements revealed a larger thermopower for the Au-(*meta*-OPE3)-Au junctions as compared to Au-(*para*-OPE3)-Au junctions. Our measurements are in good agreement with theoretical *ab-initio* calculations (see Fig. 3-4), which predict such a difference as a result of quantum interference effects. Our results demonstrate that it is possible to use quantum interference phenomena to achieve an enhanced thermoelectric performance in molecular junctions at room temperature, opening a path towards quantum engineering of thermoelectric materials. Besides the destructive π-interference discussed in our work, destructive σ-interference can also be utilized to elevate thermoelectric performance[142]. In contrast, similar enhancement effects in semiconductor systems, e.g. in quantum dots[143], require cryogenic temperatures and are therefore not suitable for many purposes. Future thermoelectric applications of molecule-based devices require a larger power factor, that is, a large S_{junc} combined with a large *G*. This desirable combination has been predicted for specific molecules with a quantum-tailored transmission spectrum such as zinc-porphines[18], which will be the subject of future work.

Chapter 4 Experimentally Investigating Electrical and Thermoelectric Properties in Single Metallo-Porphyrin Molecular Junctions

4.1 Abstract

Study of thermoelectric properties in molecular junctions provides important insights into charge transport mechanisms, which lays the foundation for energy conversion technologies at nano/micro scale. Molecular junctions with metallo-porphyrin molecules bridging Au electrodes have been shown to exhibit electrical conductance values that depend sensitively on the choice of the transition metal centres[144]. In this work we experimentally investigated the electrical conductance and thermoelectricity in several metalloporphyrin based molecular junctions. The experiments were conducted using scanning tunneling microscope break junction (STM-BJ) technique at room temperature. Our results show that when Zn metal center is present, the thermopower (11.5 μV/K) is increased by approximately a factor of two compared to bare Au-porphyrin-Au junctions (7.1 μV/K). And when Cu center is present, the thermopower is slightly suppressed (6.1 μV/K). With molecule backbones that directly bind to Au electrodes through C-Au bonds, our results also exhibit nearly two orders of magnitude increase in electrical conductance compared to previous results where thiol groups were used. Altogether, our results illustrate the possibility of tuning the thermoelectric properties in metalloporphyrin molecular junctions.

4.2 Introduction

Molecular junctions, created by bridging organic molecule between metal electrodes, are promising building blocks for electronic devices at nanometer scale.[7] Therefore, understanding charge transport properties in molecular junctions is of significant importance. Thermoelectric effect in molecular junctions, which directly converts temperature gradient to voltage, provide opportunities for fabricating energy conversion devices at the nanoscale. With a highly conjugated backbone, porphyrin molecules are good candidates for high efficiency energy conversion because of its ability to form metallo-porphyrins by coordinating a variety of metallic ions. Previous research has explored electrical transport in single porphyrin molecular junctions[144-146] featuring various transition metal centers residing in the core of the porphyrin framework and found that the electrical conductance can be tuned by transition metal centers. Recent theoretical work[145] has also predicted that the metal ion center can significantly affect the thermopower of metallo-porphyrin junctions, which make them attractive materials for fabrication of nano-scale devices. For example, Zn and Ni centered porphyrin junctions are expected to enhance the thermopower while Co and Cu centres are expected to reduce the thermopower down to nearly zero.

While computational work has predicted enhanced/reduced thermoelectricity in metallo-porphyrins, experimental investigation of the tunability of the thermoelectric properties in metallo-porphyrin molecular junctions via metal centers have remained unexplored. In this work we explore the electrical conductance and thermoelectricity properties of porphyrin and metallo-porphyrins featuring Cu and Zn metal centers.

4.3 Experiments and results

In our experiments we employed porphyrin and metallo-porphyrins with Cu and Zn metal centres. In an effort to improve the electrical conductance of molecular junctions simultaneously, we used molecules that form direct Si-Au covalent bond upon contact to Au electrodes. C-Au covalent bond has been applied in molecular junction and has been proven to increase the electrical conductance. For example, aromatic molecules terminated with trimethyltin end groups can cleave off and form a direct covalent bond between Au electrode and the molecule backbone and introduce two orders of magnitude increase in the electrical conductance, compared to junctions where molecules are bridged between Au electrodes via sulfur atoms. This method provides an opportunity to increase electrical conductance in molecular junctions, thus to increase the power factor (GS^2), where G is the electrical conductance, and S is Seebeck coefficient (also called thermopower).

Fig 4-1 a shows the structure of the molecules studied in this work, which are porphyrin, Cu-porphyrin, and Zn-porphyrin. Using tetrabutylammonium fluoride (TBAF) as deprotecting agent, the triisopropylsilyl end group was cleaved off, the molecules bind to the Au electrodes through direct C-Au bond (Fig. 4-2). Note the atom to form C-Au bond is an sp-hybridized carbon. Although previous work demonstrated lower electrical conductance with sp-hybridized carbon atoms than the one using sp^3 hybridization carbon atom[147-149], we expect increased conductance in these junctions compared to junctions with widely used sulfur anchor atom.

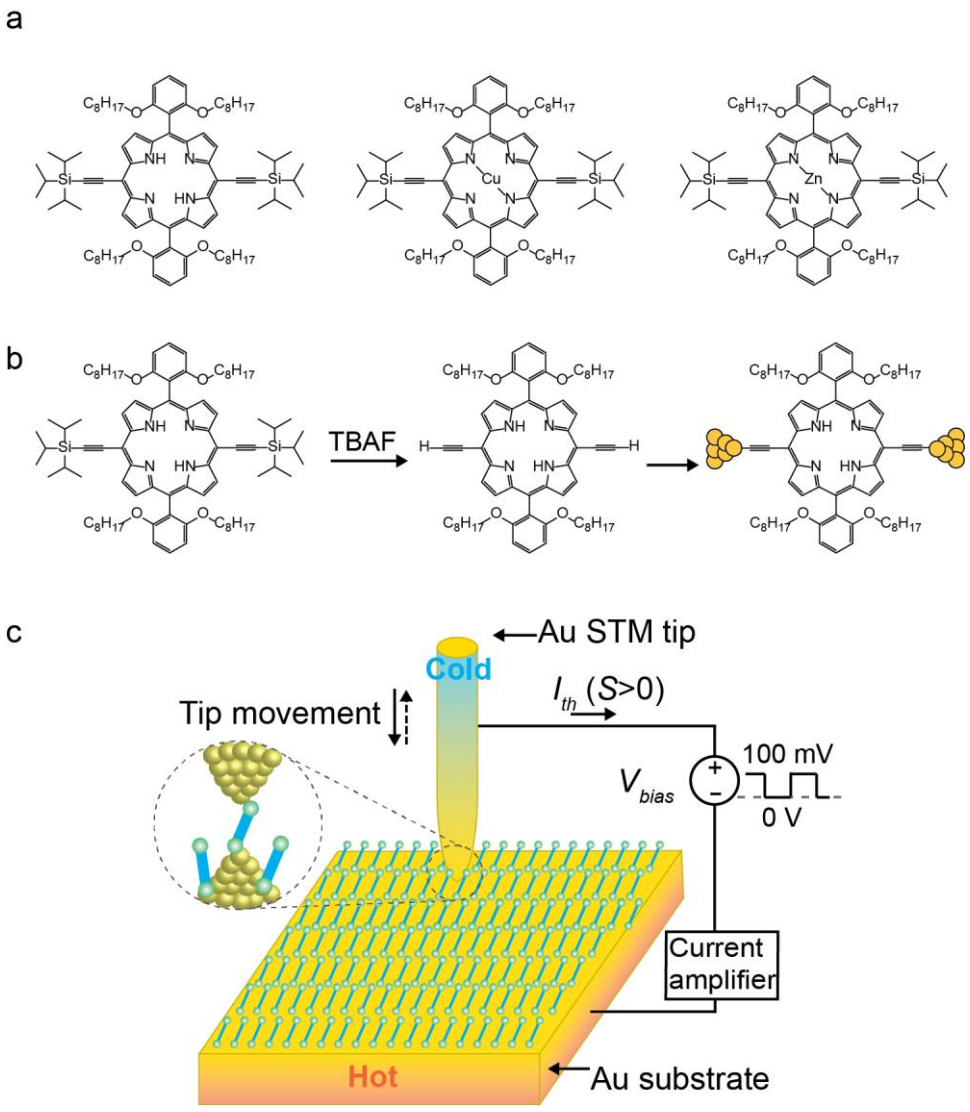

Figure 4-1 a, Structure of molecules studied in this work. From top to bottom: porphyrin, Cu-porphyrin and Zn-porphyrin. b, Formation of direct C-Au bond between porphyrin molecular backbone and Au electrodes. c, Schematic of electrical and thermoelectric measurements.

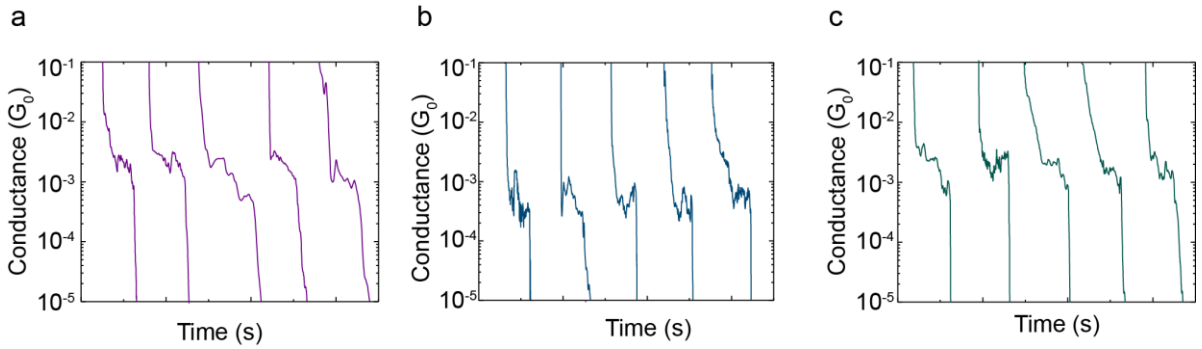

Figure 4-2 Representative traces of molecular junctions in electrical conductance measurements. a, Traces of Au-porphyrin-Au junctions. b, Traces of Au-(Cu-porphyrin)-Au junctions. c, Traces of Au-(Zn-porphyrin)-Au junctions.

First, to experimentally test the electrical conductance in these porphyrin-based molecular junctions, we conducted single molecular junction measurements in our customized ultrastable scanning tunneling microscope (STM) setup. As shown in Fig. 4-1 b, molecules were first self-assembled on Au template stripped samples with 150 nm Au on top. The 7×7 mm sized sample was mounted into the STM and connected to the electrical circuit via copper wires. The electrochemically etched Au STM tips with ~30 nm tip radius act as another electrode. In the measurement, the Au substrate was kept as ground and a 100 mV DC bias was applied from the Au tip. To form a single molecular junction, the tip first gradually approached the substrate coated with molecule monolayer until they contacted and an electrical conductance of more than 5 G_0 was observed. Then the Au tip was withdrawn from the Au substrate at a speed of 4 nm/s. During withdrawing, molecules were stochastically trapped between Au tip and substrate and the junction broke upon further stretching. The tunneling current was monitored during the procedure at 1 kHZ sampling rate, and steps and plateaus in the electrical conductance traces reflect the formation and breaking of molecular junctions.

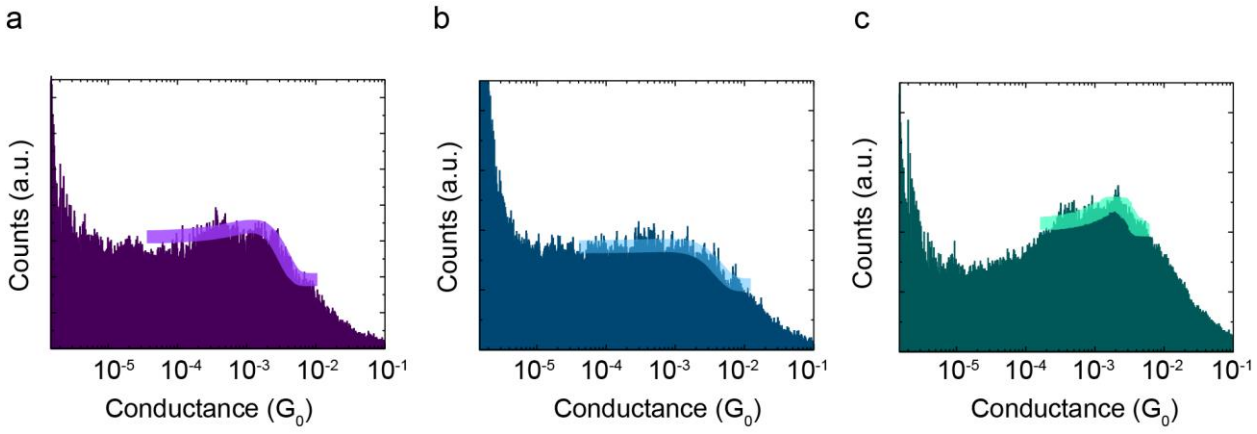

Figure 4-3 Conductance histogram obtained in the electrical conductance measurements of molecular junctions. a, Conductance histogram of Au-porphyrin-Au junctions. b, Conductance histogram of Au-(Cu-porphyrin)-Au junctions. c, Conductance histogram of Au-(Zn-porphyrin)-Au junctions. Light shaded lines represent Gaussian fit which reveals the peak in the histogram.

Representative conductance traces obtained from the measurement of porphyrin, Cu-porphyrin and Zn-porphyrin junctions are shown in Fig. 4-2, from left to right. To find out the most probable electrical conductance of each junctions, we built histogram with data collected from 1000 traces of each species of molecules without data selection. The peak of the histogram represents the most probable conductance, which is $(1.38 \pm 0.5) \times 10^{-3}\ G_0$ for Au-porphyrin-Au, $(6.9 \pm 1.5) \times 10^{-4}\ G_0$ for Au-(Cu-porphyrin)-Au, and $(2.0 \pm 0.4) \times 10^{-3}\ G_0$ for Au-(Zn-porphyrin)-Au (see Fig. 4-3, from left to right). These results show nearly 2 orders of magnitude increase in electrical conductance compared to those in previous reference[144] where thiol anchor group were used. Meanwhile, the trend of conductance change with varied metal center remains the same, *i.e.* $G_{\text{Au-(Zn-porphyrin)-Au}} > G_{\text{Au-porphyrin-Au}} > G_{\text{Au-(Cu-porphyrin)-Au}}$.

In order to measure the thermoelectricity in single molecular junctions, we first created stable temperature difference (ΔT) of 0, 15 K, 30 K, and 45 K between the Au tip and substrate. To create this temperature difference, the tip was maintained at room temperature (~ 300 K)

and the substrate was heated to desired temperature via integrated film heater. Both temperature of the tip and substrate were monitored through diode sensors. To measure the thermopower at a certain temperature difference ΔT, a single molecular junction was formed using the same method in the electrical conductance measurement. To stably trap a single molecule, the tip withdrawing speed was reduced to 0.1 nm/s, and the tip movement were paused when the electrical conductance met the most probable conductance value. At this point, the bias applied to the junction were switched from 100 mV to 0 V and the current in the circuit was recorded via a current amplifier. This current is the thermocurrent (I_{th}) resulted from the temperature difference ΔT. After 100 to 500 ms recording period, the bias was switched back to 100 mV to check if the electrical conductance was close to the most probable electrical conductance. This is to confirm that the junction was integral. This procedure of alternating the bias between 100 mV and 0 V was repeated until the single-molecular junction was broken, when the conductance value was not close to the most probable value. At this point the measurement was terminated and the data from last measurement were discarded. At each temperature difference ΔT, we conducted hundreds of similar measurements and collected the thermocurrent (I_{th}) which were later converted to thermovoltage ($\Delta V_{th} = I_{th} / G$) by dividing the electrical conductance of each junction. Histograms of thermovoltage at different temperature differences are shown in Fig.4-4 a-c. Note the sign of thremovoltage is considered as positive when current flows from the tip to the substrate through the junction, and negative when current flows in the opposite direction. From the histograms we acquired the most probable thermoelectric voltage at each temperature difference.

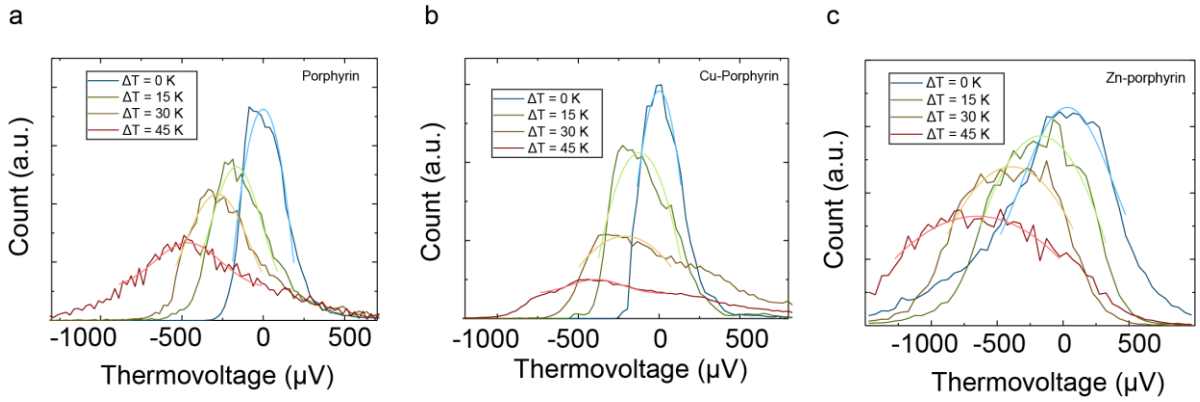

Figure 4-4 Histogram of thermovoltage in thermoelectric measurements under varied temperature difference (ΔT = 0 K, 15K, 30K, and 45 K a, Thermovoltage of Au-porphyrin-Au junctions. b, Thermovoltage of Au-(Cu-porphyrin)-Au junctions. c, Thermovoltage of Au-(Zn-porphyrin)-Au junctions. Blue lines: ΔT = 0 K; Green lines: ΔT = 15 K; Brown lines: ΔT = 30 K; Red lines: ΔT = 45 K. Light colored curves represent Gaussian fits.

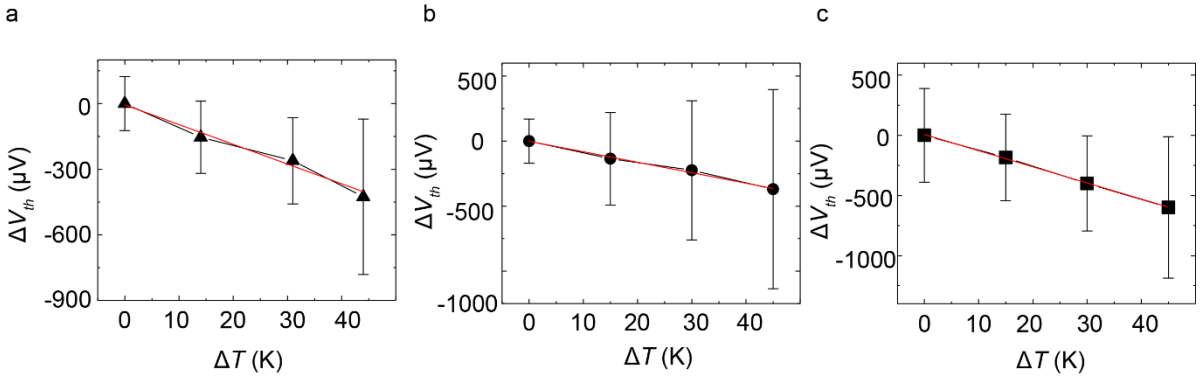

Figure 4-5 Plots of most probable thermoelectric voltages as a function of temperature difference for molecular junctions. a, Au-porphyrin-Au. b, Au-(Cu-porphyrin)-Au. c, Au-(Zn-porphyrin)-Au. Red lines represents linear fits.

Fig.4-5 plots the most probable thermoelectric voltages as a function of temperature difference for each junction studied. The thermopower of the molecular junction can be calculated by

$$S_{junc} = S_{Cu} - \frac{\Delta V_{th}}{\Delta T} \tag{4.3.1}$$

where S_{Cu}=1.94 μV/K represents the Seebeck coefficient (also called thermopower) of bulk copper at room temperature (300 K). Using Eq. 4.3.1 we obtained the Seebeck coefficients of each junction, which are (7.1 ± 6.1) μV/K for Au-porphyrin-Au, (6.1 ± 12.4) μV/K for Au-(Cu-porphyrin)-Au and (11.5 ± 13.8) μV/K for Au-(Zn-porphyrin)-Au, respectively. Compared to the Au-porphyrin-Au junction, the Au-(Zn-porphyrin)-Au junction shows nearly twice increase in thermopower and Au-(Cu-porphyrin)-Au shows slightly decreased thermopower. The trend of thermopower change agrees with prediction in literature[145].

4.4 Methods

4.4.1 Methods in Preparing Experiments

Preparation of STM tips with sub-50 nm radius.

To prepare sharp STM tips, the electrochemical etching method was used same as described in Chapter 3.4. First we prepared a solution of 37% hydrochloric acid and absolute ethanol with a volume proportion of 1:1. The Au wire (Premion®, 99.999%, 0.5 mm diameter) to be etched, which acts as the anode, was placed at the center of an approximately 10 mm diameter cathode Au ring. Both the Au wire and Au ring were immersed just below the liquid surface. Then a ±7 V DC voltage was applied between the cathode and anode, and the wire is etched away at the meniscus of the solution until breaking. In this way a sharp tip is created.

Preparation of Au template strip samples.

Similar to previous work described in Chapter 3.4, we first deposited 150 nm of Au on pristine Si wafers using electron beam evaporation. Then we used epoxy (Epotek® 377) drops to attach 7 mm × 7 mm square glass pieces (Pyrex® 7740) to the Au-coated silicon wafer. After curing the epoxy at 150 °C for 1 h, a glass piece was stripped off from the silicon wafer, peeling a clean ultra-flat Au film from the silicon wafer.

Formation of self-assembled monolayers.

To assemble molecules on the Au surface, the Au sample was immersed in a 100 μM molecule solution in ethanol (200 proof, Decan Labs) for more than 12 h. Following incubation, the device surface with the assembled monolayer was rinsed with ethanol and dried in a N_2 stream.

4.4.2. Methods in Single-Molecular Junction Measurements and Data Analysis

Single-molecular junction measurements.

To perform the thermoelectric measurements, first, a temperature difference was established between the Au tip and sample. After that, a small bias (V_{bias} =100 mV) was applied to the tip. The tip, controlled by a center piezoelectric tube, was withdrawn from the sample until a single-molecule junction was formed, as indicated by the appropriate conductance value. The movement of the tip during the withdraw cycle was then paused so that the electrical conductance shows a plateau with the corresponding conductance (as shown in Fig. 3-11 in Chapter 3). After the single-molecule junction was created, the bias voltage was alternated between 0 V and 100 mV, and the thermocurrent I_{th} was recorded when the bias was 0 V.

Data analysis method.

All experimental data were plotted in Origin. For the electrical conductance of Au-porphyrin-Au junctions, we applied a Gaussian fit in the range of 5×10^{-5} - 1×10^{-2} G_0 to the conductance histogram (as shown in Fig. 4-3 a). For the electrical conductance of Au-(Cu-porphyrin)-Au junctions, we applied a Gaussian fit in the range of 5×10^{-5} - 1×10^{-2} G_0 to the conductance histogram (as shown in Fig. 4-3 b). For the electrical conductance of Au-(Zn-porphyrin)-Au junctions, we applied a Gaussian fit in the range of 1×10^{-4} - 1×10^{-2} G_0 to the conductance histogram (as shown in Fig. 4-3 c). The peak values corresponding to the Gaussian fit provided the most probable conductance whereas the width of the Gaussian provided the uncertainty in the estimated most probable conductance. For estimating the thermoelectric voltage in single-molecule junction experiments we applied Gaussian fits to the histograms (Fig. 4-4 a-c) and used the peak value and Gaussian width as described above to obtain the most probable thermoelectric voltage and the uncertainty. The data obtained in this way are plotted in Fig. 4-5 a-c. Finally, we applied a linear fitting with the York method to acquire the slope (ΔV_{th} / ΔT) and the standard error associated with the slope.

4.4.3 Effect of Thermal Gradients on the Measured Thermopower

The thermopower (Seebeck coefficient) is defined by the following equation:

$$\Delta V_{th} = -S\Delta T \tag{4.4.1}$$

where $\Delta V_{th} = V_{hot} - V_{cold} = V_6 - V_5$, $\Delta T = T_{hot} - T_{cold} = T_1 - T_2$, Tn and Vn represent the temperature and electrical potential at node n (n=1-8), as denoted in Fig. 4-6.

The voltage differential between every two neighboring nodes in the STM setup is as follows:

$$V_2 - V_1 = -S_{junc}(T_2 - T_1) \tag{4.4.2}$$

$$V_3 - V_2 = -S_{Au}(T_3 - T_2) \tag{4.4.3}$$

$$V_4 - V_3 = -S_{Cu}(T_4 - T_3) \tag{4.4.4}$$

$$V_5 - V_4 = -S_{Cu}(T_5 - T_4) \tag{4.4.5}$$

$$V_7 - V_6 = -S_{Cu}(T_7 - T_6) \tag{4.4.6}$$

$$V_8 - V_7 = -S_{Cu}(T_8 - T_7) \tag{4.4.7}$$

$$V_1 - V_8 = -S_{Au}(T_1 - T_8) \tag{4.4.8}$$

Here S_{junc} is the thermopower of the molecular junction, S_{Au} and S_{Cu} are the thermopower of bulk Au and Cu, respectively. V_n and T_n are the voltage and temperature at each node (n=1-8). We assume that the Au sample and Au tip are both isothermal (T_3=T_2, T_8=T_1), and the Cu wires outside of the STM chamber are at ambient temperature (T_4=T_5=T_6=T_7). The thermal gradient arises between nodes 7 and 8, and nodes 3 and 4. Now we can reduce the equations to

$$\Delta V_{th} = V_6 - V_5 = S_{junc}(T_2 - T_1) - S_{Cu}(T_8 - T_3) = -\left(S_{junc} - S_{Cu}\right)\Delta T \tag{4.4.9}$$

where T_3=T_2 is the temperature of the hot side and T_8=T_1 is the temperature of the cold side.

Finally, we obtain the expression of the thermopower of the junction:

$$S_{junc} = S_{Cu} - \frac{\Delta V_{th}}{\Delta T} \tag{4.4.10}$$

with S_{Cu} = 1.94 V/K at T = 300 K.

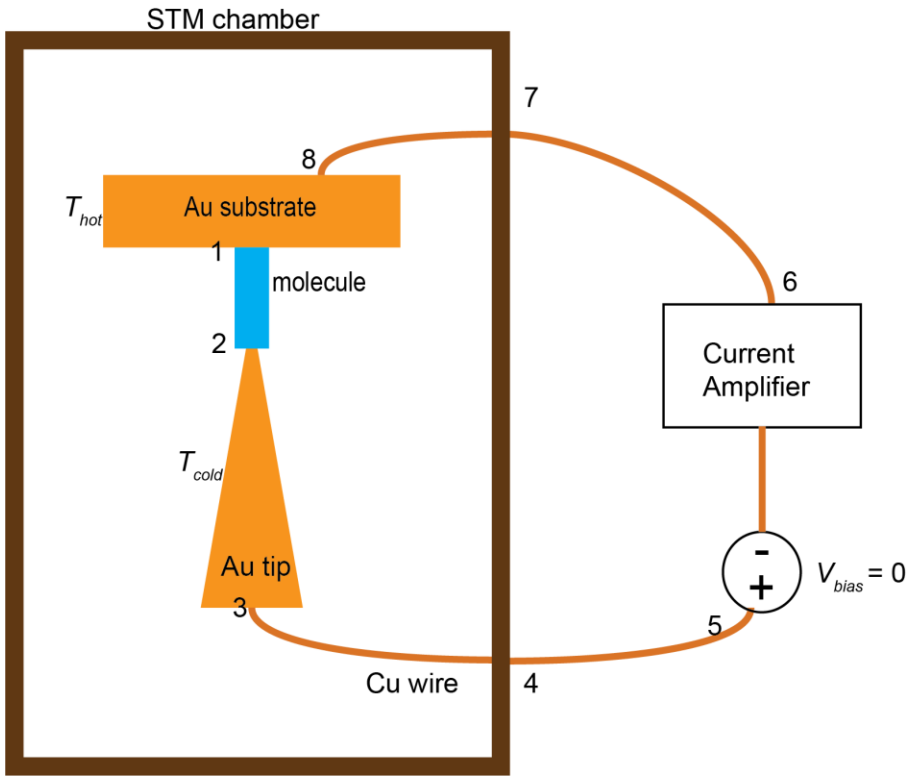

Figure 4-6 Schematic diagram of the circuit in the STM setup, showing different materials and nodes (1-8), where voltage and temperature differentials are present.

4.4.4 Discussion of the Sign of the Thermocurrent

As described in Chapter 4.3, $S_{junc} = S_{Cu} - \Delta V_{th}/\Delta T$, where the temperature differential

is defined as $\Delta T = T_{substrate} - T_{tip}$ and the open circuit voltage differential is defined as $\Delta V_{th} = V_{substrate} - V_{tip}$. In the Chapter 4.3 we related the thermocurrent I_{th} (measured under conditions where the substrate and tip are shorted with each other externally) to the open circuit voltage ΔV_{th} by $\Delta V_{th} = -I_{th}/G$, where G is the electrical conductance of the junction. The negative sign reflects the fact that under open circuit conditions, the voltage ΔV_{th}opposes the flow of I_{th}. Further, this choice of a negative sign is consistent with the fact that the Seebeck coefficient is positive for junctions exhibiting HOMO-dominated transport and negative for those with LUMO-dominated transport.

4.5 Conclusion

In this work we used STM break junction (STM) technique to investigate electrical and thermoelectrical properties of single-molecular junctions based on porphyrin and metallo-porphyrin with chosen metal centres Cu and Zn. To improve the electrical conductance, we created direct Si-Au covalent bond between molecule backbone to Au electrodes, and results show two orders of magnitude increase compared to previous results where molecule were bridged between Au electrodes by sulfur atoms. This is probably due to the enhanced electronic coupling of the electrodes to the complex conjugated system of porphyrin, in spite that coupling of the conducting orbitals with the Au electrodes introduced by sp-hybridized carbon atom may be quite different with that of sp^3 hybridized carbon atom.

To explore how thermoelectric properties of Au-porphyrin-Au junctions may vary with different metal ion centers, we conducted single-molecular junction experiments under temperature difference from 0 K to 45 K in ambient condition. Our results show that the all

junctions (Au-porphyrin-Au, Au-(Cu-porphyrin)-Au and Au-(Zn-porphyrin)-Au) present positive Seebeck coefficient, which implies HOMO (highest occupied molecular orbital) dominated charge transport in all three molecular junctions. Furthermore, our results show the possibility to tune the thermopower in metallo-porphyrin molecular junctions by varying the transition metal center. Interestingly, among all the measured junctions, Au-(Zn-porphyrin)-Au junction exhibits highest electrical conductance as well as highest Seebeck coefficient, which makes Au-(Zn-porphyrin)-Au attractive material for energy conversion device. The power factor (GS^2) of Au-(Zn-porphyrin)-Au achieves 2×10^{-15} W/K^2 which exceeds that of Au-benzenedithiol-Au (3.8×10^{-17} W/K^2).

Chapter 5 Peltier Cooling in Molecular Junctions

Reproduced with permission from *Nature Nanotechnology*.

Longji Cui, Ruijiao Miao, Kun Wang, Dakotah Thompson, Linda Angela Zotti, Juan Carlos Cuevas, Edgar Meyhofer and Pramod Reddy. *Nature Nanotechnology*, **13**, 122-127, (2018).

5.1 Abstract

The study of thermoelectricity in molecular junctions is of fundamental interest for the development of various technologies including cooling (refrigeration) and heat-to-electricity conversion[8, 37, 38, 60]. Recent experimental progress in probing the thermopower (Seebeck effect) of molecular junctions[22, 27, 78, 81] has enabled studies of the relationship between thermoelectricity and molecular structure[2, 7]. However, observations of Peltier cooling in molecular junctions—a critical step for establishing molecular-based refrigeration—have remained inaccessible. Here, we report direct experimental observations of Peltier cooling in molecular junctions. By integrating conducting-probe atomic force microscopy[17, 18] with custom-fabricated picowatt-resolution calorimetric microdevices, we created an experimental platform that enables the unified characterization of electrical, thermoelectric and energy dissipation characteristics of molecular junctions. Using this platform, we studied gold junctions with prototypical molecules (Au-biphenyl-4,4'-dithiol-Au, Au-terphenyl-4,4''-dithiol-Au and Au-4,4'-bipyridine-Au) and revealed the relationship between heating or

cooling and charge transmission characteristics. Our experimental conclusions are supported by self-energy-corrected density functional theory calculations. We expect these advances to stimulate studies of both thermal and thermoelectric transport in molecular junctions where the possibility of extraordinarily efficient energy conversion has been theoretically predicted[37, 38, 60, 150].

5.2 Introduction

When electrical current flows across an isothermal junction of two materials, net refrigeration is accomplished when Peltier cooling is larger in magnitude than Joule heating[151, 152]. Experimentally probing Peltier cooling and Joule heating in current-carrying molecular junctions is crucial for understanding electron transport, electron–phonon interactions and energy dissipation mechanisms at the atomic and molecular scales. Previous experimental studies[153-155] have explored local ionic and electronic heating in molecular junctions and probed the non-equilibrium temperature increase due to electron–phonon and electron–electron interactions in the junctions. More recently, experimental advancements have enabled the measurement of Joule heating in the electrodes of molecular junctions[55, 120]. In spite of interesting theoretical predictions and the practical significance[156], experimental observations of molecular-scale refrigeration have not been possible because of technical challenges in detecting picowatt-level cooling.

5.3 Experiments, Results and Discussion

We developed an experimental platform that is suitable for creating and stably maintaining molecular junctions while allowing simultaneous measurements of the electrical conductance and Seebeck coefficient, as well as the heating or cooling power deposited in the electrodes

of the molecular junctions. Specifically, we developed custom-fabricated calorimetric microdevices (Fig. 5-1 a, b), which have integrated into them highly sensitive platinum thermometers with a temperature resolution (ΔT_{min}) of < 0.1 mK (see Fig. 5-5 and Chapter 5.4.11). The microdevice is suspended by four long, doubly clamped silicon nitride beams to achieve both high thermal resistance ($R_S \approx 3.3 \times 10^6$ KW^{-1}; see Fig. 5-6) and stiffness (~3.8 Nm^{-1}; see Fig. 5-9). These characteristics enable detection of heating or cooling power with ~30 pW resolution. Moreover, the planar surface of the microdevice (see Fig. 5-7) is coated with an electrically isolated Au layer, on top of which a self-assembled monolayer is created to aid the formation of molecular junctions (see Fig. 5-1 a and Chapter 5.4).

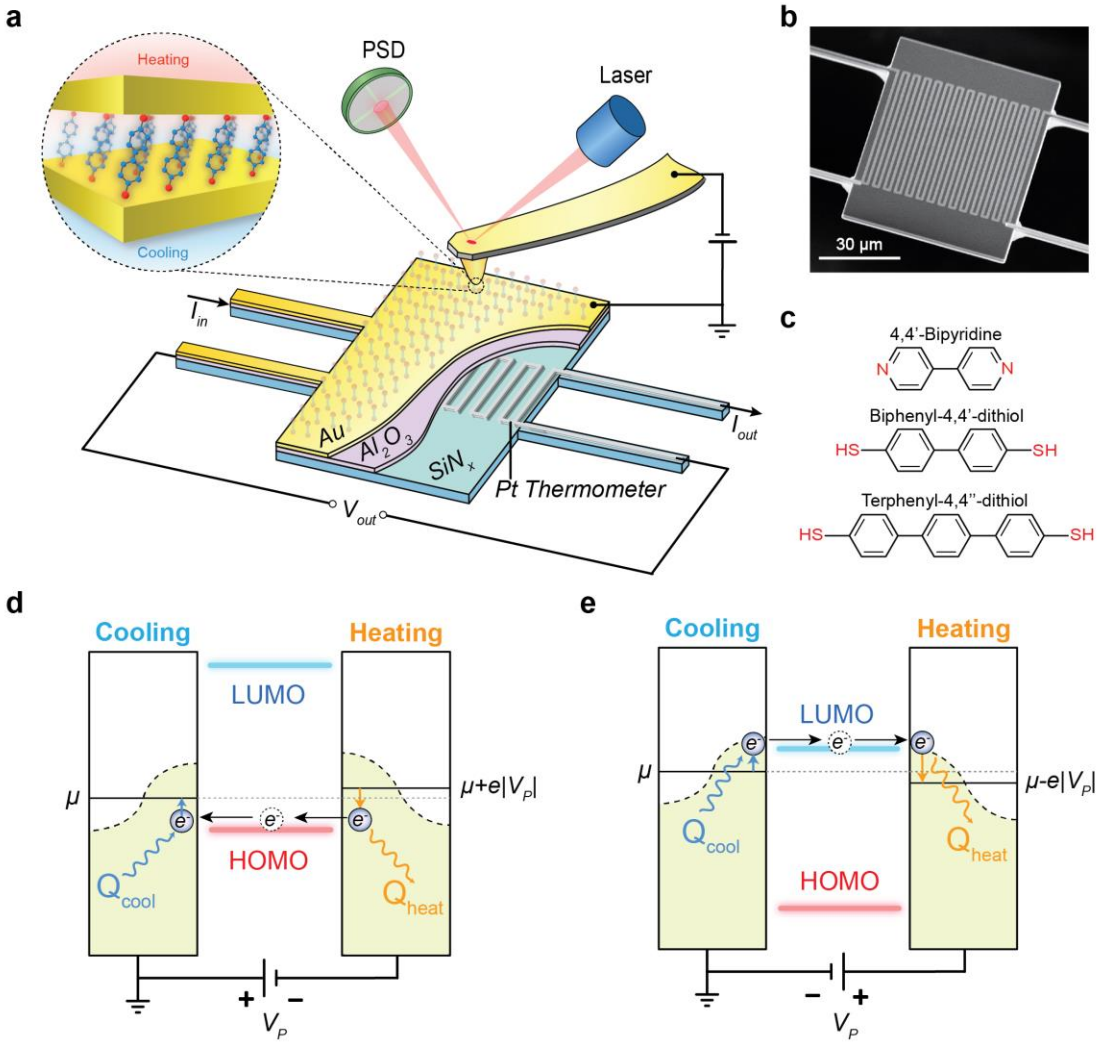

Figure 5-1 Probing cooling in molecular junctions. a, Schematic of the experimental platform. Molecular junctions are formed by placing a Au-coated AFM tip in gentle contact with a self-assembled monolayer created on a Au-coated calorimetric microdevice. The electrical conductance of the molecular junctions is measured by supplying a small voltage bias (V_P) and recording the resultant current. The temperature change of the microdevice is induced by the heating or cooling effect in the current-carrying molecular junctions. The resistance of the Pt thermometer is continuously monitored by applying an electric current (I_{in}) into the resistor and measuring the voltage output (V_{cal}). PSD, position-sensitive detector. b, Scanning electron microscope image of the custom fabricated microdevice. c, Chemical structures of the molecules studied in this experiment. d, Schematic description of the origin of the Peltier effect in a molecular junction in which transport is dominated by the HOMO. The transmission function is depicted as a Lorentzian around the HOMO and LUMO levels. The terms μ_{cal}, Q_{heat} and Q_{cool} denote chemical potential, heating and cooling power, respectively. e, Same as d, but for the LUMO-dominated case.

Our strategy for quantifying the Peltier-effect-based cooling of molecular junctions, at room temperature (298 K), is depicted in Fig. 5-1 a. A contact-mode atomic force microscope (AFM), equipped with a sharp Au-coated cantilevered probe (tip radius ~100 nm and stiffness ~0.1 Nm^{-1}; see Fig. 5-8), is used to make a 'soft' contact with the monolayer of molecules on the Au-coated microdevice such that the contact force is maintained at ~1 nN by using feedback control. As established in past work[17, 18, 157, 158], this nanoscopic contact between an AFM tip and a self-assembled monolayer contains approximately 100 metal–molecule–metal junctions (see Chapter 5.4.8). Next, we applied a voltage bias (V_P) and recorded the resultant electric current (I) flowing through the molecules from which we obtained the electrical conductance (and the I–V characteristics) of the molecular junctions. Current flow across the molecular junctions results in heat dissipation and cooling due to Joule heating and Peltier effects, which in turn give rise to a temperature change (ΔT) of the calorimetric microdevice that can be quantified by measuring the resistance of the Pt thermometer integrated into the device. To monitor the temperature change, we supplied a fixed electric current ($I_{in} = 20\ \mu A$) to the Pt thermometer while continuously monitoring the voltage drop (V_{cal}) across the resistor. The total cooling or heating power (Q_{cal}) in the calorimeter can be directly determined from ΔT by $Q_{cal} = \Delta T / R_S$, where $R_S \approx 3.3 \times 10^6\ KW^{-1}$ is the thermal resistance of the microdevice (see Fig. 5-6).

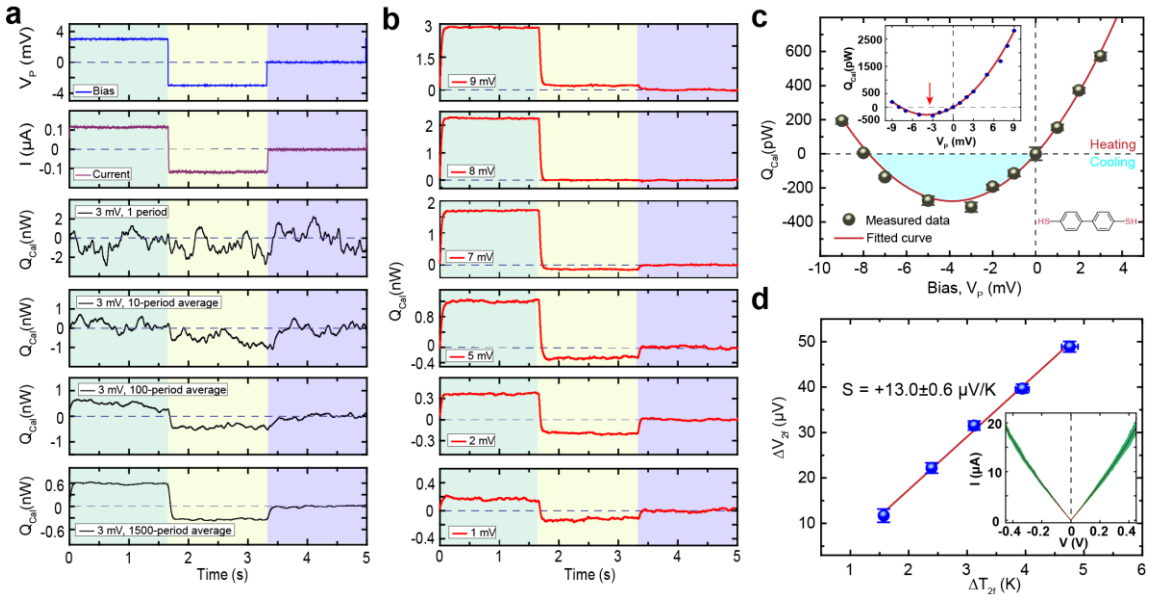

Figure 5-2 Observation of Peltier cooling in Au-BPDT-Au junctions. a, Experimental protocol for quantifying the heating and cooling power in molecular junctions. A periodic three-level voltage (blue line) is supplied into the junctions, while electrical current (purple line) and thermal signal (black lines) are simultaneously recorded. Improved thermal resolution is obtained by averaging the thermal signal over a large number of periods to reduce noise level. b, Time-averaged heating and cooling signal traces (red lines) under different voltage bias. c, Measured voltage-dependent thermal power for BPDT junctions. The solid red line indicates the fitted curve using equation (5.3.1) and the measured Seebeck coefficient and electrical conductance. The shaded blue region indicates the voltage region where net cooling (refrigeration) is observed. Inset shows the measured data and the fitted curve for voltage bias from -9 mV to +9 mV. The red arrow points to the voltage that leads to the maximum cooling effect. Error bars represent the standard deviation of data obtained from the time-averaging scheme. d, Measured Seebeck coefficient (*S*) of BPDT junctions. The red solid line is the best linear fit to the measured data, with the slope indicating the Seebeck coefficient. Inset shows the *I*-*V* characteristics of the junctions obtained by averaging ten individual *I*-*V* curves. The green shaded region represents the standard deviation. Error bars represent the standard deviation of data obtained from five independent measurements.

One may ask whether it is reasonable to expect cooling in the electrodes of molecular junctions and under which conditions. Within Landauer theory, when a voltage bias V_P is applied to the probe relative to the grounded calorimeter electrode, the power input into the calorimeter (Q_{cal}) is[158]

$$Q_{cal}(V_P) = \frac{2}{h}\int_{-\infty}^{\infty}(\mu_{cal} - E)\tau(E - V_P)[f_{cal} - f_P]dE$$

$$= GTSV_P + \frac{1}{2}GV_P^2 + O(V_P^3) \quad (5.3.1)$$

where μ_{cal} is the chemical potential of the calorimeter electrode, f_P and f_{cal} are the Fermi–Dirac distributions of the probe and calorimeter electrodes, respectively, $\tau(E, V_P)$, is the transmission of the junction depended on energy (E) and bias voltage (V_P), T is absolute temperature, G and S are the low-bias electrical conductance and the Seebeck coefficient of the molecular junctions, respectively, and $O(V_P^3)$ represents the higher-order terms. Note that G and S are related to $\tau(E, V_P)$ (see Chapter 5.4). Thus, for small biases, when $|V_P| < 2|ST|$ and the first-order term $GTSV_P$ dominates, cooling is expected when SV_P (the product of the Seebeck coefficient and the applied bias) is negative. The physical picture behind the expected cooling mechanism is shown in the schematics in Fig. 5-1 d, e and is discussed below.

We first investigated cooling in Au-biphenyl-4,4'-dithiol (BPDT)-Au junctions. Towards this goal, we applied a periodic, three-level voltage sequence, $+V_P$ (from $t = 0$ to 1.66 s), $-V_P$ (1.66 s to 3.33 s) and 0 volts (3.33 s to 5 s), across Au-BPDT-Au junctions, and simultaneously measured both the current flow through the junctions and Q_{cal} (note that the calorimeter electrode is always grounded in these experiments). The time period of each of the voltage pulses (1.66 s) is chosen to be significantly larger than the thermal time constant (~40 ms) of the microdevice (see Chapter Fig. 5-7) so that there is sufficient time for steady-state conditions to be established in the calorimeter. Representative traces of the recorded electrical current (I) and heating or cooling power (Q_{cal}), corresponding to one period of the three-level voltage sequence ($+V_P$, $-V_P$ and 0, where V_P was chosen to be 3 mV), are shown in Fig. 5-2 a.

It can be clearly seen that when the voltage is changed from $+V_P$ to $-V_P$, the current direction switches sign as expected. However, the expected heating or cooling of the calorimeter (represented by a temperature change of the calorimeter) remains unresolvable owing to the considerable noise in the signal. To resolve the desired signal, we used an averaging scheme that improves the thermal resolution and hence the calorimetric resolution (see Method 5.4.11 for details). Briefly, in this approach the thermal signals from many (500 to 2000) equivalent phases of three-level voltage sequence ($+V_P$, $-V_P$ and 0) are aligned and averaged, and Q_{cal} is determined. Figure 5.2 a depicts the results obtained after averaging 10100 and 1500 period traces, clearly demonstrating that such averaging reduces noise to a level where heating and cooling can be resolved. Specifically, for Au-BPDT-Au junctions we find a net cooling power ~300 pW when a negative bias of -3 mV is applied. The corresponding heating power when reversing the bias polarity is ~600 pW.

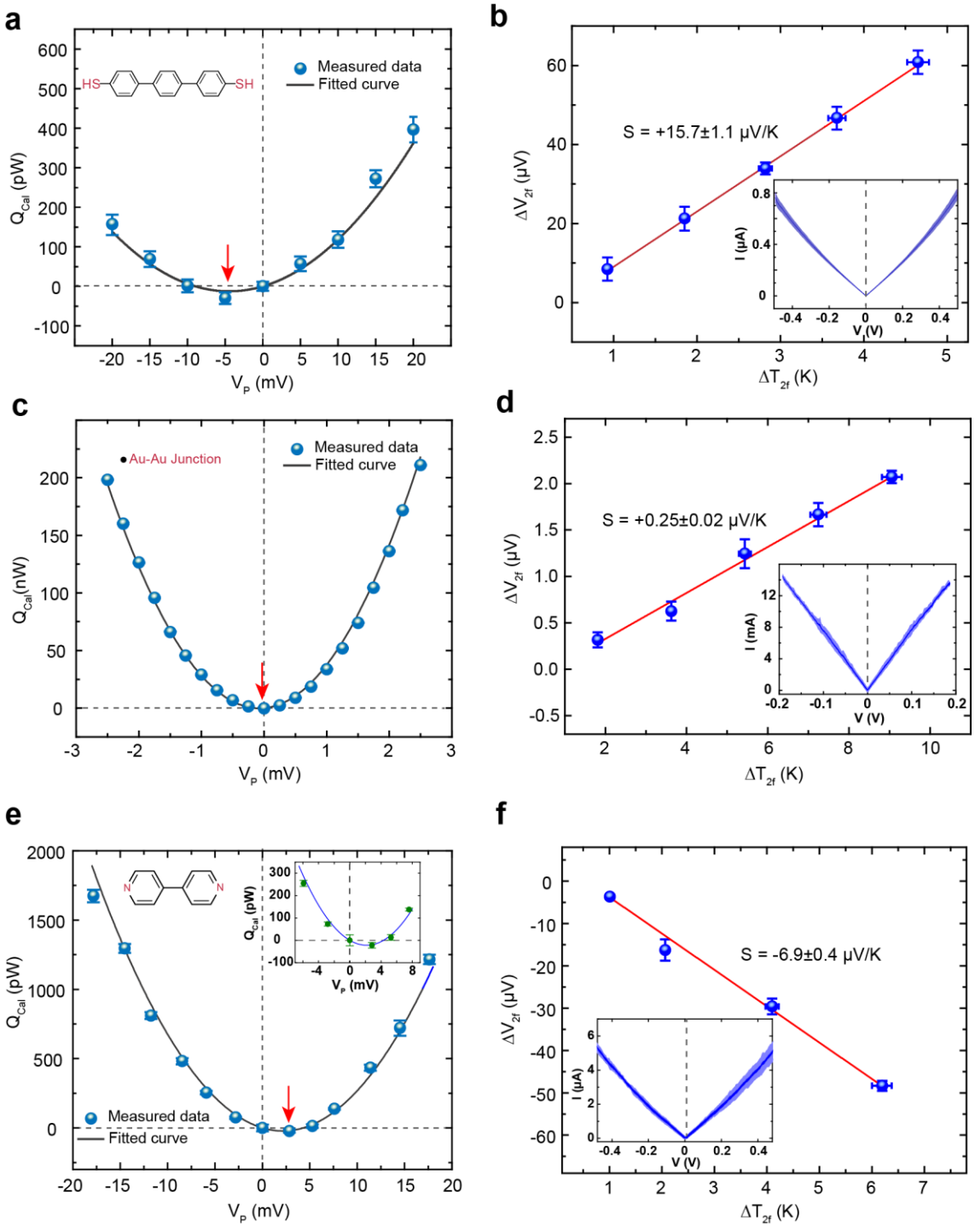

Figure 5-3 Measured Peltier effect in Au-TPDT-Au, Au-Au and Au-BP-Au junctions. a, b, As in Fig. 5-2 c and d, but for TPDT junction. The black solid line indicates the fitted curve using transport parameters (low-bias conductance and Seebeck coefficient) input from independent characterizations of both properties. c, d, For Au-Au noncontacts in which negligible cooling effect is found. e, f, For BP junction. In contrast to BPDT and TPDT

junctions, the maximum in cooling power is observed when a positive bias is applied, consistent with the physical picture of the Peltier effect in LUMO-dominated molecular junctions (indicated by negative Seebeck coefficient in f). Error bars in a, c, e represent the standard deviation of data obtained from the time-averaging scheme. Error bars in b, d, f represent the standard deviation of data obtained from five independent measurements.

Figure 5.2 b presents the time-averaged thermal signal for varying V_P from 1 mV and 9 mV for the same Au-BPDT-Au molecular junctions. It can be seen that, under positive biases, Q_{cal} is always positive. In contrast, net cooling ($Q_{cal} < 0$) is observed in a narrow range of negative biases, $V_P \in [-8\text{ mV}, 0\text{ mV}]$. We plot the measured Q_{cal} as a function of the voltage bias applied to the probe (V_P) in Fig. 5-2 c. The measured power dissipation is roughly parabolic as expected from equation (5.3.1). To obtain a quantitative comparison with the predictions of equation (5.3.1), we independently measured the electrical conductance and the Seebeck coefficient of molecular junctions. These measurements are accomplished with the same experimental platform (see Chapter 5.4) by directly recording the *I-V* characteristics and *S*. From these measurements (Fig. 5-2 d), we determined that the low-bias conductance is ~37 μS (note that this relatively large conductance is due to the fact that we trapped multiple molecules in the molecular junction) and the Seebeck coefficient is $+13.0 \pm 0.6\ \mu VK^{-1}$ (indicating that transport is dominated by the highest occupied molecular orbital, HOMO), in good agreement with past work12 for Au-BPDT-Au molecular junctions. By putting these independently measured transport parameters into equation (5.3.1) (neglecting higher-order $O(V_P^3)$ terms), we obtained the solid line shown in Fig. 5-2 c. The resulting agreement between the calculated thermoelectric cooling of Au-BPDT-Au junctions and the experimental values confirms the applicability of the Landauer approach for modelling cooling.

The physical processes that result in molecular-junction-based cooling can be understood by considering the schematic of a HOMO junction shown in Fig. 5-1 d. The left electrode is grounded and represents the electrode integrated into the calorimeter while the right electrode signifies the probe. When the probe is negatively biased as shown, electrons are injected into the probe electrode at an energy of $\mu_{cal} + e|V_P|$ and leave the calorimeter electrode at an energy μ_{cal}. Under these conditions, charge transfer occurs not only at energies between $\mu_{cal} + e|V_P|$ and μ_{cal} but also at energies within a few k_BT (k_B is the Boltzmann constant) of the chemical potentials owing to the thermal broadening of the Fermi–Dirac functions. Charge transfer at energies between the chemical potentials leads to Joule heating in the calorimeter (see Fig. 5-14). However, charge transfer through the junction at energies below the chemical potential of the calorimeter electrode leads to cooling in the calorimeter, while charge transfer at energies above the chemical potential of the probe leads to heating. Thus, in HOMO-dominated junctions, when the probe is negatively biased and the voltage magnitude is appropriately chosen, net cooling (that is, Peltier cooling dominates over Joule heating) occurs in the calorimeter, as the transmission probabilities (see Fig. 5-1 d) are larger at μ_{cal} than at $\mu_{cal} + e|V_P|$ (see Chapter 5.4.12 for more details of the physical mechanism). The situation is reversed when the probe is positively biased, resulting in only net heating in the calorimeter for HOMO-dominated junctions. Similar arguments can be presented to understand cooling in LUMO-dominated junctions (Fig. 5-1 e).

Corresponding measurements were also performed on Au–terphenyl-4,4″-dithiol (TPDT)-Au junctions and Au-Au nanocontacts. The measured thermal power, *I-V* characteristics and Seebeck coefficient are summarized in Fig. 5-3. In contrast to the BPDT case, TPDT molecular junctions exhibit significantly smaller cooling owing to their low electrical

conductance, in spite of a slightly higher Seebeck coefficient of +15.7 ± 1.1 μV K^{-1}. In Au-Au nanocontacts without molecules between the Au electrodes, there was no detectable cooling effect (Fig. 5-3 c) because of the extremely small Seebeck coefficient—a result in excellent agreement with the prediction of equation (5.3.1). This control experiment confirms that the molecules play a critical role in the observed cooling.

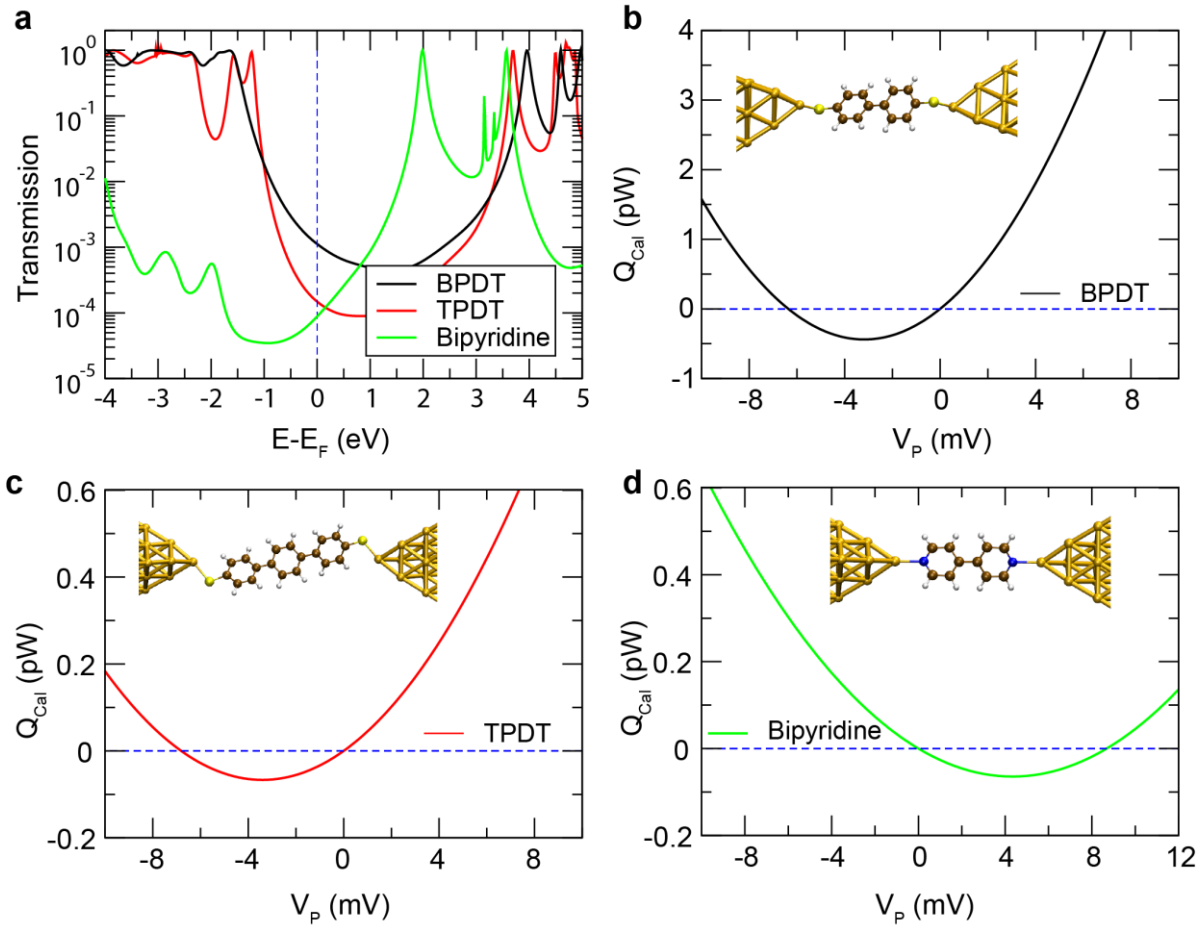

Figure 5-4 Computed heating/cooling effect in the molecular junctions used in this experiment. a, Calculated zero-bias transmission function as a function of energy, measured with respect to the Fermi energy (E_F), for BPDT, TPDT and BP junctions. The transmission and its derivative at E_F determine the electrical conductance and the Seebeck coefficient of the molecular junctions, respectively. b-d, Calculated heating and cooling power at different voltages for BPDT, TPDT and BP single-molecule junctions, respectively. The insets show the geometries used to compute the different transport properties.

Finally, we performed measurements using Au-4,4′-bipyridine (BP)-Au molecular junctions, in which transport is expected to be dominated by the LUMO level[2] (as also confirmed by our measurements of the Seebeck coefficients; see Fig. 5-3 f). In these experiments, in contrast to the measurements in HOMO-dominated junctions, we observed net cooling in the calorimeter for a positive bias applied to the probe (Fig. 5-3 e). The observed heat dissipation characteristics of Au-BP-Au junctions are consistent with the predictions of equation (5.3.1) using independent measurements of the electrical conductance and the Seebeck coefficient, as reflected by the excellent agreement between the experimental data and the result from equation (5.3.1). The physical picture for the observed cooling behavior in LUMO-dominated junctions is shown in Fig. 5-1 e.

To identify the microscopic origin of the observed heating and cooling effects in our molecular junctions, we used an *ab initio* transport model based on density functional theory[138] (DFT) to compute the transmission function ($\tau(E)$). To investigate whether our experimental observations are directly determined by the structure and properties of the molecules incorporated into the junction, we focus our computational analysis on single-molecule junctions. In Fig. 5-4 a, we summarize the results for the zero-bias transmission function for three junctions where the molecules under study (BPDT, TPDT and BP) are attached to Au electrodes via atop positions (insets in Fig. 5-4 b–d). For these calculations, we used the DFT + Σ method to attenuate known self-interaction errors in DFT and account for image charge effects[55, 141]. Then, using $\tau(E)$, we computed within the Landauer theory the electrical conductance, the Seebeck coefficient and the power released in the calorimeter (equation (5.3.1)). As we are interested in the low-bias regime, the bias-dependence of the transmission was ignored.

For the Au-BPDT-Au and Au-TPDT-Au junctions, the transport at the Fermi energy (E_F) is dominated by the HOMO of the molecules (Fig. 5-4 a), which results in a negative slope of the transmission at E_F and a positive Seebeck coefficient. In this example, the conductance of the BPDT junction is 1.1×10^{-3} G_0, where $G_0 = 2e^2/h = 12.9$ kΩ^{-1} is the conductance quantum, while for TPDT the conductance is 1.5×10^{-4} G_0, almost an order of magnitude lower as expected from the exponential decay of the conductance with molecular length. The corresponding Seebeck coefficients at room temperature are +10.5 μVK^{-1} for BPDT and +11.1 μVK^{-1} for TPDT, which are in good accord with our experimental observations. The results for the computed cooling power in single-molecule junctions (Fig. 5-4 b and c) predict that these junctions exhibit cooling for negative bias in a voltage range of $V_P \in$ [-7mV, 0mV], in excellent agreement with the voltage range for which cooling is observed in the experiments. The lower cooling power of TPDT is simply due to its lower conductance. Note that the difference in power values with respect to the experiments arises because we are simulating single-molecule junctions instead of the many-molecule junctions used in the work. Finally, the BP junction exhibits a conductance of 8.8×10^{-5} G_0, consistent with previous experimental and theoretical work9, transport is dominated by the LUMO (Fig. 5-4 a), with a negative Seebeck coefficient of -4.4 μVK^{-1}, and the cooling effect occurs at positive bias (Fig. 5-4 d) in a range $V_P \in$ [0mV, +9mV], again in qualitative agreement with our observations. A direct quantitative comparison between theory and experiments is primarily limited by the uncertainty in the number of molecules in the junction (note, however, that the Seebeck coefficient is independent of the number of molecules). These results strongly indicate that the observed cooling and heating are determined by the intrinsic properties of individual molecules.

5.4 Methods

5.4.1 Nanofabrication Process of Suspended Calorimetric Devices

The detailed steps for fabricating the suspended calorimetric microdevices are shown in Fig. 5-5. Briefly, a low-stress silicon nitride (SiNx) film that is 500 nm thick is first deposited onto a silicon wafer using LPCVD (Step 1). Subsequently, a 30 nm thick Pt serpentine line is patterned onto the SiNx layer using lift-off (Step 2). Then, Au leads with a thickness of 100 nm are defined on the SiNx layer using the same lift-off process (Step 3). The topology of the suspended region and the beams is created using RIE etching through the SiNx layer on the front side (Step 4). Windows in the SiNx layer, located on the backside of the silicon wafer, are then etched using RIE (Step 5). Subsequently, a through-hole in the silicon handler wafer is created by a KOH etch to release the suspended device (Step 6). After releasing the device, a 100 nm thick Al_2O_3 film is deposited on the whole device using atomic layer deposition (ALD) (Step 7) and serves to electrically isolate the Pt serpentine from the Au layer that will be deposited in the final step. Finally, the microdevice is coated with a 50 nm thick Au film that is deposited using sputtering (Step 8). Immediately after the deposition of the Au thin film, the microdevice is immersed into a molecular solution to form a self-assembled monolayer (SAM) of molecules.

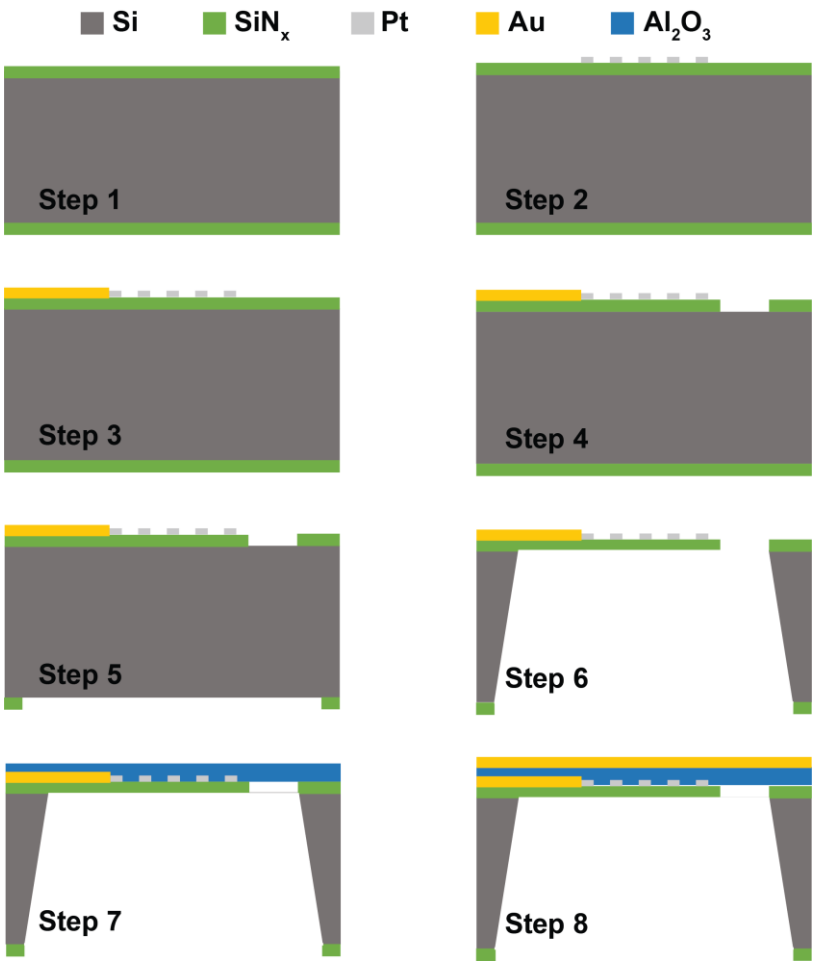

Figure 5-5 Nanofabrication of the suspended calorimetric devices. Detailed steps in the fabrication of the suspended calorimetric devices are described in the text.

5.4.2 Measurement of the Thermal Resistance and Thermal Time Constant of the Calorimetric Devices

The thermal resistance of the suspended microdevices was calibrated using an approach similar to that described in our previous work[159]. Briefly, the temperature rise of the device was measured by supplying a range of dc electrical currents to the integrated Pt serpentine line, which dissipated known amounts of heat in the suspended region of the microdevice. Figure 5-6 a plots the measured temperature rise (ΔT) against the power input (Q). The thermal

resistance of the microdevice can be readily obtained by using $R_S = \Delta T / Q$, which was estimated to be 3.35 (± 0.01) × 10^6 K/W.

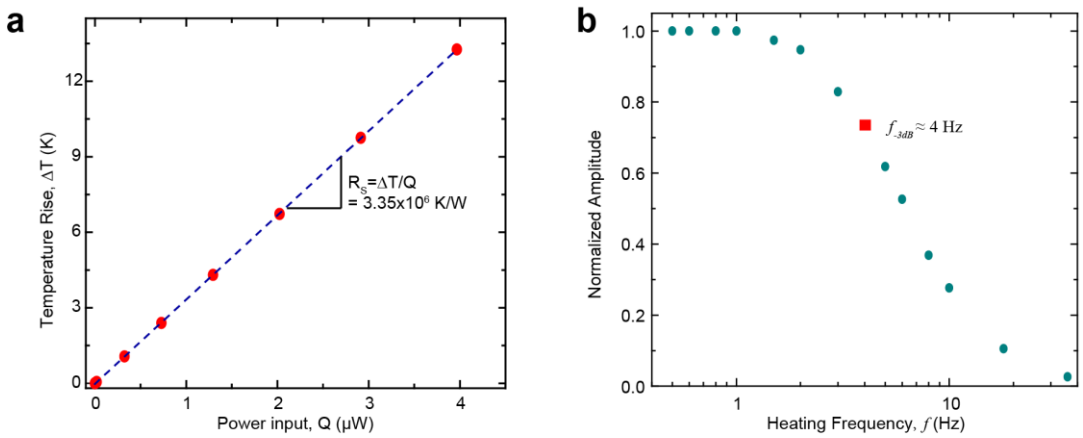

Figure 5-6 Calibration of the thermal resistance and thermal time constant of the calorimetric devices. a, Measured temperature rise of the device as a function of the input power. The thermal resistance is given by the slope of the fitted curve. b, Normalized temperature rise of the device as the frequency of the sinusoidal heat input is varied. The red square indicates the -3dB point.

To calibrate the thermal time constant of the microdevice, we supplied a sinusoidal heat current with fixed amplitude (I_f = 4 μA) and systematically varied the frequency of the current while measuring its temperature response. The Joule heating (Q_{2f}) occurs at a frequency 2f and produces temperature oscillations in the microdevice with an amplitude of ΔT_{2f}. This 2f component of the temperature change of the microdevice can be related to the voltage drop across the Pt thermometer at 3f, V_{3f}, using the relationship $V_{3f} = \Delta T \alpha I_f R / 2$, where α is the temperature coefficient of resistance and R is the nominal resistance of the Pt thermometer. The measured amplitude of the temperature fluctuations, normalized to the amplitude of the measured value at the lowest frequency, is plotted against the frequency in Fig. 5-6 b. We note

that the cut-off frequency (-3dB point) is at ~4 Hz. Therefore, the thermal time constant (τ) of the microdevice can be obtained using $\tau = (2\pi f_{-3dB})^{-1} \sim 40$ ms.

5.4.3 Surface Characterization of the Microdevices

The surface topography of the Au-coated microdevices was characterized by atomic force microscopy (AFM). As shown in Fig. 5-7, the RMS roughness of the suspended region was found to be less than 0.4 nm within a scanning area of 500 nm by 500 nm. We note that this flatness is comparable to that for template-stripped Au surfaces and facilitates the formation of self-assembled monolayer of molecules on the Au surface.

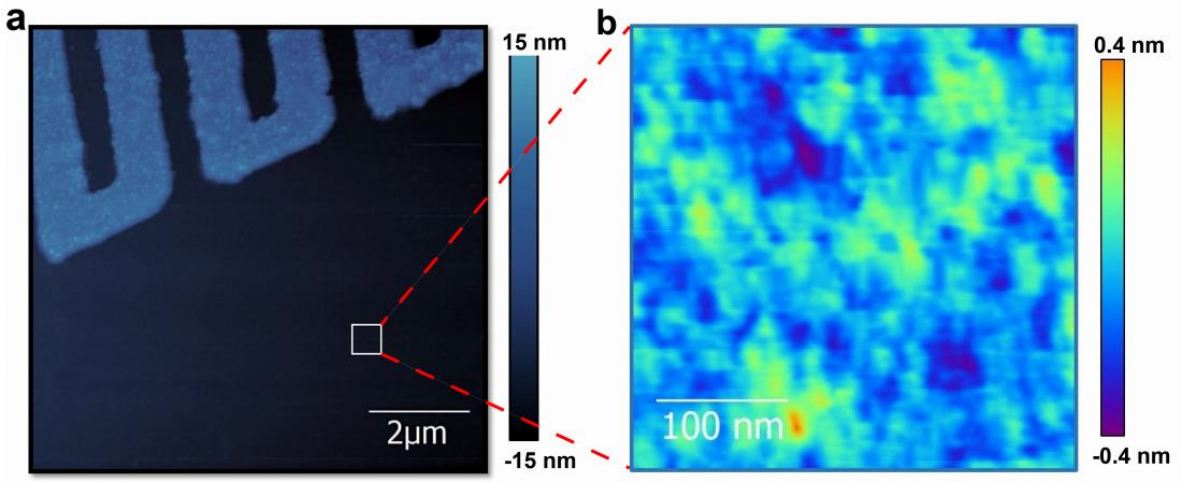

Figure 5-7 Surface topography of the suspended microdevices obtained by Atomic Force Microscopy (AFM). The Pt serpentine thermometer can be seen in (a). b, AFM scans performed on the planar region of the microdevice reveal a RMS roughness of ~0.4 nm within a 500 nm by 500 nm area.

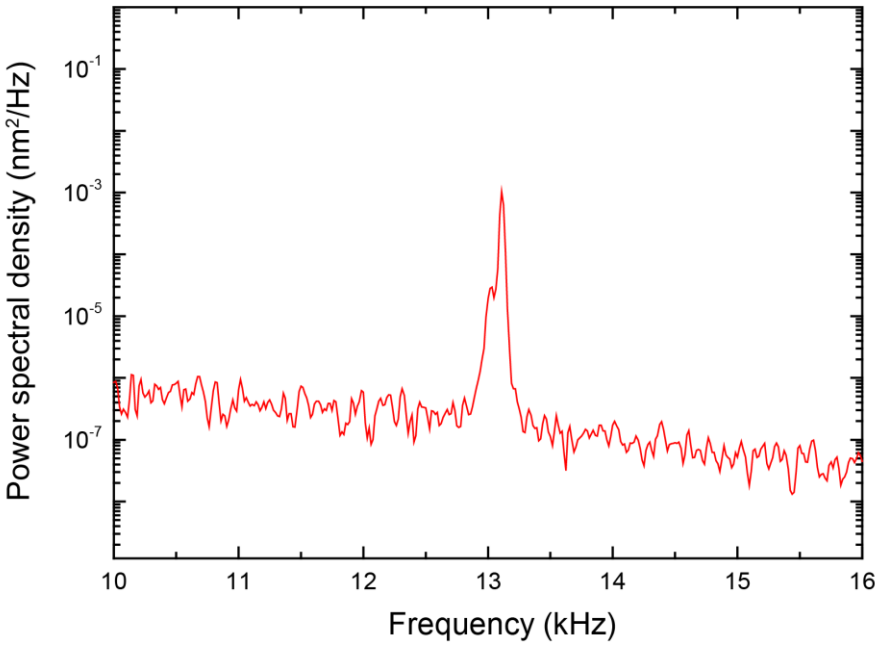

Figure 5-8 Power spectral density (PSD) of the deflection of AFM cantilever. The peak frequency at ~13 kHz corresponds to the resonance frequency of the cantilever, and the thermally-driven, mean squared displacement of the cantilever is about 0.039 nm^2.

5.4.4 Calibration of the Spring Constant of the AFM Probes

The spring constant of the AFM probes is estimated using the equipartition theorem[160]. Briefly, the spring constant of the AFM probe (k) and the temperature (T) of the thermal reservoir that the probe is connected to are related by: $\frac{1}{2}k\langle x^2\rangle = \frac{1}{2}k_BT$, where k_B is the Boltzmann constant and x is the displacement of the end of the tip due to random thermal fluctuation in the probe. To obtain the mean square displacement, $\langle x^2\rangle$, we monitored the thermally-driven deflections of the AFM cantilever with a position-sensitive photodiode detector. From a time series of the AFM cantilever displacement we computed the power spectral density (PSD) of the thermally driven oscillations. As shown in Fig. 5-8, the PSD

features a peak at ~13 kHz that corresponds to the resonant frequency of the AFM cantilever. The mean square displacement was obtained by integrating the PSD and was found to be ~0.039 nm^2. Finally, by substituting the estimated value of $\langle x^2 \rangle$, into the equipartition theorem the spring constant can be calculated to be ~0.1 N/m.

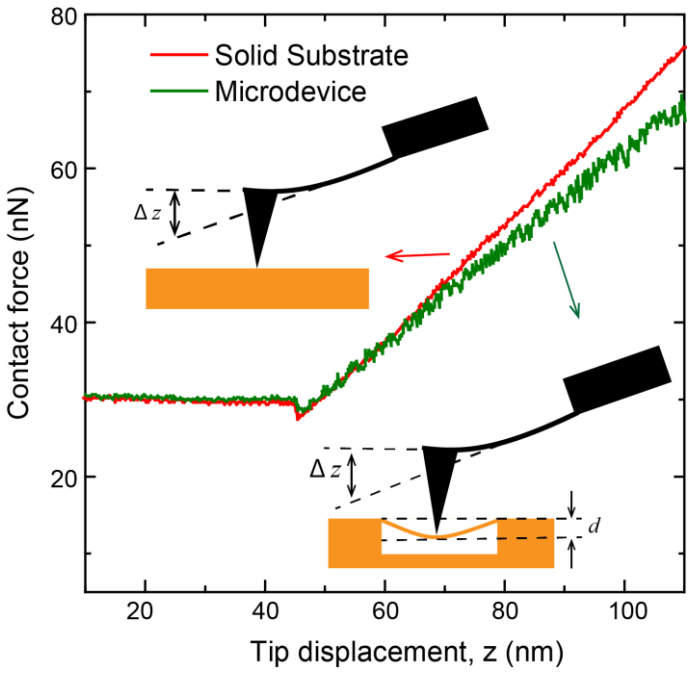

Figure 5-9 Stiffness calibration of the suspended calorimeter. Force-displacement curves of an AFM probe on the calorimeter and a solid substrate. The insets show the differences in deflection in the two different experiments. The stiffness of the microdevice calorimeter can be estimated from these measurements as described in the text.

5.4.5 Evaluation of the Stiffness of the Suspended Calorimetric Devices

Thermal fluctuations of suspended microdevices need to be minimized to sub-nanometer levels for creating stable molecular junctions, which requires that the suspended devices have sufficiently high mechanical stiffness. To measure the stiffness of the calorimetric devices we employed an approach similar to that used in a previous work[161]. Briefly, we employed an

AFM cantilever with a known spring constant (k_{Can}) of ~0.75 N/m and placed it in close proximity to a solid silicon (Si) substrate. The substrate was first displaced towards the cantilever and the force exerted on the cantilever as a function of the displacement was recorded (Fig. 5-9). Subsequently, we systematically repeated the same experiments with a suspended device (suspended region attached to a Si substrate via thin and long beams, see Fig. 5-1). The measured force vs. displacement curves are shown in Fig. 5-9. It can be seen that the slope of the force vs. displacement curve (m_1) recorded on the solid substrate is greater than the curve (m_2) obtained with the compliant device. The difference in force exerted on the cantilever in the two experiments is attributable to the compliance of the suspended device. Specifically, it can be shown that the stiffness of the suspended device (k_{Sus}) can be related to the stiffness of the cantilever (k_{Can}) by the following expression $k_{\mathrm{Sus}} = k_{\mathrm{Can}} / \left[\frac{m_1}{m_2} - 1\right]$, which yields a stiffness for the microdevice of 3.85 ± 0.11 N/m. This stiffness is significantly higher than the stiffness of the AFM probes used in the measurement (~0.1 N/m) and thus does not limit the stability of our junctions.

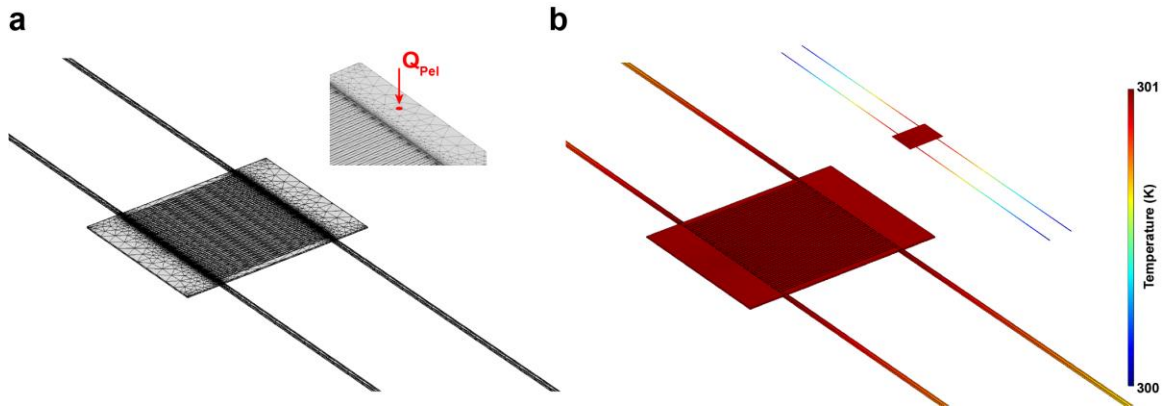

Figure 5-10 Modelling of the temperature distribution on the calorimetric microdevice. a, Meshing structure used in the simulation. A known amount of thermal power (300 nW) is applied to a small spot with an area of ~20 nm^2 at the edge of the suspended calorimeter device

(see inset). b, Calculated temperature field when the temperature increases by ~1 K on the suspended region. The temperature gradient is primarily restricted to the beams (see inset).

5.4.6 Analysis of the Uniformity of the Temperature Distribution of the Suspended Calorimeters

In measuring the heating and cooling power of the molecular junctions, one important question is whether the temperature of the suspended region is uniform when heating or cooling occurs in a localized area. To address this issue, we employed a COMSOL-based finite element analysis to analyze the temperature distribution within the microdevice in the presence of a finite heat flux (300 nW) applied to a small spot (~20 nm^2) on the surface. Figure 5.10 presents the meshing topology used in the simulation and the calculated result. It can be clearly seen that the temperature drop occurs primarily along the beams connecting the suspended region to the thermal reservoir and there are negligible thermal gradients across the suspended region. This ensures that the temperature reported by the Pt thermometer integrated on the suspended region can be readily used to estimate the thermal power applied on the microdevice.

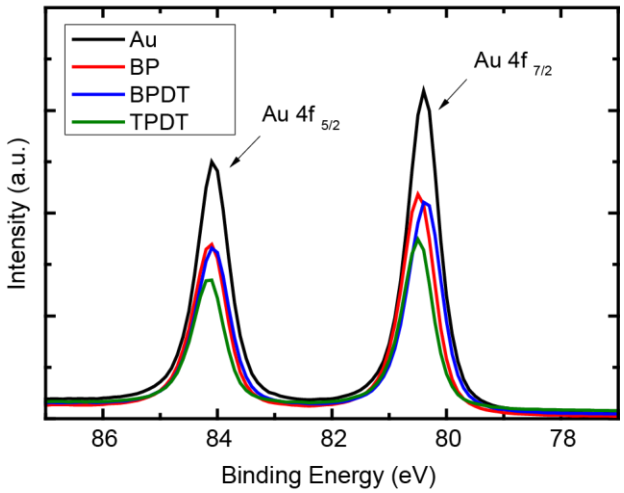

Figure 5-11 Characterization of the self-assembled monolayer using XPS. The photoelectron intensity on different monolayers as a function of the binding energy.

Table 5-1 Summary of the measured monolayer thicknesses using XPS and ellipsometry.

	BPDT	TPDT	BP
XPS (nm)	1.29 (0.14)	1.85 (0.19)	1.19 (0.16)
Ellipsometry (nm)	1.47 (0.07)	1.86 (0.08)	0.91 (0.08)

5.4.7 Ultra-low Noise Measurement Environment

All measurements described in this work were performed using an ultra-high vacuum scanning probe microscope (RHK UHV 7500), which was housed in an ultra-low-noise facility that features excellent vibration-isolation (meeting the stringent NIST-A criterion) and temperature stability (<100 mK drift over 24 hours).

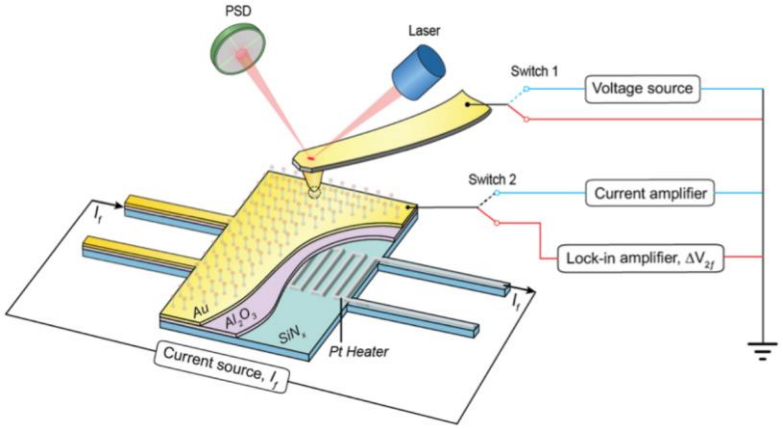

Figure 5-12 Schematic describing the approach employed for thermoelectric voltage measurements on molecular junctions.

5.4.8 Characterization of the Self-Assembled Monolayer of Molecules

We employed X-ray photoelectron spectroscopy (XPS) and ellipsometry to determine the monolayer thickness of the self-assembled monolayer. The representative measured results are presented in Fig. 5-11 and the estimated thicknesses are summarized in Table 5-1. The XPS experiments were performed on a Kratos Axis Ultra system using a monochromatic Al X-ray source at a setting of 8 mA and 14 kV. The estimated thickness is based on the exponential attention of the substrate photoelectrons in the presence of the self-assembled monolayer[162-165] (as shown in Fig. 5-11). The ellipsometry measurements were performed on the Woollam M-2000 Ellipsometer. Incident light beams at angles of 55°, 65° and 75°, over the wavelengths from 400–1700 nm were used for this characterization and the data were fit with an optical model (using CompleteEASE^{TM} V4.86) to extract the thickness of the monolayer. It can be seen in Table 5-1 that the two measurement approaches yield consistent results, which agree well with previously reported thicknesses[18, 166-168].

The number of molecules in the junctions can be estimated by applying a simple, contact-mechanics model (Hertzian theory). Specifically, the radius of contact between the Au AFM tip and the SAM can be estimated from Hertzian contact mechanics[169] to be $r = \sqrt[3]{R_{tip}F/E}$, where R_{tip} is the radius of the tip, F is the apparent load on the contact, and E is the Young's modulus. Taking F to be 16 nN which sums the pull-off load of ~15 nN and the applied load of 1 nN, R_{tip} = 100 nm, and E = 79 GPa for Au, we estimate the contact radius r to be 2.7 nm, corresponding to a contact area of ~23 nm^2. Based on the expected packing density of the benzene dithiol molecules on the Au[170] substrate of ~5 × 10^{14} molecules/cm^2 we estimate that the junction contains approximately 100–110 molecules. Moreover, we also employed the well-known Johnson-Kendall-Roberts (JKR) model[171] which was developed based on the classic Hertzian contact mechanics to calculate the contact area and didn't find significant difference in estimating the number of molecules compare to the classic model. Furthermore, the number of molecules in the junction can also be justified from the electrical conductance measurement. By comparing the reported value of the single-molecule junction, BPDT for example which is ~2.6 MΩ (5 × 10^{13} G_0)[122] to the measured electrical conductance of the SAM which is ~37 μS (27 KΩ), we can estimate the number of the molecules in the junction to be approximately 100, by assuming the electrical conduction of the molecules are independent from each other.

5.4.9 Electric Circuitry

As depicted in Fig. 5-1 a, the low-bias electrical conductance of the molecular junctions is measured by applying a small voltage bias (below 20 mV) across the junctions and measuring the electric current using a current amplifier (Keithley 428). The current-flow in

the molecular junctions generates both Peltier and Joule effects in the electrodes. The thermal power (heating or cooling) was measured by monitoring the temperature change of the suspended calorimeter 10 using the integrated Pt thermometer. This was accomplished by measuring the electrical resistance change of the Pt resistor in a half-Wheatstone bridge configuration whose voltage output was first amplified by an instrumentation amplifier (AD 524) with a gain of 100, and then supplied into a second voltage amplifier (SRS 760) with a gain of 10. Furthermore, current-voltage (*I*-*V*) characteristics of the molecular junctions were measured by linearly increasing the voltage bias (from ~ -0.5 V to 0.5 V) and measuring the resultant electric current. The approach employed for measuring the Seebeck coefficients of molecular junctions is shown in Fig. 5-12.

Temperature change (ΔT) of the microdevice due to the Peltier cooling/Joule heating in the molecular junction can be estimated by $\Delta T = V_{Cal} / I_{in} R_{Pt} \alpha$, where V_{Cal} is the voltage output across the Pt thermometer, I_{in} is the input electric current (see Fig. 5-1 a) and R_{Pt} and α are the resistance the temperature coefficient of resistance of the Pt thermometer, respectively. We note that the Joule heating induced by I_{in} is estimated to elevate the temperature of the microdevice by ~10 K.

5.4.10 Details of Applying the Time Averaging Scheme in Data Processing

To implement the time averaging scheme measurements of heating and cooling in molecular junctions, we applied repeated sequences of three level voltage biases across junctions and recorded the resulting electrical conductance and the temperature rise of the suspended calorimeter (as shown in Fig. 5-2 a) for an extended period of time. Depending on

the desired signal to noise ratio and the magnitude of the thermal power output, the number of three-level periods over which data were collected was varied. Specifically, for the data shown in Fig. 5-2 b the number of periods over which data were averaged at each bias are as follows: 450 (9 mV), 720 (8 mV), 1320 (7 mV), 600 (5 mV), 1500 (2 mV), and 2000 (1 mV), respectively. In general, the number of periods required to resolve signals increased with decreasing power output.

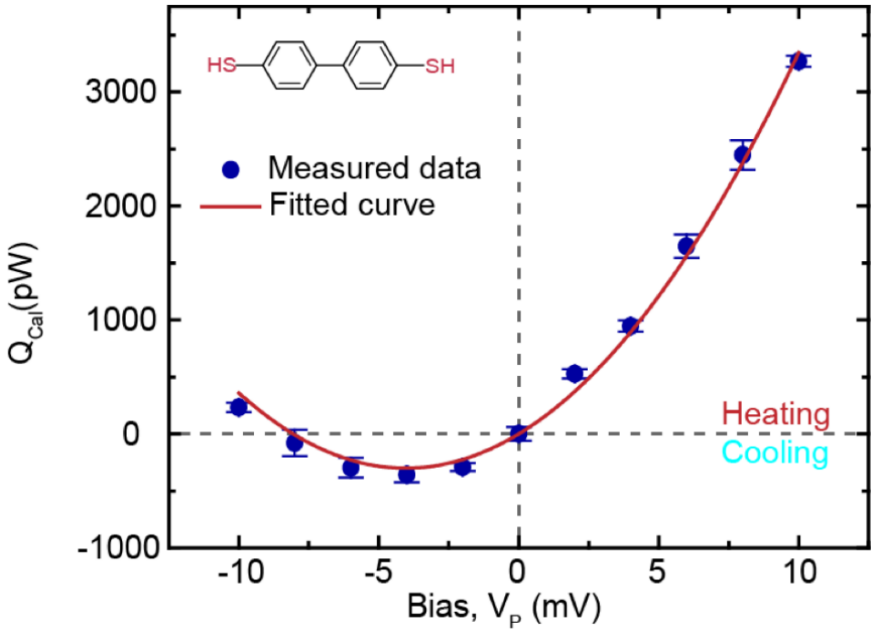

Figure 5-13 Second independent data set for the voltage-dependent cooling/heat generation in BPDT junctions. The solid red line indicates the fitted curve using Eq. 5.3.1 and the measured Seebeck coefficient and electrical conductance.

In performing these heat dissipation/cooling measurements we observed small changes in the electrical conductance of the junction (~5% - 10%) during the time course of the measurement. In order to (systematically) account for the variations of the conductance we normalized all the measured power outputs by the electrical conductance relative to that measured at a bias of 3 mV. Finally, we note that these results are independent of the samples

and were found to be repeatable with multiple probes and microdevices calorimeters. An additional data set from a different microdevice and probe obtained over a wider range of biases for BPDT molecular junctions is shown in Fig. 5-13. It can be seen the observed cooling minima is virtually identical to the data shown in Fig. 5-2 c.

5.4.11 Description of the Temperature Resolution of the Pt Thermometer

To evaluate the temperature resolution of the Pt thermometer of the calorimeter, we followed the protocols developed by us in previous work12, 13. Briefly, our measurement applied an unmodulated electrical current into the Pt line to quantify the modulated temperature change due to the applied three-level voltage bias. The noise components in this experiment include contributions from the electronic system (amplifiers), thermal Johnson noise, shot noise, and the temperature fluctuation from the ambient environment. Following the procedure described in detail elsewhere[120] by us we estimate that the temperature resolution of our modulations based on approach to be given by:

$$\Delta T_{Res} = \left[\int_0^{\infty} G_N(f) \left[\frac{\mathrm{Sin}(2\pi f T}{2\pi f T} \right]^2 \times \left[\frac{6\,\mathrm{Sin}(\pi f \Delta t)}{1 + 2\,\mathrm{Cos}(2\pi f \Delta t)} \right]^2 df \right]^{\frac{1}{2}} \qquad (5.4.1)$$

where $G_N(f)$ is the power spectral density associated with temperature noise, (i.e. the period of each three-level cycle) and $2T$ is the total time over which each set of three-level excitations were performed. For example, as described in the section above for the bias with 1 mV amplitude, the three-level excitation for this measurement was repeat for a total of 2000 cycles, where each cycle was 5 seconds long. Therefore, $2T = 2000 \times 5 = 10000$ seconds for the 1 mV

voltage amplitude experiments. Further, we note that we have previously[172] analyzed the noise spectral characteristics of resistance thermometers and had estimated $G_N(f)$. Using this information in conjunction with Eq. 5.4.1, we estimate, that for measurements performed for 2000 cycles, our temperature resolution is better than 0.1 mK, thus giving us a heat current resolution that is below 30 pW.

5.4.12 Physical Mechanisms of Cooling and Heat Dissipation in Molecular Junctions

To qualitatively understand the physical processes that result in cooling we consider the schematics shown in Fig. 5-14 a-c where the left electrode is grounded and represents the electrode integrated into the calorimeter and the right electrode is negatively biased and represents the probe. In these scenarios electrons are injected into the right electrode (probe) at an energy of $\mu_{Cal} + e|V_P|$ and leave the left electrode (calorimeter) at an energy μ_{Cal}. This implies that if N electrons flow through the junction there is a net heat dissipation that is given by $Ne|V_P|$.

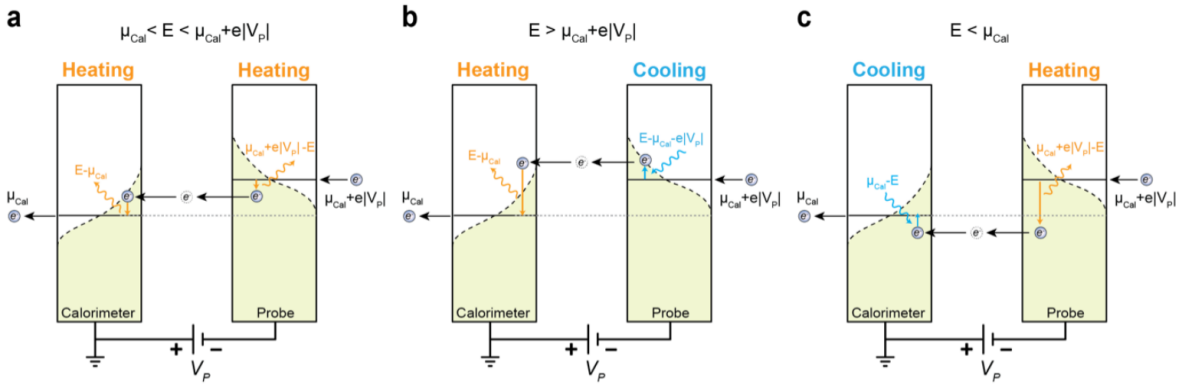

Figure 5-14 Schematic describing the physical mechanism involved in heating and cooling in molecular junctions. a, A scenario where an electron is transmitted between the chemical potentials of the electrodes. b, A scenario where an electron is transmitted above the chemical

potential of the probe. c, A scenario where an electron is transmitted below the chemical potential of the calorimeter.

To understand the origin of cooling it is essential to first note that flow of charge occurs in a range of energies, *i.e*. at all energies between the chemical potentials of the electrodes and in a small range of energies (~few k_BT) above the chemical potential of the probe and below the chemical potential of the calorimeter. As is described in more detail below, the electrons flowing between the chemical potentials of the electrodes cause heating in both electrodes. However, the electrons flowing above the chemical potential of the probe ($\mu_{Cal} + e|V_P|$) produce heating in the calorimeter and cooling in the probe. Further, electrons flowing below the chemical potential of the calorimeter (μ_{Cal}) cause cooling in the calorimeter and heating in the probe. From this discussion it is obvious that, for the given bias conditions, if the number of electrons transmitted below μ_{Cal} dominate the charge transfer then it is possible to achieve net cooling in the calorimeter. Below, we first describe the heating and cooling characteristics of electrons transmitted at various energies.

Heating due to electrons transmitted between chemical potentials:

Fig. 5-14 a shows the scenario where an electron is transmitted at an energy E between the chemical potentials. In this case the electron must dissipate as heat some of its energy ($\mu_{Cal} + e|V_P| - E$) in the probe and the rest of energy of ($E - \mu_{Cal}$) in the calorimeter. Thus, charge transfer at energies between the chemical potentials results in heat generation in both the electrodes and the total heat generation per electron is $e|V_P|$.

Heating/Cooling due to electrons transmitted above the chemical potential of the probe:

When electrons are transmitted at an energy $E > \mu_{Cal} + e|V_P|$ (see Fig. 5-14 b) the electrons absorb energy $E - \mu_{Cal} - e|V_P|$ from the probe resulting in cooling in the probe and dissipate energy $E - \mu_{Cal}$ in the calorimeter. Notice that the net heat generation by the electron in the device $((E - \mu_{Cal}) - (E - \mu_{Cal} - e|V_P|) = e|V_P|)$ is still the same as that for electrons transmitted between the chemical potentials.

Heating/Cooling due to electrons transmitted below the chemical potential of the calorimeter:

When electrons are transmitted at an energy $E < \mu_{Cal} + e|V_P|$ (see Fig. 5-14 c) they dissipate as heat some energy $(\mu_{Cal} + e|V_P| - E)$ in the probe resulting in heating of the probe and they absorb some energy $(E - \mu_{Cal})$ in the calorimeter, resulting in cooling of the calorimeter. Again, notice that the net heat generation by the electron in the device $((E - \mu_{Cal}) - (E - \mu_{Cal} - e|V_P|) = e|V_P|)$ is still the same as that for electrons transmitted between the chemical potentials.

Relationship between transmission function and cooling:

From the qualitative description provided above it is clear that when the calorimeter electrode is grounded, and the probe is negatively biased, net cooling can occur in the calorimeter if the cooling provided by electrons transmitted below μ_{Cal} is larger than the heating produced by electrons transmitted at other energies. This can happen only when the transmission probabilities are larger at μ_{Cal} than those at $\mu_{Cal} + e|V_P|$. This in turn implies that the transmission function has a negative slope, *i.e.* $(\partial T / \partial E)_{E=\mu Cal}$ is negative, implying a positive Seebeck coefficient. This prediction is consistent with Eq. 5.3.1, which suggests that when a negative bias is applied to the probe, the calorimeter can be cooled if the Seebeck coefficient of the junction is positive. From the qualitative arguments provided above it can

also be seen that, for net cooling to be observed, the heat dissipation due to electrons transmitted between the chemical potentials must also be small as they result in only heat dissipation. For this reason, cooling can only be observed at low voltage biases. Finally, if the transmission function is only weakly dependent on energy then the cooling due to electrons transmitted below μ_{Cal} and heating due to electrons transmitted above $\mu_{Cal} + e|V_P|$ tend to cancel each other resulting in no observable cooling.

5.5 Conclusion

In conclusion, we have experimentally observed cooling in molecular junctions. Our experimental results also link the charge transmission characteristics of a molecule to the Peltier effects measured in molecular junctions. Furthermore, the experimental platform reported here allows the seamless characterization of electrical, thermal and thermoelectric transport properties on the same molecular junction in a unified manner. This work should stimulate further systematic exploration of atomic- and molecular-scale thermal transport[7, 34, 159] and quantification of the thermoelectric figure of merit in a variety of interesting molecules, nanostructures and materials.

Chapter 6 Summary and Future Work

6.1 Summary

In this dissertation I presented work on investigating charge transport and thermoelectricity in molecular junctions. Both scanning tunneling microscope break junction (STM-BJ) and conductive-probe atomic force microscope (CP-AFM) techniques were employed in order to perform single-molecular junction and monolayer measurements.

In an effort to probe the influence of quantum interference in molecular junctions, I studied transport in two oligo(phenylene ethynylene) (OPE) derivatives, *para*-OPE3 and *meta*-OPE3, which feature exactly the same chemical composition but different connectivity on the center benzene rings. Destructive interference arises as a result of the meta connection, which in turn leads to a decrease in the the electrical conductance (1.2×10^{-4} G_0 for para junctions, 1.1×10^{-5} G_0 for meta junctions) and increase in the Seebeck coefficient (~10 μV/K for para junctions, ~20 μV/K for meta junctions). Both single-molecule and monolayer experiments were performed, the results from both techniques were found to correspond well with each other and agree with theoretical predictions made by our collaborators.

Although improved thermoelectricity was achieved in molecular junctions, destructive quantum interference unavoidably results in a reduced electrical conductance, which is undesired for a thermoelectric device. As an alternate approach to tune thermoelectricity in molecular junctions, I present work on metallo-porphyrin based molecular junctions, in which

the charge transport mechanism varies depending on the metallic ion incorporated in the porphyrin. The junctions chosen here are Au-porphyrin-Au, Au-(Cu-porphyrin)-Au and Au-(Zn-porphyrin)-Au. In order to further improve the thermoelectric performance in these junctions, a C-Au direct bond between the molecular backbone and Au electrodes was created. The results of single-molecular junction experiments show tunable electrical conductance and thermopower in the molecular junctions with varied metal centres, and almost two orders of magnitude increase in electrical conductance compared to junctions with thiol end groups in previous research. Among three junctions studied in this work, the Au-(Zn-porphyrin)-Au junction exhibits both the highest electrical conductance and highest thermopower.

Along with the thermoelectricity phenomenon discussed above, I presented work on investigating Peltier cooling in molecular junctions. The molecular junctions studied here, Au-(biphenyl-4,4'-dithiol)-Au, Au-(terphenyl-4,4''-dithiol)-Au and Au-(4,4'-bipyridine)-Au, are stereotypical junctions whose thermopower has been extensively studied. A conductive-probe AFM-based setup, in conjunction with a picowatt resolution calorimeter, acts as a platform facilitating the measurements of electrical conductance, thermoelectricity and heat dissipation. Peltier cooling in molecular junctions was observed at small bias voltage, and the relationship between heating/cooling and charge transport mechanism were discussed. This work not only reveals Peltier cooling in molecular junctions which is a critical step in establishing molecular-based refrigeration, but also provides an experimental platform in investigating thermal transport, thermoelectricity and electrical conductance.

6.2 Future Work -- Tuning Thermoelectricity in Molecular Junctions via Formation of Charge Transfer Complex

Molecular junctions, as potential building blocks in nano-scale electronic devices, hold great promise for nanotechnologies applications including energy conversion devices. Here, I briefly describe future research directions related to charge transport and thermoelectricity in molecular junctions aiming at improving thermoelectric performance in molecular junctions.

The structures of organic charge transfer (CT) salts play a critical role in determining their mode of charge transport[173], and hence their unusual electrical properties, which range from semiconducting through metallic to superconducting. The discovery that treatment of the aromatic hydrocarbon perylene with bromine resulted in the formation of a black, crystalline and surprisingly conductive (10^{-2} $S \cdot cm^{-1}$) organic material initiated the systematic study of charge transfer complexes. Following the syntheses of regioregular poly-3-alkylthiophenes and the discovery that thin films of these materials can have good semiconductor properties, oligo- and polythiophene derivatives have become widely-studied materials in organic electronics.

In contrast, recent work shows that the conductance of single molecular junctions involving either a terthiophene or a simple 1,4-phenylene moiety increase by over an order of magnitude upon formation of their charge transfer complexes with tetracyanoethylene (TCNE)[174]. Here TCNE act as electron acceptor and the organic molecules act as electron donors. The large conductance enhancement is due to the creation of a new quantum resonance in the transmission function of the junction upon complex formation that is close to the contact Fermi energy.[173]

Future work can focus on molecules such as those shown in Fig. 6-1 (6[Ph]6 and 6[T3]6), which hold significant promise for boosting both electric conductance and Seebeck coefficients through the introduction of Fano resonance in the transmission function near the contact Fermi energy. It is also claimed that since TCNE is a strong electron acceptor, the position of the orbital responsible for the Fano resonance automatically adjusts to achieve the filling[174]. This makes the resonance peak relatively independent of the location and orientation of the TCNE relative to the molecule backbone. As a result, the junction of these two molecules are expected to have giant thermopower at room temperature without gating.

Besides the two molecules with reported enhanced electrical conductance when charge transfer complexes are formed, other molecules that are strong electron donors – 6[PhOMe2]6 and T4-Me (Fig. 6-1) are also good candidates for improving thermoelectricity under the same mechanism. It is suggested[174] that the conductance enhancement is an inherent property of the TCNE complexation, rather than a property of a particular donor molecule. In this case, one may expect enhancement in electrical conductance in 6[PhOMe2]6:TCNE and T4-Me:TCNE junctions as well.

As an even stronger acceptor compared to TCNE, tetracyanoquinodimethane (TCNQ) is also promising in enhancing the thermopower of metal-molecule-metal junctions.

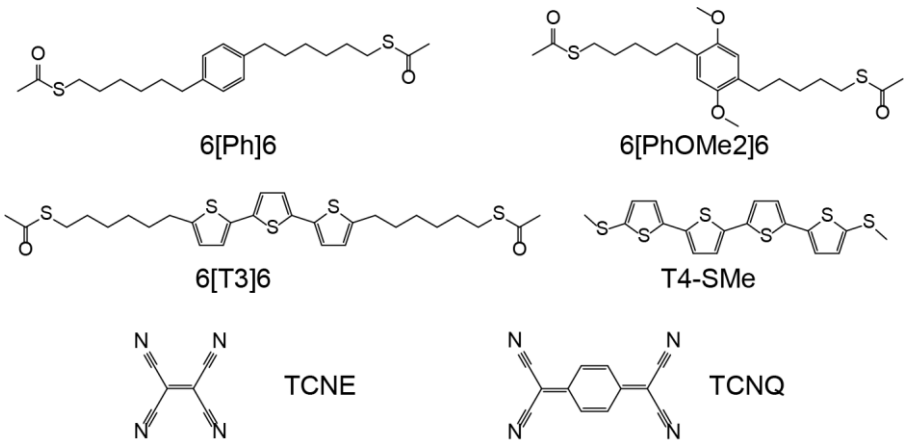

Figure 6-1Chemical Structures of discussed molecules for charge transfer complex formation.

Bibliography

1. Cuevas, J. C.; Scheer, E., *Molecular electronics : an introduction to theory and experiment*. World Scientific: Singapore ; Hackensack, NJ, (2010).
2. Aradhya, S. V.; Venkataraman, L. *Single-molecule junctions beyond electronic transport*. *Nat Nanotechnol* **8** (6), 399-410, (2013).
3. Tao, N. J. *Electron transport in molecular junctions*. *Nat Nanotechnol* **1** (3), 173-81, (2006).
4. Ratner, M. *A brief history of molecular electronics*. *Nat Nanotechnol* **8** (6), 378-381, (2013).
5. Song, H.; Reed, M. A.; Lee, T. *Single Molecule Electronic Devices*. *Adv Mater* **23** (14), 1583-1608, (2011).
6. Lee, W.; Song, B.; Reddy, P. *Measurement of thermoelectric and thermal transport properties of single-molecule junctions*. *Annu. Rev. Heat Transfer* **16** (1), 259-286, (2013).
7. Cui, L. J.; Miao, R. J.; Jiang, C.; Meyhofer, E.; Reddy, P. *Perspective: Thermal and thermoelectric transport in molecular junctions*. *J Chem Phys* **146** (9), 092201, (2017).
8. Dubi, Y.; Di Ventra, M. *Colloquium: Heat flow and thermoelectricity in atomic and molecular junctions*. *Rev Mod Phys* **83** (1), 131-155, (2011).
9. Bergfield, J. P.; Ratner, M. A. *Forty years of molecular electronics: Non-equilibrium heat and charge transport at the nanoscale*. *Phys Status Solidi B* **250** (11), 2249-2266, (2013).
10. Xiang, D.; Wang, X. L.; Jia, C. C.; Lee, T.; Guo, X. F. *Molecular-Scale Electronics: From Concept to Function*. *Chem Rev* **116** (7), 4318-4440, (2016).
11. Aviram, A.; Ratner, M. A. *Molecular Rectifiers*. *Chem Phys Lett* **29** (2), 277-283, (1974).
12. Reed, M. A.; Zhou, C.; Muller, C. J.; Burgin, T. P.; Tour, J. M. *Conductance of a molecular junction*. *Science* **278** (5336), 252-254, (1997).
13. Song, H.; Kim, Y.; Jang, Y. H.; Jeong, H.; Reed, M. A.; Lee, T. *Observation of molecular orbital gating*. *Nature* **462** (7276), 1039-1043, (2009).
14. Reed, M. A. *Inelastic electron tunneling spectroscopy*. *Mater Today* **11** (11), 46-50, (2008).
15. Muller, C. J.; Krans, J. M.; Todorov, T. N.; Reed, M. A. *Quantization effects in the conductance of metallic contacts at room temperature*. *Phys Rev B* **53** (3), 1022-1025, (1996).
16. Xu, B. Q.; Tao, N. J. *Measurement of single-molecule resistance by repeated formation of molecular junctions*. *Science* **301** (5637), 1221-1223, (2003).
17. Tan, A.; Sadat, S.; Reddy, P. *Measurement of thermopower and current-voltage characteristics of molecular junctions to identify orbital alignment*. *Appl Phys Lett* **96** (1), 013110, (2010).

18. Tan, A.; Balachandran, J.; Sadat, S.; Gavini, V.; Dunietz, B. D.; Jang, S. Y.; Reddy, P. *Effect of Length and Contact Chemistry on the Electronic Structure and Thermoelectric Properties of Molecular Junctions*. *J Am Chem Soc* **133** (23), 8838-8841, (2011).
19. Tan, A. R.; Balachandran, J.; Dunietz, B. D.; Jang, S. Y.; Gavini, V.; Reddy, P. *Length dependence of frontier orbital alignment in aromatic molecular junctions*. *Appl Phys Lett* **101** (24), 243107, (2012).
20. Xiang, D.; Jeong, H.; Kim, D.; Lee, T.; Cheng, Y. J.; Wang, Q. L.; Mayer, D. *Three-Terminal Single-Molecule Junctions Formed by Mechanically Controllable Break Junctions with Side Gating*. *Nano Lett* **13** (6), 2809-2813, (2013).
21. Xiang, D.; Jeong, H.; Lee, T.; Mayer, D. *Mechanically Controllable Break Junctions for Molecular Electronics*. *Adv Mater* **25** (35), 4845-4867, (2013).
22. Kim, Y.; Jeong, W.; Kim, K.; Lee, W.; Reddy, P. *Electrostatic control of thermoelectricity in molecular junctions*. *Nat Nanotechnol* **9** (11), 881-885, (2014).
23. Chang, W. B.; Russ, B.; Ho, V.; Urban, J. J.; Segalman, R. A. *Gold nanocrystal arrays as a macroscopic platform for molecular junction thermoelectrics*. *Phys Chem Chem Phys* **17** (9), 6207-6211, (2015).
24. Giessibl, F. J. *Atomic resolution on Si(111)-(7x7) by noncontact atomic force microscopy with a force sensor based on a quartz tuning fork*. *Appl Phys Lett* **76** (11), 1470-1472, (2000).
25. Ward, D. R.; Halas, N. J.; Ciszek, J. W.; Tour, J. M.; Wu, Y.; Nordlander, P.; Natelson, D. *Simultaneous measurements of electronic conduction and Raman response in molecular junctions*. *Nano Lett* **8** (3), 919-924, (2008).
26. Schwobel, J.; Fu, Y. S.; Brede, J.; Dilullo, A.; Hoffmann, G.; Klyatskaya, S.; Ruben, M.; Wiesendanger, R. *Real-space observation of spin-split molecular orbitals of adsorbed single-molecule magnets*. *Nat Commun* **3**, (2012).
27. Reddy, P.; Jang, S. Y.; Segalman, R. A.; Majumdar, A. *Thermoelectricity in molecular junctions*. *Science* **315** (5818), 1568-1571, (2007).
28. Nitzan, A.; Ratner, M. A. *Electron transport in molecular wire junctions*. *Science* **300** (5624), 1384-1389, (2003).
29. Chen, F.; Hihath, J.; Huang, Z.; Li, X.; Tao, N. J. *Measurement of single-molecule conductance*. *Annu Rev Phys Chem* **58**, 535-64, (2007).
30. Sun, L.; Diaz-Fernandez, Y. A.; Gschneidtner, T. A.; Westerlund, F.; Lara-Avila, S.; Moth-Poulsen, K. *Single-molecule electronics: from chemical design to functional devices*. *Chem Soc Rev* **43** (21), 7378-411, (2014).
31. Nichols, R. J.; Higgins, S. J. *Single-Molecule Electronics: Chemical and Analytical Perspectives*. *Annu. Rev. Anal. Chem* **8**, 389-417, (2015).
32. Galperin, M.; Ratner, M. A.; Nitzan, A.; Troisi, A. *Nuclear coupling and polarization in molecular transport junctions: Beyond tunneling to function*. *Science* **319** (5866), 1056-1060, (2008).
33. Galperin, M.; Ratner, M. A.; Nitzan, A. *Molecular transport junctions: vibrational effects*. *J Phys-Condens Mat* **19** (10), 103201, (2007).
34. Segal, D.; Agarwalla, B. K. *Vibrational Heat Transport in Molecular Junctions*. *Annu Rev Phys Chem* **67**, 185-209, (2016).
35. Malen, J. A.; Yee, S. K.; Majumdar, A.; Segalman, R. A. *Fundamentals of energy transport, energy conversion, and thermal properties in organic-inorganic heterojunctions*. *Chem Phys Lett* **491** (4-6), 109-122, (2010).

36. Rincon-Garcia, L.; Evangeli, C.; Rubio-Bollinger, G.; Agrait, N. *Thermopower measurements in molecular junctions*. *Chem. Soc. Rev.* **45** (15), 4285-306, (2016).
37. Finch, C. M.; Garcia-Suarez, V. M.; Lambert, C. J. *Giant thermopower and figure of merit in single-molecule devices*. *Phys Rev B* **79** (3), 033405, (2009).
38. Bergfield, J. P.; Solis, M. A.; Stafford, C. A. *Giant Thermoelectric Effect from Transmission Supernodes*. *Acs Nano* **4** (9), 5314-5320, (2010).
39. Nakpathomkun, N.; Xu, H. Q.; Linke, H. *Thermoelectric efficiency at maximum power in low-dimensional systems*. *Phys Rev B* **82** (23), 235428, (2010).
40. Vacek, J.; Chocholousova, J. V.; Stara, I. G.; Stary, I.; Dubi, Y. *Mechanical tuning of conductance and thermopower in helicene molecular junctions*. *Nanoscale* **7** (19), 8793-8802, (2015).
41. Henry, A.; Chen, G. *High Thermal Conductivity of Single Polyethylene Chains Using Molecular Dynamics Simulations*. *Phys Rev Lett* **101** (23), 235502, (2008).
42. Liu, J.; Yang, R. G. *Length-dependent thermal conductivity of single extended polymer chains*. *Phys Rev B* **86** (10), 104307, (2012).
43. Landauer, R. *Spatial Variation of Currents and Fields Due to Localized Scatterers in Metallic Conduction*. *Ibm J Res Dev* **1** (3), 223-231, (1957).
44. Landauer, R. *Conductance Determined by Transmission - Probes and Quantized Constriction Resistance*. *J Phys-Condens Mat* **1** (43), 8099-8110, (1989).
45. Imry, Y., *Introduction to mesoscopic physics*. Oxford University Press: New York, (1997); p xiii, 234 p.
46. Datta, S., *Quantum transport : atom to transistor*. 1st pbk. ed. Cambridge University Press: Cambridge, UK ; New York, (2013); p xiv, 404 p.
47. Butcher, P. N. *Thermal and Electrical Transport Formalism for Electronic Microstructures with Many Terminals*. *J Phys-Condens Mat* **2** (22), 4869-4878, (1990).
48. Paulsson, M.; Datta, S. *Thermoelectric effect in molecular electronics*. *Phys Rev B* **67** (24), (2003).
49. Ke, S. H.; Yang, M.; Curtarolo, S.; Baranger, H. U. *Thermopower of Molecular Junctions: An ab Initio Study*. *Nano Lett* **9** (3), 1011-1014, (2009).
50. Leijnse, M.; Wegewijs, M. R.; Flensberg, K. *Nonlinear thermoelectric properties of molecular junctions with vibrational coupling*. *Phys Rev B* **82** (4), 045412, (2010).
51. Claughton, N. R.; Lambert, C. J. *Thermoelectric properties of mesoscopic superconductors*. *Phys Rev B* **53** (10), 6605-6612, (1996).
52. Huser, F.; Solomon, G. C. *From Chemistry to Functionality: Trends for the Length Dependence of the Thermopower in Molecular Junctions*. *J Phys Chem C* **119** (25), 14056-14062, (2015).
53. Solomon, G. C. *Molecular Thermopower Feeling the Squeeze*. *Nat Mater* **15** (3), 254-255, (2016).
54. Burkle, M.; Zotti, L. A.; Viljas, J. K.; Vonlanthen, D.; Mishchenko, A.; Wandlowski, T.; Mayor, M.; Schon, G.; Pauly, F. *Ab initio study of the thermopower of biphenyl-based single-molecule junctions*. *Phys Rev B* **86** (11), 115304, (2012).
55. Zotti, L. A.; Burkle, M.; Pauly, F.; Lee, W.; Kim, K.; Jeong, W.; Asai, Y.; Reddy, P.; Cuevas, J. C. *Heat dissipation and its relation to thermopower in single-molecule junctions*. *New J Phys* **16**, 015004, (2014).

56. Pauly, F.; Viljas, J. K.; Burkle, M.; Dreher, M.; Nielaba, P.; Cuevas, J. C. *Molecular dynamics study of the thermopower of Ag, Au, and Pt nanocontacts*. *Phys Rev B* **84** (19), 195420, (2011).
57. Burkle, M.; Hellmuth, T. J.; Pauly, F.; Asai, Y. *First-principles calculation of the thermoelectric figure of merit for [2,2]paracyclophane-based single-molecule junctions*. *Phys Rev B* **91** (16), 165419, (2015).
58. Bergfield, J. P.; Stafford, C. A. *Thermoelectric Signatures of Coherent Transport in Single-Molecule Heterojunctions*. *Nano Lett* **9** (8), 3072-3076, (2009).
59. Wang, Z. H.; Carter, J. A.; Lagutchev, A.; Koh, Y. K.; Seong, N. H.; Cahill, D. G.; Dlott, D. D. *Ultrafast flash thermal conductance of molecular chains*. *Science* **317** (5839), 787-790, (2007).
60. Karlstrom, O.; Linke, H.; Karlstrom, G.; Wacker, A. *Increasing thermoelectric performance using coherent transport*. *Phys Rev B* **84** (11), 113415, (2011).
61. Mahan, G. D.; Sofo, J. O. *The best thermoelectric*. *Proc. Natl. Acad. Sci. USA* **93** (15), 7436-7439, (1996).
62. Nozaki, D.; Sevincli, H.; Li, W.; Gutierrez, R.; Cuniberti, G. *Engineering the figure of merit and thermopower in single-molecule devices connected to semiconducting electrodes*. *Phys Rev B* **81** (23), (2010).
63. Miroshnichenko, A. E.; Flach, S.; Kivshar, Y. S. *Fano resonances in nanoscale structures*. *Rev Mod Phys* **82** (3), 2257-2298, (2010).
64. Bohm, D., *Quantum theory*. Prentice-Hall: New York, (1951); p ix, 646 p.
65. Lambert, C. J. *Basic concepts of quantum interference and electron transport in single-molecule electronics*. *Chem Soc Rev* **44** (4), 875-888, (2015).
66. Bernien, M.; Wiedemann, D.; Hermanns, C. F.; Kruger, A.; Rolf, D.; Kroener, W.; Muller, P.; Grohmann, A.; Kuch, W. *Spin Crossover in a Vacuum-Deposited Submonolayer of a Molecular Iron(II) Complex*. *J Phys Chem Lett* **3** (23), 3431-3434, (2012).
67. Warner, B.; Oberg, J. C.; Gill, T. G.; El Hallak, F.; Hirjibehedin, C. F.; Serri, M.; Heutz, S.; Arrio, M. A.; Sainctavit, P.; Mannini, M.; Poneti, G.; Sessoli, R.; Rosa, P. *Temperature- and Light-Induced Spin Crossover Observed by X-ray Spectroscopy on Isolated Fe(II) Complexes on Gold*. *J Phys Chem Lett* **4** (9), 1546-1552, (2013).
68. Aravena, D.; Ruiz, E. *Coherent Transport through Spin-Crossover Single Molecules*. *J Am Chem Soc* **134** (2), 777-779, (2012).
69. Ghosh, D.; Parida, P.; Pati, S. K. *Spin-crossover molecule based thermoelectric junction*. *Appl Phys Lett* **106** (19), 193105, (2015).
70. Whitney, R. S. *Most Efficient Quantum Thermoelectric at Finite Power Output*. *Phys Rev Lett* **112** (13), 130601, (2014).
71. Whitney, R. S. *Finding the quantum thermoelectric with maximal efficiency and minimal entropy production at given power output*. *Phys Rev B* **91** (11), 115425, (2015).
72. Lambert, C. J.; Sadeghi, H.; Al-Galiby, Q. H. *Quantum-interference-enhanced thermoelectricity in single molecules and molecular films*. *Cr Phys* **17** (10), 1084-1095, (2016).
73. Garcia-Suarez, V. M.; Lambert, C. J.; Manrique, D. Z.; Wandlowski, T. *Redox control of thermopower and figure of merit in phase-coherent molecular wires*. *Nanotechnology* **25** (20), (2014).
74. Al-Galiby, Q. H.; Sadeghi, H.; Algharagholy, L. A.; Grace, I.; Lambert, C. *Tuning the thermoelectric properties of metallo-porphyrins*. *Nanoscale* **8** (4), 2428-2433, (2016).

75. Sadeghi, H.; Sangtarash, S.; Lambert, C. J. *Electron and heat transport in porphyrin-based single-molecule transistors with electro-burnt graphene electrodes*. *Beilstein J Nanotech* **6**, 1413-1420, (2015).
76. Lee, W.; Reddy, P. *Creation of stable molecular junctions with a custom-designed scanning tunneling microscope*. *Nanotechnology* **22** (48), 485703, (2011).
77. Tsutsui, M.; Morikawa, T.; He, Y.; Arima, A.; Taniguchi, M. *High thermopower of mechanically stretched single-molecule junctions*. *Sci. Rep.* **5**, 11519, (2015).
78. Widawsky, J. R.; Darancet, P.; Neaton, J. B.; Venkataraman, L. *Simultaneous Determination of Conductance and Thermopower of Single Molecule Junctions*. *Nano Lett* **12** (1), 354-358, (2012).
79. Malen, J. A.; Doak, P.; Baheti, K.; Tilley, T. D.; Segalman, R. A.; Majumdar, A. *Identifying the Length Dependence of Orbital Alignment and Contact Coupling in Molecular Heterojunctions*. *Nano Lett* **9** (3), 1164-1169, (2009).
80. Widawsky, J. R.; Chen, W.; Vazquez, H.; Kim, T.; Breslow, R.; Hybertsen, M. S.; Venkataraman, L. *Length-Dependent Thermopower of Highly Conducting Au-C Bonded Single Molecule Junctions*. *Nano Lett* **13** (6), 2889-2894, (2013).
81. Li, Y. Q.; Xiang, L. M.; Palma, J. L.; Asai, Y.; Tao, N. J. *Thermoelectric effect and its dependence on molecular length and sequence in single DNA molecules*. *Nat Commun* **7**, (2016).
82. Evangeli, C.; Gillemot, K.; Leary, E.; Gonzalez, M. T.; Rubio-Bollinger, G.; Lambert, C. J.; Agrait, N. *Engineering the Thermopower of C-60 Molecular Junctions*. *Nano Lett* **13** (5), 2141-2145, (2013).
83. Moreland, J.; Ekin, J. W. *Electron-Tunneling Experiments Using Nb-Sn Break Junctions*. *J Appl Phys* **58** (10), 3888-3895, (1985).
84. Muller, C. J.; Vanruitenbeek, J. M.; Dejongh, L. J. *Conductance and Supercurrent Discontinuities in Atomic-Scale Metallic Constrictions of Variable Width*. *Phys Rev Lett* **69** (1), 140-143, (1992).
85. Yanson, A. I.; Bollinger, G. R.; van den Brom, H. E.; Agrait, N.; van Ruitenbeek, J. M. *Formation and manipulation of a metallic wire of single gold atoms*. *Nature* **395** (6704), 783-785, (1998).
86. Ludoph, B.; van Ruitenbeek, J. M. *Thermopower of atomic-size metallic contacts*. *Phys Rev B* **59** (19), 12290-12293, (1999).
87. Smit, R. H.; Noat, Y.; Untiedt, C.; Lang, N. D.; van Hemert, M. C.; van Ruitenbeek, J. M. *Measurement of the conductance of a hydrogen molecule*. *Nature* **419** (6910), 906-9, (2002).
88. Agrait, N.; Yeyati, A. L.; van Ruitenbeek, J. M. *Quantum properties of atomic-sized conductors*. *Phys Rep* **377** (2-3), 81-279, (2003).
89. Smit, R. H. M.; Untiedt, C.; van Ruitenbeek, J. M. *The high-bias stability of monatomic chains*. *Nanotechnology* **15** (7), S472-S478, (2004).
90. Martin, C. A.; van Ruitenbeek, J. M.; van der Zant, H. S. J. *Sandwich-type gated mechanical break junctions*. *Nanotechnology* **21** (26), 265201, (2010).
91. Tsutsui, M.; Morikawa, T.; Arima, A.; Taniguchi, M. *Thermoelectricity in atom-sized junctions at room temperatures*. *Sci Rep-Uk* **3**, (2013).
92. Malen, J. A.; Doak, P.; Baheti, K.; Tilley, T. D.; Majumdar, A.; Segalman, R. A. *The Nature of Transport Variations in Molecular Heterojunction Electronics*. *Nano Lett* **9** (10), 3406-3412, (2009).

93. Macia, E. *DNA-based thermoelectric devices: A theoretical prospective*. *Phys Rev B* **75** (3), 035130, (2007).
94. Xue, Y. Q.; Ratner, M. A. *End group effect on electrical transport through individual molecules: A microscopic study*. *Phys Rev B* **69** (8), 085403, (2004).
95. Balachandran, J.; Reddy, P.; Dunietz, B. D.; Gavini, V. *End-Group Influence on Frontier Molecular Orbital Reorganization and Thermoelectric Properties of Molecular Junctions*. *J Phys Chem Lett* **4** (22), 3825-3833, (2013).
96. Balachandran, J.; Reddy, P.; Dunietz, B. D.; Gavini, V. *End-Group-Induced Charge Transfer in Molecular Junctions: Effect on Electronic-Structure and Thermopower*. *J Phys Chem Lett* **3** (15), 1962-1967, (2012).
97. Bilan, S.; Zotti, L. A.; Pauly, F.; Cuevas, J. C. *Theoretical study of the charge transport through C-60-based single-molecule junctions*. *Phys Rev B* **85** (20), 205403, (2012).
98. Baheti, K.; Malen, J. A.; Doak, P.; Reddy, P.; Jang, S. Y.; Tilley, T. D.; Majumdar, A.; Segalman, R. A. *Probing the chemistry of molecular heterojunctions using thermoelectricity*. *Nano Lett* **8** (2), 715-719, (2008).
99. Lee, S. K.; Buerkle, M.; Yamada, R.; Asai, Y.; Tada, H. *Thermoelectricity at the molecular scale: a large Seebeck effect in endohedral metallofullerenes*. *Nanoscale* **7** (48), 20497-20502, (2015).
100. Rincon-Garcia, L.; Ismael, A. K.; Evangeli, C.; Grace, I.; Rubio-Bollinger, G.; Porfyrakis, K.; Agrait, N.; Lambert, C. J. *Molecular design and control of fullerene-based bi-thermoelectric materials*. *Nat Mater* **15** (3), 289-294, (2016).
101. Venkataraman, L.; Klare, J. E.; Nuckolls, C.; Hybertsen, M. S.; Steigerwald, M. L. *Dependence of single-molecule junction conductance on molecular conformation*. *Nature* **442** (7105), 904-907, (2006).
102. Mishchenko, A.; Vonlanthen, D.; Meded, V.; Burkle, M.; Li, C.; Pobelov, I. V.; Bagrets, A.; Viljas, J. K.; Pauly, F.; Evers, F.; Mayor, M.; Wandlowski, T. *Influence of Conformation on Conductance of Biphenyl-Dithiol Single-Molecule Contacts*. *Nano Lett* **10** (1), 156-163, (2010).
103. Wang, K.; Hamill, J. M.; Wang, B.; Guo, C. L.; Jiang, S. B.; Huang, Z.; Xu, B. Q. *Structure determined charge transport in single DNA molecule break junctions*. *Chem. Sci.* **5** (9), 3425-3431, (2014).
104. Yee, S. K.; Malen, J. A.; Majumdar, A.; Segalman, R. A. *Thermoelectricity in Fullerene-Metal Heterojunctions*. *Nano Lett* **11** (10), 4089-4094, (2011).
105. Lee, S. K.; Ohto, T.; Yamada, R.; Tada, H. *Thermopower of benzenedithiol and C60 molecular junctions with Ni and Au electrodes*. *Nano Lett* **14** (9), 5276-80, (2014).
106. Zerah-Harush, E.; Dubi, Y. *Enhanced Thermoelectric Performance of Hybrid Nanoparticle-Single-Molecule Junctions*. *Phys Rev Appl* **3** (6), 064017, (2015).
107. Beebe, J. M.; Engelkes, V. B.; Miller, L. L.; Frisbie, C. D. *Contact resistance in metal-molecule-metal junctions based on aliphatic SAMs: Effects of surface linker and metal work function*. *J Am Chem Soc* **124** (38), 11268-11269, (2002).
108. Yaliraki, S. N.; Kemp, M.; Ratner, M. A. *Conductance of molecular wires: Influence of molecule-electrode binding*. *J Am Chem Soc* **121** (14), 3428-3434, (1999).
109. Kim, Y.; Lenert, A.; Meyhofer, E.; Reddy, P. *Temperature dependence of thermopower in molecular junctions*. *Appl Phys Lett* **109** (3), 033102, (2016).
110. Champagne, A. R.; Pasupathy, A. N.; Ralph, D. C. *Mechanically adjustable and electrically gated single-molecule transistors*. *Nano Lett* **5** (2), 305-308, (2005).

111. Osorio, E. A.; Bjornholm, T.; Lehn, J. M.; Ruben, M.; van der Zant, H. S. J. *Single-molecule transport in three-terminal devices*. *J Phys-Condens Mat* **20** (37), 374121, (2008).
112. Park, H.; Lim, A. K. L.; Alivisatos, A. P.; Park, J.; McEuen, P. L. *Fabrication of metallic electrodes with nanometer separation by electromigration*. *Appl Phys Lett* **75** (2), 301-303, (1999).
113. Park, J.; Pasupathy, A. N.; Goldsmith, J. I.; Chang, C.; Yaish, Y.; Petta, J. R.; Rinkoski, M.; Sethna, J. P.; Abruna, H. D.; McEuen, P. L.; Ralph, D. C. *Coulomb blockade and the Kondo effect in single-atom transistors*. *Nature* **417** (6890), 722-725, (2002).
114. Maeng, J.; Jo, G.; Kwon, S. S.; Song, S.; Seo, J.; Kang, S. J.; Kim, D. Y.; Lee, T. *Effect of gate bias sweep rate on the electronic properties of ZnO nanowire field-effect transistors under different environments*. *Appl Phys Lett* **92** (23), 233120, (2008).
115. Osorio, E. A.; Moth-Poulsen, K.; van der Zant, H. S. J.; Paaske, J.; Hedegard, P.; Flensberg, K.; Bendix, J.; Bjornholm, T. *Electrical Manipulation of Spin States in a Single Electrostatically Gated Transition-Metal Complex*. *Nano Lett* **10** (1), 105-110, (2010).
116. Javey, A.; Kim, H.; Brink, M.; Wang, Q.; Ural, A.; Guo, J.; McIntyre, P.; McEuen, P.; Lundstrom, M.; Dai, H. J. *High-kappa dielectrics for advanced carbon-nanotube transistors and logic gates*. *Nat Mater* **1** (4), 241-246, (2002).
117. Gabor, N. M.; Zhong, Z. H.; Bosnick, K.; Park, J.; McEuen, P. L. *Extremely Efficient Multiple Electron-Hole Pair Generation in Carbon Nanotube Photodiodes*. *Science* **325** (5946), 1367-1371, (2009).
118. Jarillo-Herrero, P.; Kong, J.; van der Zant, H. S. J.; Dekker, C.; Kouwenhoven, L. P.; De Franceschi, S. *Orbital Kondo effect in carbon nanotubes*. *Nature* **434** (7032), 484-488, (2005).
119. Jeong, W.; Kim, K.; Kim, Y.; Lee, W.; Reddy, P. *Characterization of nanoscale temperature fields during electromigration of nanowires (vol 4, 4975, 2014)*. *Sci Rep-Uk* **4**, 4975, (2014).
120. Lee, W.; Kim, K.; Jeong, W.; Zotti, L. A.; Pauly, F.; Cuevas, J. C.; Reddy, P. *Heat dissipation in atomic-scale junctions*. *Nature* **498** (7453), 209-213, (2013).
121. Scheer, E.; Agrait, N.; Cuevas, J. C.; Yeyati, A. L.; Ludoph, B.; Martin-Rodero, A.; Bollinger, G. R.; van Ruitenbeek, J. M.; Urbina, C. *The signature of chemical valence in the electrical conduction through a single-atom contact*. *Nature* **394** (6689), 154-157, (1998).
122. Guo, S. Y.; Zhou, G.; Tao, N. J. *Single Molecule Conductance, Thermopower, and Transition Voltage*. *Nano Lett* **13** (9), 4326-4332, (2013).
123. Tsutsui, M.; Morikawa, T.; He, Y. H.; Arima, A.; Taniguchi, M. *High thermopower of mechanically stretched single-molecule junctions*. *Sci Rep-Uk* **5**, 11519 (2015).
124. Arroyo, C. R.; Tarkuc, S.; Frisenda, R.; Seldenthuis, J. S.; Woerde, C. H. M.; Eelkema, R.; Grozema, F. C.; van der Zant, H. S. J. *Signatures of Quantum Interference Effects on Charge Transport Through a Single Benzene Ring*. *Angew Chem Int Edit* **52** (11), 3152-3155, (2013).
125. Kaliginedi, V.; Moreno-Garcia, P.; Valkenier, H.; Hong, W. J.; Garcia-Suarez, V. M.; Buiter, P.; Otten, J. L. H.; Hummelen, J. C.; Lambert, C. J.; Wandlowski, T. *Correlations between Molecular Structure and Single-Junction Conductance: A Case Study with Oligo(phenylene-ethynylene)-Type Wires*. *J Am Chem Soc* **134** (11), 5262-5275, (2012).
126. Scott, G. D.; Natelson, D. *Kondo Resonances in Molecular Devices*. *Acs Nano* **4** (7), 3560-3579, (2010).

127. Sánchez, D.; López, R. *Scattering Theory of Nonlinear Thermoelectric Transport*. *Phys Rev Lett* **110** (2), 026804, (2013).
128. Keane, Z. K.; Ciszek, J. W.; Tour, J. M.; Natelson, D. *Three-terminal devices to examine single-molecule conductance switching*. *Nano Lett* **6** (7), 1518-1521, (2006).
129. Cui, L. J.; Miao, R. J.; Wang, K.; Thompson, D.; Zotti, L. A.; Cuevas, J. C.; Meyhofer, E.; Reddy, P. *Peltier cooling in molecular junctions*. *Nat Nanotechnol* **13** (2), 122-128, (2018).
130. Pedersen, K. G. L.; Strange, M.; Leijnse, M.; Hedegard, P.; Solomon, G. C.; Paaske, J. *Quantum interference in off-resonant transport through single molecules*. *Phys Rev B* **90** (12), 125413, (2014).
131. Yoshizawa, K.; Tada, T.; Staykov, A. *Orbital views of the electron transport in molecular devices*. *J Am Chem Soc* **130** (29), 9406-9413, (2008).
132. Manrique, D. Z.; Huang, C.; Baghernejad, M.; Zhao, X. T.; Al-Owaedi, O. A.; Sadeghi, H.; Kaliginedi, V.; Hong, W. J.; Gulcur, M.; Wandlowski, T.; Bryce, M. R.; Lambert, C. J. *A quantum circuit rule for interference effects in single-molecule electrical junctions*. *Nat Commun* **6**, 6389, (2015).
133. Huh, T. W.; Han, G.; Ban, W. J.; Ahn, H. S. *Efficient fabrication of gold tips by electrochemical etching for tip-enhanced Raman spectroscopy*. *Int J Precis Eng Man* **18** (2), 221-226, (2017).
134. Frisenda, R.; van der Zant, H. S. J. *Transition from Strong to Weak Electronic Coupling in a Single-Molecule Junction*. *Phys Rev Lett* **117** (12), 126804, (2016).
135. Frisenda, R.; Janssen, V. A. E. C.; Grozema, F. C.; van der Zant, H. S. J.; Renaud, N. *Mechanically controlled quantum interference in individual pi-stacked dimers*. *Nat Chem* **8** (12), 1099-1104, (2016).
136. Frisenda, R.; Tarkuc, S.; Galan, E.; Perrin, M. L.; Eelkema, R.; Grozema, F. C.; van der Zant, H. S. J. *Electrical properties and mechanical stability of anchoring groups for single-molecule electronics*. *Beilstein J Nanotech* **6**, 1558-1567, (2015).
137. Stokbro, K.; Taylor, J.; Brandbyge, M.; Mozos, J. L.; Ordejon, P. *Theoretical study of the nonlinear conductance of Di-thiol benzene coupled to Au(111) surfaces via thiol and thiolate bonds*. *Comp Mater Sci* **27** (1-2), 151-160, (2003).
138. Pauly, F.; Viljas, J. K.; Huniar, U.; Hafner, M.; Wohlthat, S.; Burkle, M.; Cuevas, J. C.; Schon, G. *Cluster-based density-functional approach to quantum transport through molecular and atomic contacts*. *New J Phys* **10**, 125019, (2008).
139. Brandbyge, M.; Mozos, J. L.; Ordejón, P.; Taylor, J.; Stokbro, K. *Density-functional method for nonequilibrium electron transport*. *Phys Rev B* **65** (16), 165401, (2002).
140. *TURBOMOLE V7.2 2017* http://www.turbomole.com.,
141. Quek, S. Y.; Venkataraman, L.; Choi, H. J.; Louie, S. G.; Hybertsen, M. S.; Neaton, J. B. *Amine-gold linked single-molecule circuits: Experiment and theory*. *Nano Lett* **7** (11), 3477-3482, (2007).
142. Garner, M. H.; Li, H. X.; Chen, Y.; Su, T. A.; Shangguan, Z.; Paley, D. W.; Liu, T. F.; Ng, F.; Li, H. X.; Xiao, S. X.; Nuckolls, C.; Venkataraman, L.; Solomon, G. C. *Comprehensive suppression of single-molecule conductance using destructive sigma-interference*. *Nature* **558** (7710), 415-+, (2018).
143. Josefsson, M.; Svilans, A.; Burke, A. M.; Hoffmann, E. A.; Fahlvik, S.; Thelander, C.; Leijnse, M.; Linke, H. *A quantum-dot heat engine operated close to thermodynamic efficiency limits*. *arXiv:1710.00742 [cond-mat.mes-hall]*,

144. Liu, Z. F.; Wei, S. J.; Yoon, H.; Adak, O.; Ponce, I.; Jiang, Y.; Jang, W. D.; Campos, L. M.; Venkataraman, L.; Neaton, J. B. *Control of Single-Molecule Junction Conductance of Porphyrins via a Transition-Metal Center*. *Nano Lett* **14** (9), 5365-5370, (2014).
145. Noori, M.; Aragones, A. C.; Di Palma, G.; Darwish, N.; Bailey, S. W. D.; Al-Galiby, Q.; Grace, I.; Amabilino, D. B.; Gonzalez-Campo, A.; Diez-Perez, I.; Lambert, C. J. *Tuning the electrical conductance of metalloporphyrin supramolecular wires*. *Sci Rep-Uk* **6**, (2016).
146. Aragones, A. C.; Darwish, N.; Saletra, W. J.; Perez-Garcia, L.; Sanz, F.; Puigmarti-Luis, J.; Amabilino, D. B.; Diez-Perez, I. *Highly Conductive Single-Molecule Wires with Controlled Orientation by Coordination of Metalloporphyrins*. *Nano Lett* **14** (8), 4751-4756, (2014).
147. Cheng, Z. L.; Skouta, R.; Vazquez, H.; Widawsky, J. R.; Schneebeli, S.; Chen, W.; Hybertsen, M. S.; Breslow, R.; Venkataraman, L. *In situ formation of highly conducting covalent Au-C contacts for single-molecule junctions*. *Nat Nanotechnol* **6** (6), 353-357, (2011).
148. Olavarria-Contreras, I. J.; Perrin, M. L.; Chen, Z.; Klyatskaya, S.; Ruben, M.; van der Zant, H. S. J. *C-Au Covalently Bonded Molecular Junctions Using Nonprotected Alkynyl Anchoring Groups*. *J Am Chem Soc* **138** (27), 8465-8469, (2016).
149. Arasu, N. P.; Vazquez, H. *Direct Au-C contacts based on biphenylene for single molecule circuits*. *Phys Chem Chem Phys* **20** (15), 10378-10383, (2018).
150. Sadeghi, H.; Sangtarash, S.; Lambert, C. J. *Oligoyne Molecular Junctions for Efficient Room Temperature Thermoelectric Power Generation*. *Nano Lett* **15** (11), 7467-7472, (2015).
151. Rowe, D. M., *Thermoelectrics handbook : macro to nano*. CRC/Taylor & Francis: Boca Raton, (2006).
152. Callen, H. B., *Thermodynamics; an introduction to the physical theories of equilibrium thermostatics and irreversible thermodynamics*. Wiley: New York,, (1960); p 376 p.
153. Huang, Z. F.; Chen, F.; D'Agosta, R.; Bennett, P. A.; Di Ventra, M.; Tao, N. J. *Local ionic and electron heating in single-molecule junctions*. *Nat Nanotechnol* **2** (11), 698-703, (2007).
154. Ioffe, Z.; Shamai, T.; Ophir, A.; Noy, G.; Yutsis, I.; Kfir, K.; Cheshnovsky, O.; Selzer, Y. *Detection of heating in current-carrying molecular junctions by Raman scattering*. *Nat Nanotechnol* **3** (12), 727-732, (2008).
155. Ward, D. R.; Corley, D. A.; Tour, J. M.; Natelson, D. *Vibrational and electronic heating in nanoscale junctions*. *Nat Nanotechnol* **6** (1), 33-38, (2011).
156. Galperin, M.; Saito, K.; Balatsky, A. V.; Nitzan, A. *Cooling mechanisms in molecular conduction junctions*. *Phys Rev B* **80** (11), 115427, (2009).
157. Wold, D. J.; Frisbie, C. D. *Fabrication and characterization of metal-molecule-metal junctions by conducting probe atomic force microscopy*. *J Am Chem Soc* **123** (23), 5549-5556, (2001).
158. Choi, S. H.; Kim, B.; Frisbie, C. D. *Electrical resistance of long conjugated molecular wires*. *Science* **320** (5882), 1482-1486, (2008).
159. Cui, L. J.; Jeong, W.; Hur, S.; Matt, M.; Klockner, J. C.; Pauly, F.; Nielaba, P.; Cuevas, J. C.; Meyhofer, E.; Reddy, P. *Quantized thermal transport in single-atom junctions*. *Science* **355** (6330), 1192-1195, (2017).

160. Florin, E. L.; Rief, M.; Lehmann, H.; Ludwig, M.; Dornmair, C.; Moy, V. T.; Gaub, H. E. *Sensing Specific Molecular-Interactions with the Atomic-Force Microscope*. *Biosens Bioelectron* **10** (9-10), 895-901, (1995).
161. Frank, I. W.; Tanenbaum, D. M.; Van der Zande, A. M.; McEuen, P. L. *Mechanical properties of suspended graphene sheets*. *J Vac Sci Technol B* **25** (6), 2558-2561, (2007).
162. Henderson, J. I.; Feng, S.; Bein, T.; Kubiak, C. P. *Adsorption of diisocyanides on gold*. *Langmuir* **16** (15), 6183-6187, (2000).
163. Frey, S.; Stadler, V.; Heister, K.; Eck, W.; Zharnikov, M.; Grunze, M.; Zeysing, B.; Terfort, A. *Structure of thioaromatic self-assembled monolayers on gold and silver*. *Langmuir* **17** (8), 2408-2415, (2001).
164. Lu, Q.; Liu, K.; Zhang, H. M.; Du, Z. B.; Wang, X. H.; Wang, F. S. *From Tunneling to Hopping: A Comprehensive Investigation of Charge Transport Mechanism in Molecular Junctions Based on Oligo(p-phenylene ethynylene)s*. *Acs Nano* **3** (12), 3861-3868, (2009).
165. Bain, C. D.; Whitesides, G. M. *Attenuation Lengths of Photoelectrons in Hydrocarbon Films*. *J Phys Chem-Us* **93** (4), 1670-1673, (1989).
166. Azzam, W.; Wehner, B. I.; Fischer, R. A.; Terfort, A.; Woll, C. *Bonding and orientation in self-assembled monolayers of oligophenyldithiols on Au substrates*. *Langmuir* **18** (21), 7766-7769, (2002).
167. Kamenetska, M.; Quek, S. Y.; Whalley, A. C.; Steigerwald, M. L.; Choi, H. J.; Louie, S. G.; Nuckolls, C.; Hybertsen, M. S.; Neaton, J. B.; Venkataraman, L. *Conductance and Geometry of Pyridine-Linked Single-Molecule Junctions*. *J Am Chem Soc* **132** (19), 6817-6821, (2010).
168. Diao, Y. X.; Han, M. J.; Wan, L. J.; Itaya, K.; Uchida, T.; Miyake, H.; Yamakata, A.; Osawa, M. *Adsorbed structures of 4,4 '-bipyridine on Cu(111) in acid studied by STM and IR*. *Langmuir* **22** (8), 3640-3646, (2006).
169. Johnson, K. L. *Contact Mechanics*. *P I Mech Eng J-J Eng* **223** (J3), 254-254, (2009).
170. Whelan, C. M.; Smyth, M. R.; Barnes, C. J. *HREELS, XPS, and electrochemical study of benzenethiol adsorption on Au(111)*. *Langmuir* **15** (1), 116-126, (1999).
171. Johnson, K. L.; Kendall, K.; Roberts, A. D. *Surface Energy and Contact of Elastic Solids*. *Proc R Soc Lon Ser-A* **324** (1558), 301-&, (1971).
172. Sadat, S.; Meyhofer, E.; Reddy, P. *High resolution resistive thermometry for micro/nanoscale measurements*. *Rev Sci Instrum* **83** (8), (2012).
173. Akamatu, H.; Inokuchi, H.; Matsunaga, Y. *Electrical Conductivity of the Perylene-Bromine Complex*. *Nature* **173** (4395), 168-169, (1954).
174. Vezzoli, A.; Grace, I.; Brooke, C.; Wang, K.; Lambert, C. J.; Xu, B. Q.; Nichols, R. J.; Higgins, S. J. *Gating of single molecule junction conductance by charge transfer complex formation*. *Nanoscale* **7** (45), 18949-18955, (2015).